The dynamics of cross-shore sediment transport
in the Rhine region of freshwater influence

Raul Flores Audibert

A dissertation
submitted in partial fulfillment of the
requirements for the degree of

Doctor of Philosophy

University of Washington

2018

Reading Committee:

Alexander R. Horner-Devine, Chair

Nirnimesh Kumar

Andrea S. Ogston

Julie D. Pietrzak

Alejandro J. Souza

Program Authorized to Offer Degree:
Civil and Environmental Engineering

University of Washington

Abstract

The dynamics of cross-shore sediment transport
in the Rhine region of freshwater influence

Raul Flores Audibert

Chair of the Supervisory Committee:
Professor Alexander R. Horner-Devine
Civil and Environmental Engineering Department

River plumes are critical to the exchange of suspended particulate matter (SPM) between nearshore regions and shelf seas. These exchanges contribute fundamentally to the health and function of the coastal ecosystem, and have important implications for the overall sediment and biomass budgets. The physical processes that determine these exchanges depend on the dynamical characteristics of the river plume, which are largely affected by the freshwater input, water depth and the tidal flow, among many other factors. Here, we present field measurements and numerical modeling of hydrodynamics and sediment transport in order to investigate the dynamics of cross-shore exchange processes along a shallow river plume system.

Measurements from moorings and bottom frames along the Rhine region of freshwater influence (ROFI) are used to evaluate the importance of baroclinic (stratified) and barotropic (unstratified) dynamics on the cross-shore transport of fine sediments, in a site located 10 km north of the river mouth. These measurements allowed for the evaluation of sediment transport dynamics over a wide range of stratification, wind, wave and tidal conditions. Both barotropic and baroclinic processes are found to be relevant for the cross-shore transport of fines at depth. The observations suggest that wind and wave-driven transport during storms tends move fine sediment offshore, while calmer, more stratified conditions move it back onshore.

Data collected during an intense 2-day storm are used to document the occurrence of a wave-supported gravity flow (WSGF) in a shallow inner shelf site along the Rhine ROFI. These observations are the first to document a WSGF on a predominantly sandy environment; previous observations had been restricted to muddy shelf deposits with very fine particle size distributions. The observed WSGF dynamics support previous studies regarding the use of a friction-buoyancy balance, and suggest that the same balance can be used on sandy seabeds. The offshore transport associated with the WSGF was much higher than other modes of transport, such as the suspended transport in the upper water column or the bedload, highlighting the importance of these events to cross-shelf transport and morphological evolution on inner-shelf regions. The occurrence of a WSGF under conditions unique from previous observations suggest that WSGF may occur in a much wider range of shelf locations than previously thought.

In the Rhine, the tidal flow interacts with the cross-shore density gradients to generate tidal straining. The influence of tidal straining in the generation of a turbidity maximum zone (TMZ) along the Rhine ROFI is investigated using idealized numerical simulations. Tidal straining leads to cross-shore sediment convergence and the formation of a nearshore TMZ, that is detached from the coastline and confined to the near-bed region. Subtidal landward sediment fluxes are created by asymmetries in vertical mixing between the stratifying and de-stratifying phases of the tidal cycle. Model simulations show the development of a coastal TMZ for a wide range of horizontal density gradients, latitudes and settling velocity of bed sediments, suggesting that this phenomena is not limited to the Rhine ROFI. A parameter space for the occurrence of tidal straining and a coastal turbidity maximum is proposed in terms of a horizontal Richardson number and a Stokes number.

Lastly, near-bed turbulence and bedform measurements are used to investigate the influence of bed roughness in the estimation of bed shear stress under the influence of large waves and currents. Direct measurements of the near-bed Reynolds stresses are compared to bed stress estimates obtained from a 1D bottom boundary layer model that accounts for wave-current interaction. Model-derived bed stresses compare well with measurements when field measurements of bedform dimensions are

incorporated into the model calculations. The use of standard bedform predictors based on bulk wave properties results in a severe overestimation of the bed stresses at this particular site. We find that the combination of a time-dependent bedform evolution model and a 1D wave-current boundary layer model provides a simple approach that allows improved bed stress estimates in cases where bedform data is not available. Estimates of bed stresses and measured vertical turbulent sediment fluxes are then incorporated into a linear erosion formulation to obtain field-based estimates of the critical stress for erosion and resuspension constant.

TABLE OF CONTENTS

LIST OF FIGURES

ACKNOWLEDGMENTS

First, I'd like to thank my advisor, Alex Horner-Devine. I cannot begin to describe how lucky I consider myself to have had Alex as a mentor, and to have worked under his supervision for these past four years. I'd like to thank Alex for all his kindness and support, for all the discussions and inspiration, and for sharing his expertise and passion for science with me. Our weekly meetings were something I always looked forward to, as I knew that I'd be a better scientist after them. One day, I hope to be as good advisor to my own students as Alex was to me. For all he has taught me, science related or not, I will be always grateful.

I would also like to thank my committee, Andrea Ogston, Julie Pietrzak, Jim Thomson, Nirni Kumar, Jim Riley and Alejandro Souza. They offered invaluable advice and guidance on my work and progress for which I am extremely grateful. Particular thanks to Julie Pietrzak and Alejandro Souza for their support, advice and guidance from the moment I started my PhD work. I am privileged to have worked with them and hope to continue to do so in the future. I would also like to give special thanks to Nirni Kumar for all his help, support, motivation and for sharing his modeling expertise.

A big thank you to the EFM group. This is truly a group of amazing people. Thanks for all the help with homework, problem sets, for all the discussions and for all the good times. I'd like to mention a few students I crossed paths with, even though all EFM members provided guidance, advice or inspiration at one time or another: thanks to Anthony, Sam, Roxanne, Ruth, Zhouchen, Seth, Mike, David and Christine. Special thanks to Maru and Maddie, for countless hours of study, homework and fun during our first year at UW (go 2014!). I'd also like to thank Maggie Mckeon, for all the help and patience during the field work in The Netherlands. Having said all that, I'd like to single out one member of the EFM group, Maru, the other half of the Chilean EFM team. I'll always be grateful for her friendship, support, good laughs and for her role in making the grad school experience so great for me.

DEDICATION

to my beautiful wife, Daniela, and to my family

Chapter 1

INTRODUCTION

1.1 Motivation

Rivers deliver significant amounts of freshwater, sediment, terrestrial nutrients, biomass and contaminants to the coastal ocean (*Milliman and Syvitski*, 1992), creating buoyant plumes that become the interface between rivers and continental shelf seas. These buoyant plumes can flow along the coast for tens of kilometers (*Simpson et al.*, 1993; *Fong and Geyer*, 2001; *Horner-Devine et al.*, 2015), altering the structure of the coastal ecosystem and determining the final fate of terrestrial material. A detailed understanding of the physical processes that govern the spatial and temporal variability of the dynamics of these regions has important consequences regarding the management of coastal resources, in both short and long term timescales. On short timescales, for example, stratification resulting from riverine freshwater may inhibit the vertical transport of substances such as oxygen and nutrients, affecting the distribution of biota along the coast (*Joordens et al.*, 2001; *Hickey et al.*, 2010; *van der Hout et al.*, 2017). On longer timescales, the flow in these regions controls the net export of sediment to the outer shelf and exerts control on the morphology of coastal regions (*Milliman and Meade*, 1983; *Geyer et al.*, 2004; *Souza et al.*, 2007).

River plumes are extremely complex and dynamical regions, which are affected by freshwater discharge, tidal amplitude, coastline bathymetry, ocean currents, winds and Earth's rotation (*Simpson*, 1997; *Horner-Devine et al.*, 2015). As rivers drain watersheds all over the globe, they are very common features along coastlines worldwide. Around forty percent of the global population lives within 100 kilometers of a coast [1], and a large percentage of that population will have regular access to coastal zones that are located close to an estuary and are thus influenced by a river plume. As human population grows near these regions, the pressure on river-estuary-plume systems increases

---

[1]United Nations, http://www.un.org/esa/sustdev/natlinfo/indicators/methodology_sheets/oceans_seas_coasts/pop_coastal_areas.pdf

substantially. The rate at which waste water discharge, fertilizers and agricultural products are discharged into the coastal ecosystem to accommodate the evolving needs of a growing population is increased. Direct human intervention, such as the construction of dams, the implementation of coastal engineering projects and dredging on estuarine or coastal waterways, is becoming more frequent. Being able to predict the impact of such interventions becomes a necessity to sustainably manage coastal areas, as they have the potential to alter the ambient transport pathways and modify the distribution of biomass and sediments. From a societal standpoint, and in light of current trends that suggest that populations in coastal zones will continue to grow, understanding how human activity shapes the coastal ecosystem and its resources is very relevant. Those effects can be understood in terms of the hydrodynamics and associated transport processes in rivers, estuaries and river plumes.

Among all processes that occur in the coastal ocean, the transport of suspended particulate matter (SPM) contributes fundamentally to the health and function of the coastal ecosystem. The impact of river plume processes on SPM dynamics has gained much relevance over the last few decades in light of the pressure that large-scale engineering projects have exerted on the morphodynamics of coastal areas, and, additionally, due to the undesirable effects of climate change and sea-level rise. SPM regimes in river plumes are different from those of wave-dominated environments in the nearshore and those of outer shelf seas. The density difference between riverine and salt water has important consequences on the delivery, transport and ultimate fate of the terrigenous sediment (*Geyer et al.*, 2004). Due to processes such as settling, aggregation and flocculation, the pathways of sediments are different than those of riverine freshwater and are frequently much more complex. Sediments can be trapped in frontal zones, either in the estuary or on the shelf, which may often lead to large increases in suspended sediment concentrations (*Jay and Smith*, 1990; *Geyer et al.*, 2004; *Souza et al.*, 2007; *Amoudry and Souza*, 2011). Stratification leads to the suppression of turbulence at the pycnocline (*Geyer*, 1993; *de Nijs et al.*, 2010), which inhibits vertical diffusion and traps suspended matter in regions close to the bed (*Souza et al.*, 2007). As a consequence, sediment transport in river-influenced regions is often dominated by near-bottom fluxes (*Geyer et al.*, 2004; *Traykovski*, 2007), suggesting that near-bed measurements are required to avoid erroneous conclusions about the magnitude and direction of transport, and about the physical processes responsible

for the transport. This relates not only to sediments, but also to contaminants, nutrients, organic carbon, plankton and chlorophyll-a (*Joordens et al.*, 2001; *Hickey et al.*, 2010; *Souza and Lane*, 2013; *van der Hout et al.*, 2017).

Despite the progress achieved in the research of SPM transport in river-dominated environments, much remains to be understood before we can unequivocally predict the magnitude of fluxes and depositional patterns on coastal regions. Each river system is different and different physical processes may dominate depending on freshwater discharge, sediment load, sedimentary environment and water depth, among many other factors. Furthermore, transport processes may vary within a river plume system depending on the location with respect to the mouth of the estuary (*Horner-Devine et al.*, 2015).

In this thesis, we aim to contribute to the understanding of sediment transport dynamics in shallow, frictional river plumes, which are commonly referred to as regions of freshwater influence (ROFIs, (*Simpson*, 1997)). The fundamental questions we investigate are motivated by the need to better understand the physical mechanisms that lead to cross-shore sediment fluxes, which enable the exchange of SPM between the near-shore and the inner (and outer) shelf region. These mechanisms may determine whether SPM accumulates in the coastal system or is exported to the abyssal ocean, and thus play a key role in understanding the overall source to sink sediment budget.

1.2 Regions of freshwater influence

On a global scale, ROFIs represent an important component of the shelf sea environment (*Simpson*, 1997), and, consequently, the study of the dynamics of sediment transport and dispersal in these systems is relevant for human life. The formal definition of a ROFI was first provided by *Simpson* (1997): The region between the shelf sea regime and the estuary where the local input of freshwater buoyancy from the coastal source is comparable with, or exceeds, the seasonal input of buoyancy as heat which occurs all over the shelf. The distinctive feature of all ROFI systems is then the input of significant amounts of buoyancy as freshwater from one large river, multiple smaller rivers or a combination of river systems of different sizes.

Upon exiting the river mouth, the influence of Earth's rotation turns riverine freshwater anti-cyclonically and generates a classical buoyant current that flows with the coast to its right (in the Northern hemisphere). In ROFIs, water column structure (density and currents) is the result of the competition between the stratifying influence of the baroclinic flow and the stirring (mixing) effect induced by the tides, waves and winds. As these forcing conditions can change their intensity rapidly, ROFI systems may switch between stratified and vertically mixed conditions on relatively short timescales when compared to outer shelf seas (*Simpson et al.*, 1993; *Souza and Simpson*, 1996). An important and predictable component of the stratification-stirring competition is the tidal flow, which tends to induce a fortnightly (14.5 days) variation in stratification due to the spring-neap cycle. The fortnightly variation in water column stability has been extensively documented in ROFI systems such as Liverpool Bay (*Simpson et al.*, 1990; *Simpson*, 1997) and the Rhine (*Simpson et al.*, 1993; *Simpson and Souza*, 1995; *Souza et al.*, 1997).

In addition to the fortnightly cycle that is imposed by the tides, which can be randomly modified by waves and winds (*Simpson and Souza*, 1995; *Souza and Simpson*, 1997), the tidal straining mechanism induces marked semi-diurnal oscillations in stratification (*Simpson et al.*, 1990; *Simpson and Souza*, 1995; *Rippeth et al.*, 2001). Tidal straining corresponds to the interaction between the tidal shear and the horizontal density gradients, which act to alternately induce and destroy stratification (*Simpson et al.*, 1990). Observation of semi-diurnal oscillations in stratification, in which the water column may vary between a well-mixed state and stratified within a single tidal cycle, are characteristic features of the Liverpool Bay ROFI (*Simpson et al.*, 1990; *Rippeth et al.*, 2001; *Verspecht et al.*, 2009a) and the Rhine ROFI (*Simpson and Souza*, 1995; *De Boer et al.*, 2008). Overall, the structure of density and currents in ROFIs involves a complex superposition of processes that can vary on a wide range of timescales. These processes will, in turn, condition the mechanisms by which sediments are transported and distributed in ROFI systems.

In this work we are concerned with ROFI systems that have a strong interaction with the bottom, and that can be classified as bottom attached plumes (*Geyer et al.*, 2004; *Yankovsky and Chapman*, 1997). Bottom friction is important in these systems, and is one the most relevant dynamical parameters that control, for example, the cross-shore scale of the plume (*Horner-Devine et al.*, 2015),

the inhibition of instabilities (*Münchow and Garvine*, 1993) and the distribution of suspended sediments (*Pietrzak et al.*, 2011). Bottom attached plumes can potentially carry sediments further away than the limits dictated by particle settling, since turbulence arising from bottom stresses can maintain sediments in the water column for long periods of time (*Geyer et al.*, 2004). In general, the baroclinic flow does not generate appreciable bottom stresses (*Chapman and Lentz*, 1994; *Geyer et al.*, 2004), and the energy that enables sediment resuspension in shallow shelf environments often comes from the tidal flow. Tidally-induced bed stresses are a key component of sediment transport dynamics in bottom-attached systems (*Jones et al.*, 1996; *Geyer et al.*, 2004; *Pietrzak et al.*, 2011).

In ROFIs, the buoyancy input competes with the mixing induced by the tides, winds and waves to establish stratification. The tide, wind and wave mixing also compete with particle settling to maintain fine sediment in the water column. The instantaneous movement of sediments in shallow regions is usually related to the tidal flow and wave forcing, however, the long term transport in ROFIs is typically a result of residual currents and turbulent dispersion processes which are significantly modified by the density-driven circulation (*Souza and Lane*, 2013). An important consequence of density gradients in ROFIs is the generation of subtidal (low frequency) landward sediment fluxes (*Burchard et al.*, 2008; *Souza and Lane*, 2013), which may result in regions of sediment convergence and high suspended sediment concentrations.

1.3   The Rhine region of freshwater influence

In this thesis, we focus our attention on the ROFI generated by the second largest river in Europe, the Rhine River. The Rhine discharges an average of 2500 m^{3}s^{-1} into the southern North Sea (Figure 1.1), sustaining an extensive ROFI that has important implications for water column structure and dynamics along the Dutch coast (*Simpson and Souza*, 1995). The Rhine ROFI typically spans approximately 20 km in the cross-shore direction and it extends for over 100 km downstream (northwards) from the river mouth (*Simpson et al.*, 1993; *De Boer*, 2009).

The most energetic driving force in the North Sea is the semi-diurnal tide, which interacts with the density field set by the ROFI creating a complex current structure (*Simpson*, 1997). *Simpson et al.* (1993) identified that the Rhine ROFI shows variations in stratification primarily at two
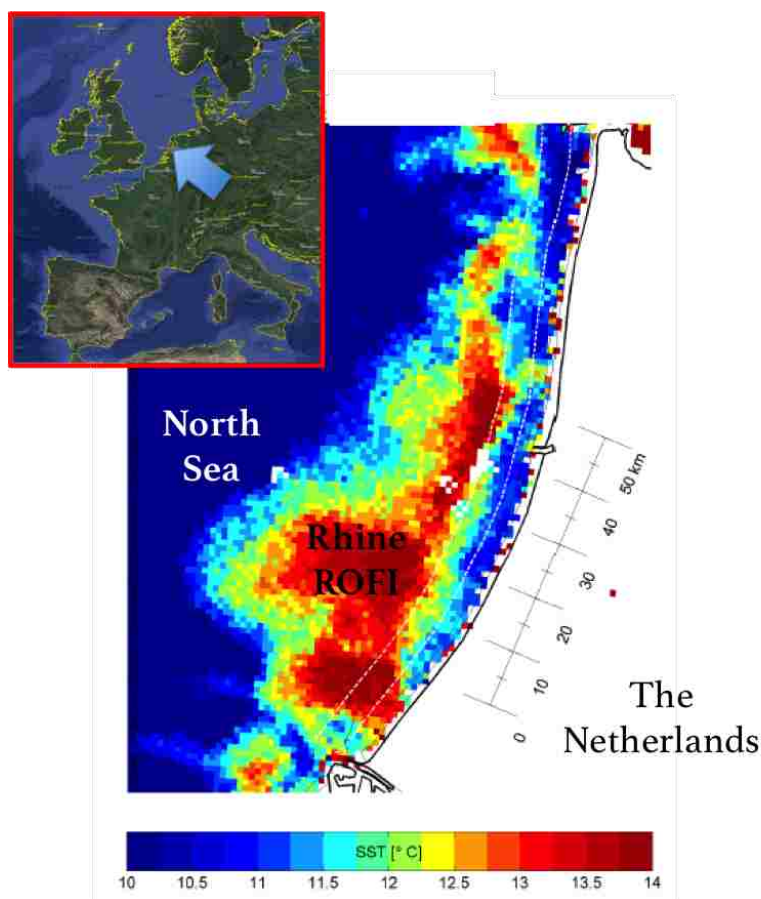
Figure 1.1: Sea surface temperature signal corresponding to the Rhine region of freshwater influence along the Dutch coast. Adapter from *De Boer* (2009). Inset shows the location of The Netherlands.

time scales, fortnightly and semi-diurnal, which are determined by tidal mixing and tidal straining, respectively. The ROFI is typically well mixed during energetic periods, such as spring tides or storms, and is stratified during low energy periods, such as neap tides.

The semi-diurnal variations in stratification are associated with the interaction between the tidal wave and the density field (*Simpson and Souza*, 1995). In this region of the North Sea, the tide behaves as a progressive Kelvin wave, hence it propagates parallel to the coast with tidal velocities in phase with tidal elevation. During well-mixed periods, tidal velocities are rectilinear and they do

not interact with the dominant cross-shore density gradient (*Visser et al.*, 1994; *Souza and Simpson*, 1997). During periods of vertical stratification, the tidal current patterns are modified and tidal ellipses become more circular, with counter-rotating top and bottom currents. This generates a strong cross-shore shear, that is able to interact with the cross-shore density gradients to create and destroy stratification (*Visser et al.*, 1994; *Simpson and Souza*, 1995).

In order to understand how the counter-rotating tidal ellipses are generated, it is useful to decompose the tidal currents into cyclonic and anticyclonic rotary components, R_+ and R_-, respectively, each one having a boundary layer height given by (*Prandle*, 1982; *Souza*, 2013)

$$\delta_\pm \sim \frac{C_0 U_*}{\omega \pm f} \tag{1.1}$$

where C_0 is a constant (*Souza*, 2013), U_* is the bottom friction velocity, ω is the tidal frequency ($M2$ component) and f is the Coriolis parameter. At mid-latitudes, $\omega \approx f$, which results in an anticyclonic boundary layer that is much greater than the cyclonic boundary layer (*Visser et al.*, 1994; *Souza et al.*, 1997),

$$\frac{\delta_-}{\delta_+} \sim 3 \tag{1.2}$$

In the Rhine ROFI, the anticyclonic boundary layer is typically greater than water depth, i.e., $\delta_- > h$. The rotary velocity components for the case of a well-mixed water column are shown in Figure 1.2a. The cyclonic component reaches its free stream velocity close to the bottom, whereas the anticyclonic component, which has a much greater boundary layer, is not able to reach its free stream velocity. In the presence of stratification and a pycnocline (Figure 1.2b), the cyclonic component is not modified. Due to the suppression of turbulence at the pycnocline, the bottom and upper layers become dynamically decoupled, which results in a modification of the anticyclonic component velocity component (*Visser et al.*, 1994; *Verspecht et al.*, 2010). As the upper layer does not feel bottom friction anymore, the anticyclonic component is free to reach its free stream velocity, which increases the anticyclonic character of surface currents. In response to the increase in anticyclonic rotation of the surface currents, the bottom currents gain cyclonic rotation in order to maintain a zero depth-averaged cross-shore flow due to the proximity of the coastal wall (*Visser*
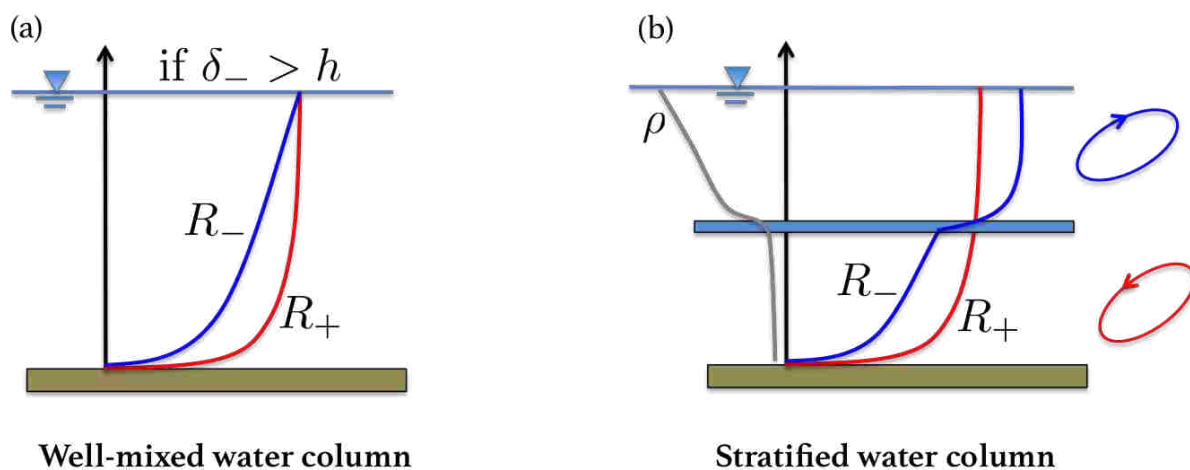
Figure 1.2: Schematic of cyclonic (R_+, red line) and anticyclonic (R_-, blue line) tidal current components for a) a well-mixed water column and b) a stratified water column.

et al., 1994) (Figure 1.2b).

The modification of tidal currents by stratification leads to the development of a strong cross-shore shear that interacts with the cross-shore density gradient to induce and destroy stratification (*Simpson et al.*, 1990; *Simpson and Souza*, 1995; *Souza and James*, 1996; *Souza et al.*, 2008). Figure 1.3b shows the near-bottom tidal ellipse, where the cyclonic rotation results in onshore flow occurring from low water (LW) to high water (HW), and offshore flow occurring from HW to LW. The interaction of the tidal flow with the cross-shore density gradients is shown in Figure 1.3c. In the Rhine, minimum stratification occurs at LW (*Simpson and Souza*, 1995; *De Boer et al.*, 2006). From LW to HW, stratification is generated by the interaction of the cross-shore velocity profile and the cross-shore density gradients. In the near-bed region, denser waters are moved over less dense waters by the onshore flow, while in the upper water column the offshore currents move lighter water over denser water. Maximum water column stratification is reached at HW (*Simpson and Souza*, 1995). From HW to LW, the cycle reverses and stratification is destroyed, and minimum stratification occurs again at LW. The interaction between the tidal shear and the horizontal density gradients that results in variations in stratification at the tidal frequency has been termed strain-induced

periodic stratification (SIPS; *Simpson et al.* (1990)) and is a characteristic feature of the Rhine ROFI. The cross-shore tidal straining mechanism shown in Figure 1.3 has been demonstrated to dominate the variations in stratification in the far field of the Rhine (*Simpson and Souza*, 1995; *De Boer et al.*, 2008).

The Rhine ROFI has been extensively studied, with most of the research centered around the structure of tidal currents (*Visser et al.*, 1994; *Souza and Simpson*, 1997; *De Boer et al.*, 2006), variability in stratification (*Simpson and Souza*, 1995; *De Boer et al.*, 2008; *Rijnsburger et al.*, 2016) and the interactions between turbulence, stratification and mixing (*Fisher et al.*, 2002; *Souza et al.*, 2008; *Fischer et al.*, 2009). The effects of these dynamics on SPM patterns and transport processes have been relatively less studied. However, measurements along the Rhine have shown the effects of stratification on the distribution and sinking rates of chlorophyll and plankton (*Joordens et al.*, 2001; *Peperzak et al.*, 2003). Similarly, ROFI stratification is found to play an important role on the distribution of suspended sediments on both short and long timescales (*Jones et al.*, 1996; *Pietrzak et al.*, 2011).

As river plumes are formed by regions that are dynamically very different (*Horner-Devine et al.*, 2015), it follows that the sediment transport processes can differ significantly between them. In the near and mid-field regions of the Rhine ROFI, the onshore propagation of freshwater lenses that are periodically ejected from the estuary (*Rijnsburger et al.*, 2018) leads to offshore fluxes of fine sediments in the lower half of the water column (*Horner-Devine et al.*, 2017). On the other hand, in a study site located 80 km north of the river mouth, *van der Hout et al.* (2015) reported a persistent mid-shelf turbidity maximum zone (TMZ) with peak concentrations located 1.251.5 km from the coast. Additional observations along the Dutch coast (*Van Alphen*, 1990; *Simpson et al.*, 1993; *Joordens et al.*, 2001), suggest that this coastal TMZ may extend all over the ROFI.

This TMZ is undoubtedly the main feature of fine sediment dynamics along the Rhine ROFI, and several mechanisms have been hypothesized to contribute to its formation and maintenance (*Visser et al.*, 1991; *van der Hout et al.*, 2015). In this thesis, we discuss two of them extensively: the downslope (offshore) movement of gravity-driven sediment flows (see Chapter 3) and cross-
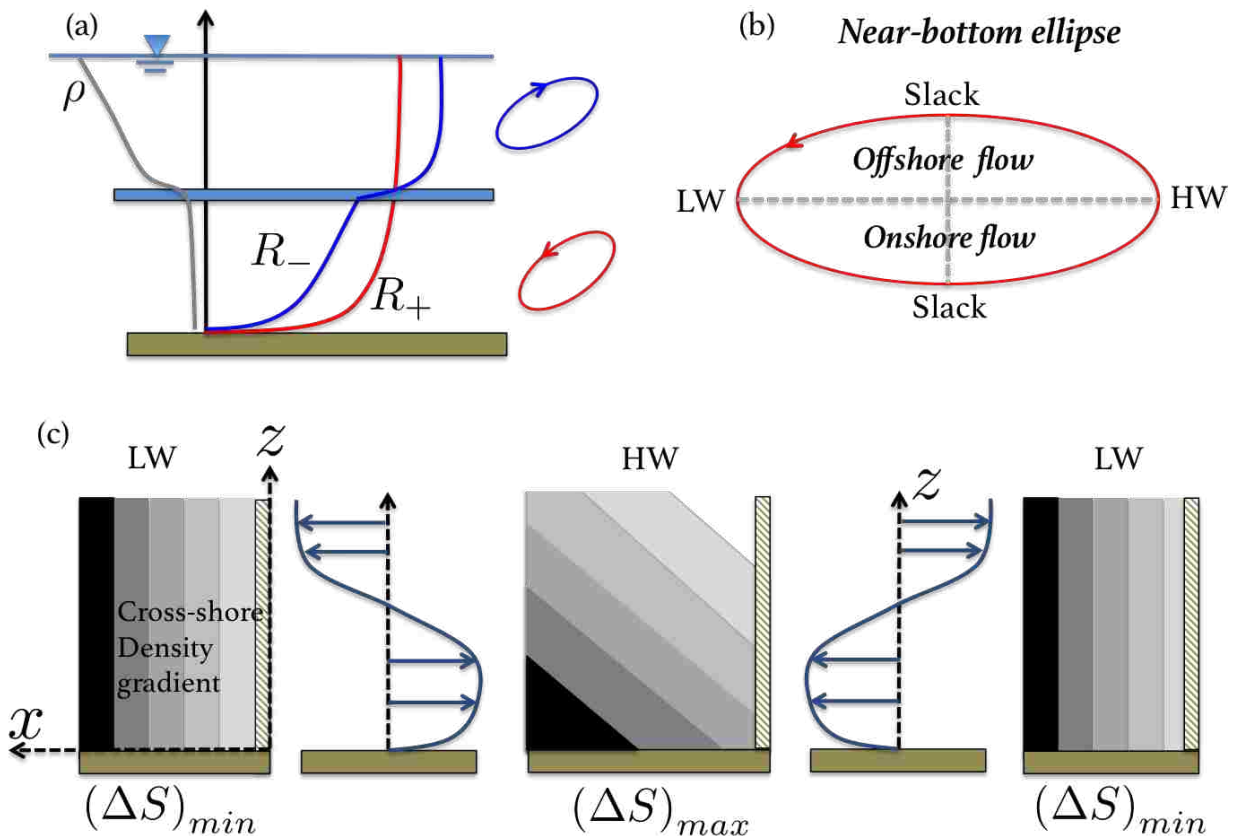
Figure 1.3: Schematics of the cross-shore tidal straining mechanism along the Rhine ROFI. (a) Cyclonic (R_+, red line) and anticyclonic (R_-, blue line) tidal current components for a stratified water column. (b) Near-bottom tidal ellipse, which rotates cyclonically (anti-clockwise in the Northern Hemisphere) (c) Cross-shore straining mechanism. Colors are associated to water density (darker is denser). ΔS refers to top-bottom salinity difference. LW: low water (peak ebb), HW: high water (peak flood). The cross-shore tidal shear resulting from the modification of tidal ellipses interacts with the horizontal density gradient to create and destroy stratification at the tidal frequency.

shore tidal straining (see Chapter 4). We also discuss mechanisms leading to cross-shore sediment transport in the mid-field region of the ROFI, in particular, the interplay between the effects of storms and stratified periods (see Chapter 2).

1.4   Thesis outline

This thesis is largely based on field measurements taken during the STRAINS (STRAtification Impacts on Nearshore Sediment transport) campaign in September-October 2014, at a site located 10 km north of the Rhine River mouth. These measurements are presented in the following chapters, and included detailed time series of tidal currents, salinity, suspended sediment concentrations and near-bed turbulence and morphology. In Chapter 2, we use field measurements to evaluate the impact of storms and water column stratification on the cross-shore transport of fine sediments in the mid-field plume region of the Rhine ROFI. The relevance of barotropic and baroclinic processes is discussed, and the dominant modes of transport are identified. This chapter has been reproduced with minor changes from,

Flores, R.P., Rijnsburger, S., HornerDevine, A.R., Souza, A.J. and Pietrzak, J.D., 2017. The impact of storms and stratification on sediment transport in the Rhine region of freshwater influence. Journal of Geophysical Research: Oceans, 122(5), pp.4456-4477.

In Chapter 3, we document the occurrence of a wave supported gravity-driven flow (WSGF) during an intense 2-day storm. These observations are the first to show the occurrence of a WSGF on a predominantly sandy seabed. The dynamics of the WSGF is discussed and the field data is compared against theoretical predictions. Different approaches to the modeling of WSGF are discussed in terms of their applicability on sandy sites. The contents of this chapter have been reproduced with minor changes from,

Flores, R. P., Rijnsburger, S., Meirelles, S., Horner-Devine, A. R., Souza, A. J., Pietrzak, J. D., et al. (2018). Wave generation of gravity-driven sediment flows on a predominantly sandy seabed. Geophysical Research Letters, 45. https://doi.org/10.1029/2018GL077936.

Chapter 4 presents results from an idealized numerical model in order to investigate the influence of tidal straining in the generation of a coastal turbidity maximum zone along the Rhine ROFI. The physical mechanisms leading to cross-shore sediment convergence are discussed, and a parameter space for the occurrence of tidal straining and a coastal TMZ is provided in terms of density gradients and the Coriolis parameter as a function of latitude.

Chapter 5 presents near-bed turbulence and bedform measurements collected during the STRAINS campaign. The effects of bedforms on the estimation of bottom stress are discussed, and a methodology (based on existing models) to incorporate non-equilibrium bedform dynamics into bed stress calculations is outlined. Fine sediment resuspension dynamics are discussed in terms of the vertical turbulent sediment fluxes.

Lastly, Chapter 6 provides a summary and a discussion of future directions on these topics.

Chapter 2

THE INFLUENCE OF STORMS AND STRATIFICATION ON SUSPENDED SEDIMENT TRANSPORT IN THE RHINE REGION OF FRESHWATER INFLUENCE

2.1 Introduction

Rivers deliver significant amounts of freshwater and sediment to the ocean (*Dagg et al.*, 2004; *Milliman and Syvitski*, 1992), creating buoyant plumes that become the interface between estuaries and continental shelf seas. Upon exiting the estuary, the influence of Earth's rotation eventually turns riverine freshwater anti-cyclonically (to the right in the Northern hemisphere), establishing a narrow current that can flow tens of kilometers along the coast (*Fong and Geyer*, 2001, 2002; *Pietrzak et al.*, 2002; *Horner-Devine et al.*, 2015). Consequently, river plumes are critical in determining the advection, dispersion and redistribution of sediments, pollutants and biota, thus controlling primary productivity and several other environmental issues in coastal regions.

Circulation dynamics in river plumes are largely baroclinic and vary significantly according to riverine freshwater discharge, tidal amplitude, coastline geometry, ocean currents, wind stress and the effect of Earth's rotation (*Horner-Devine et al.*, 2015). In shallow tidal systems, such as the Rhine (*Simpson*, 1997) or Liverpool Bay (*Verspecht et al.*, 2009a, 2010), bottom friction is also relevant by setting the cross-shore extension of the plume and the scale of the bottom boundary layer, which can often influence a large portion of the water column. These systems are often referred to as Regions of Freshwater Influence (ROFIs). In these systems, tidal current structure and the vertical distribution of SPM (Suspended Particulate Matter) responds directly to the onset and destruction of stratification, which in turn is determined by the interaction between the freshwater plume and tidal, wind and wave mixing processes (*Simpson and Souza*, 1995; *Visser et al.*, 1994; *Joordens et al.*, 2001; *Peperzak et al.*, 2003).

The outflow discharge from the Rhine river into the shallow and highly energetic coastal areas of

the Southern North Sea sustains a large ROFI, that extends for over 100 km along the Dutch coast and, on average, remains concentrated within a 20 km-wide coastal strip (*De Kok*, 1996; *Pietrzak et al.*, 2011). Three main dynamical regions can be distinguished (*Garvine*, 1984; *Hetland*, 2005; *Horner-Devine et al.*, 2009, 2015): the near-field, where the momentum of the plume layer dominates over its buoyancy, the mid-field, where Earth's rotation begins to dominate and turns the plume in the down coast direction, and the far-field, where a buoyant density current has been established flowing parallel to the coast towards the northeast. Physical processes leading to the switching of stratification, the modification of tidal currents and mid-shelf sediment accumulation have been extensively studied in the far-field (*Simpson and Souza*, 1995; *van der Hout et al.*, 2015; *De Boer et al.*, 2006; *Rijnsburger et al.*, 2016), where cross-shore tidal straining (*Simpson et al.*, 1990) plays a key role. Closer to the river mouth, in the mid-field region, the tidal advection of freshwater lenses strongly modifies stratification and current patterns from those observed in the far-field (*Van Alphen et al.*, 1988; *Horner-Devine et al.*, 2017), with effects on transport processes that have not yet been fully investigated.

The potential impact of river plume processes on SPM transport dynamics has gained much relevance over the last few decades, especially in light of the pressure that large-scale engineering projects have exerted on the morphodynamics of coastal areas. For the particular case of the Dutch coast, the completion of the Sand Engine (*Stive et al.*, 2013; *de Schipper et al.*, 2016) in 2011 and the construction of an extension of the Port of Rotterdam have introduced modifications to the morphology of the coastline and nearshore SPM transport patterns. The Sand Engine is a 21.5 million m^3 sand nourishment located 10 km north of the Rhine River mouth, built to protect the beaches and dunes along the Dutch coast from erosion and provide a defence to flooding of the low-lying lands of The Netherlands (*Stive et al.*, 2013).

SPM regimes in river plumes are different from those of wave-dominated environments in the nearshore and those of shelf seas. Stratification leads to the suppression of turbulence at the pycnocline (*Geyer*, 1993; *de Nijs et al.*, 2010), trapping suspended matter below it. The continuous change between stratified and well-mixed conditions in shallow river plumes, such as the Rhine, complicates the task of inferring subsurface SPM fluxes from remote sensing data or surface mea-

surements (*Pietrzak et al.*, 2011; *van der Hout et al.*, 2015). *Geyer et al.* (2004) concluded that sediment transport in river-influenced regions is often dominated by near-bottom fluxes, which suggests that near-bed measurements are required to avoid erroneous conclusions about the magnitude and direction of transport.

In this chapter, we will present field measurements taken 1 km offshore and 10 km north from the Rhine River mouth (in the vicinity of the Sand Engine) in order to investigate the sediment fluxes in a shallow mid-field plume region, a region strongly influenced by the propagation of tidally-generated freshwater lenses as well as processes characteristic of the far-field. We give a global description of sediment dynamics in the inner shelf region of the ROFI and their response to storms (barotropic) and stratified (barocilinic) periods. The analysis is focused on the identification of the underlying physical mechanisms that determine the direction and intensity of sediment transport, emphasizing near-bottom dynamics that are dominated by higher concentrations and larger particle sizes relevant for coastal morphodynamics. The chapter is organized as follows: Section 2.2 gives an overview of previous work that is relevant for the analysis we present in this study. Section 2.3 describes the measurements, conditions and methods. Density, current structure, suspended sediment concentrations and results for the suspended sediment fluxes are presented in Section 2.4. Section 2.5 presents a discussion of the findings and the role of stratification on transport processes in the mid-field region of the Rhine ROFI, and Section 2.6 presents the conclusions.

2.2 Background

Processes leading to SPM transport in the Rhine ROFI are strongly tied to density stratification patterns (*van der Hout et al.*, 2015; *Joordens et al.*, 2001). Variations in stability of the Rhine ROFI occur at different timescales (*Simpson et al.*, 1993; *Simpson*, 1997). The fortnightly cycle of the tides imposes a predictable variation in the tidal mixing component, that is reflected in a neap-spring time scale variation in stratification. Superimposed on tidal processes, the variability in wind and wave forcing, along with a time-dependent river discharge often produce sources of stratification variability in a much shorter timescale.

Observations in the far-field of the Rhine ROFI (40-80 km from the river mouth) show a semi-

diurnal variation during periods of stratification (*Simpson et al.*, 1993; *Simpson and Souza*, 1995). In this region of the North Sea, the tide is dominated by the M2 semidiurnal component and is well described by a progressive Kelvin wave traveling to the northeast, with tidal velocities in phase with tidal elevation. Tidal straining results from the interaction of the tidal shear with the horizontal density gradients, alternately inducing and destroying stratification at the tidal frequency (*Simpson et al.*, 1990). Stratification develops during during the flood, reaching its maximum at local high water (*De Boer et al.*, 2006). The process is reversed during the ebb tide, such that minimum stratification occurs at low water. Strain-induced stratification requires the occurrence of strong cross-shore exchange currents, which cannot come from the barotropic tidal currents that tend to be parallel to the coast. The generation of strong cross-shore currents is explained by the modification of tidal ellipses due to the effect of stratification (*Visser et al.*, 1994; *Verspecht et al.*, 2010). Tidal current vectors show elliptical trajectories in the horizontal plane, and can be decomposed in two counter-rotating phasors (*Prandle*, 1982). Following Ekman dynamics, the one that rotates opposite to Earth's rotation has a much greater boundary layer thickness than the component that rotates in the same direction as the Earth. The onset of stratification decouples the water column at the pycnocline by reducing the eddy viscosity (*Visser et al.*, 1994), and the upper layer is free to move under the barotropic forcing. This increases the amplitude of clockwise (anti-cyclonic) currents at the surface with respect to the unstratified case. Due to the proximity of the coast, near-bottom currents become more cyclonic such that at any time the depth-averaged cross-shore velocity is zero because of continuity constraints (*De Boer et al.*, 2006). This combined effect creates a strongly sheared cross-shore flow, with cross-shore currents that show 180° phase difference between the surface and bottom, and maximum stratification is achieved at times of the maximum relative displacement between the lower and upper layers. *Simpson and Souza* (1995) first realized the two-way interaction between the cross-shore density gradients and semidiurnal counter-rotating currents in the Rhine ROFI.

In this work we refer to tidal straining as the generation of counter-rotating tidal ellipses by vertical stratification, resulting in the cross-shore tilting of the isopycnals (*Visser et al.*, 1994; *Simpson and Souza*, 1995). In the Rhine ROFI there are several other straining mechanisms that contribute to the generation of stratification and transport processes, which are described in detail in *De Boer*

et al. (2008). Our definition of tidal straining corresponds to the term S_x in *De Boer et al.* (2008) and *Rijnsburger et al.* (2016).

In the absence of stratification (barotropic conditions), Earth's rotation induces small ellipticities that result in cross-shore currents during both neap and spring tides (*De Boer et al.*, 2006). It is important to note that these cross-shore currents are just a small fraction of the dominant along-shore velocities, but still allow for cross-shore exchange during energetic storm periods with strong wind and wave mixing.

Closer to the river mouth, additional processes generate different stratification and current patterns from those observed in the far-field (*Van Alphen et al.*, 1988; *De Boer et al.*, 2008). The discharge of the Rhine River is strongly modulated by the semidiurnal tidal wave propagating into the estuary. Consequently, freshwater enters the coastal zone as a series of periodic pulses released during ebb tide (*de Ruijter et al.*, 1997) generating strong fronts on their boundaries that are similar to tidal plume fronts observed in other systems, such as the Connecticut (*Garvine*, 1974, 1977) and Columbia (*Horner-Devine et al.*, 2009) River plumes. Freshwater lenses have been observed to propagate northeastwards along the Dutch coast at velocities up to 0.5 ms^{-1}, while undergoing strong mixing and deformation before being incorporated to the plume (*de Ruijter et al.*, 1997). Fronts have also been observed to propagate all the way to the beach generating rapid current responses in the lower layer (*Horner-Devine et al.*, 2017), in addition to strong density gradients in time and space.

In the mid-field region, the frontal processes characteristic to the near-field and the tidal straining processes characteristic of the far-field interact, as shown by *De Boer et al.* (2008). Moreover, the counter-rotating velocity field generated by tidal straining results in the onshore and offshore advection of the entire ROFI, generating a periodic front that is displaced by over 7 km each tidal cycle (*Simpson and Souza*, 1995) that interacts with the ejected freshwater lenses. This interaction likely results in asymmetric processes driven by the timing of the freshwater lenses, with the potential of impacting cross-shore exchange.

Cross-shore circulation patterns and associated transport processes are also influenced by wind forcing, especially during storms. In recent years, cross-shelf winds have been shown to generate cross-shore exchange flows aligned with the wind stress in shallow inner shelf regions where the surface and bottom boundary layers overlap (*Lentz*, 1995; *Lentz and Fewings*, 2012). *Fewings et al.* (2008) demonstrated that alongshore winds at a location in 12m of water do not drive substantial cross-shelf circulation (as opposed to the mid and outer shelf) and that circulation is driven by the cross-shelf wind, wave forcing and tides. Wind stress has also been shown to be one of the dominant terms in the depth-averaged momentum balance at depths less than 30m (*Fewings and Lentz*, 2010; *Gutierrez et al.*, 2006), where it balances the pressure gradient (coastal setup or setdown) induced mainly by the cross-shore winds.

Many investigations in the Rhine ROFI have shown the effects of haline stratification on the vertical distribution of sediment (*Pietrzak et al.*, 2011; *van der Hout et al.*, 2015) and the sinking rates of chlorophyll and phytoplankton (*Peperzak et al.*, 2003; *Joordens et al.*, 2001). *Pietrzak et al.* (2011) showed that high SPM values can be observed near the surface over the full extension of the plume when the Rhine ROFI is well-mixed in the vertical, whereas during stratified periods SPM is not visible in the near-surface layer as it gets trapped below the pycnocline. This was also reported by *Joordens et al.* (2001) and more recently by *van der Hout et al.* (2015), using cross-shore transects at different locations along the Dutch coast.

In-situ SPM transport studies in the Rhine ROFI have been mostly conducted at distances greater than 40 km from the estuary mouth in the far-field plume (*McCandliss et al.*, 2002; *Van Alphen*, 1990; *van der Hout et al.*, 2015). At a study site located 80 km north of the river mouth, *van der Hout et al.* (2015) reported that the accumulation of SPM in the cross-shore direction over a year is a significant percentage of the yearly residual alongshore transport, leading to a persistent mid-shelf turbidity maximum zone with peak concentrations located 1.25-1.5 km from the coast. Furthermore, they suggest that the nearshore presence of turbidity maximum is strongly influenced by processes related to stratified plume dynamics, such as asymmetry in cross-shore straining.

In one of the few in-situ SPM studies located in the mid-field region, *Horner-Devine et al.* (2017)

described a new cross-shore exchange mechanism in which the tidally generated front from the Rhine River outflow propagates onshore and drives suspended sediment from the surfzone 2-3 km offshore. This mechanism involves the interaction between near-shore wave-induced sediment resuspension and plume-generated pulses of seaward velocity in the lower layer due to the onshore propagation of the front near the surface. In their study, *Horner-Devine et al.* (2017) found that suspended sediment transport measured at a mooring located at 12m depth and 10 km north of the Rhine River mouth was strongly dominated by pulses of seaward transport that were timed with the passage of the tidal plume front. Based on the timing of elevated SSC relative to the front, low bed stresses and high cross-shore velocities, they conclude that the transport pulses are the result of advection from the surf zone region rather than local resuspension. This new mechanism provides a link between the shoreline and offshore coastal waters through the interaction of baroclinic river plume processes and surfzone wave activity. Transport due to frontal pumping dominated the cross-shore flux during the 2013 experiment and this process is also observed in the data from the 2014 experiment presented here (see our Figure 2.9). One of the objectives of the present study is to determine whether this mechanism dominates transport dynamics close to the river mouth under a different set of forcing conditions.

2.3 Setup and methods

2.3.1 Measurements

Field observations were carried out from 15 September to 28 October (year days 258 to 301), 2014, comprising almost two complete neap-spring cycles. These measurements are part of a large scientific field campaign called STRAINS (Stratification Impacts on Nearshore Sediment Transport), which focused on the role of ROFI processes and stratification on sediment transport near the Sand Engine and their implications along the Dutch coast. Two moorings were deployed approximately 10 km north-east of the mouth of the Rotterdam waterway at nominal depths of 12m and 18m, corresponding to 1.5 and 6 kilometers from the coast, respectively (Figure 2.1a).

The moorings were located in the mid-field region of the Rhine ROFI, i.e., within the excursion of the tidal plume front generated by the freshwater outflow from the Rhine. The moorings were designed
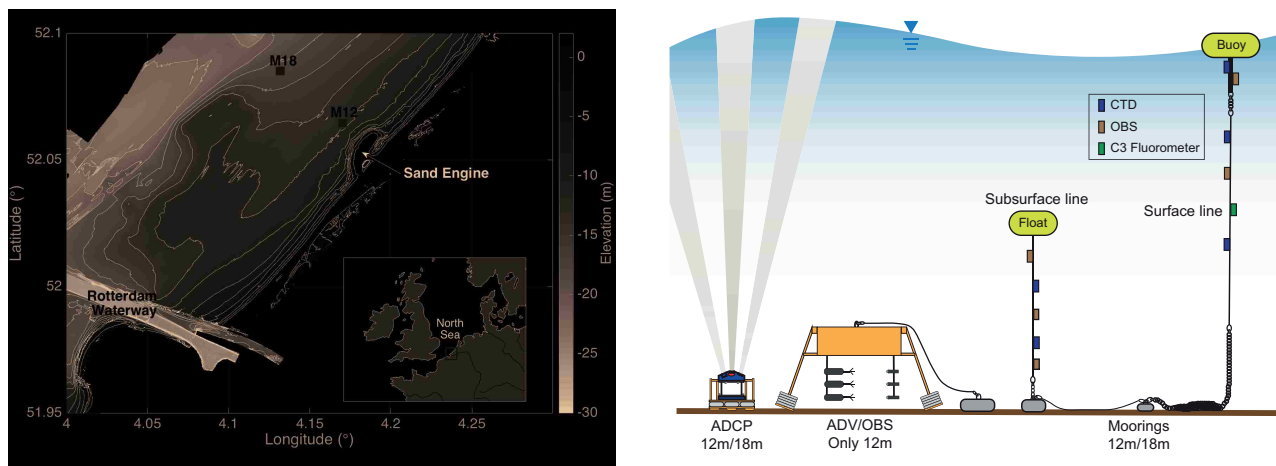
Figure 2.1: Study area and Moorings. (Left) Dutch coast near the Rhine river mouth. Red squares mark the location of moorings and bottom frames at 12m and 18m depth. (Right) Instrumentation schematics. Moorings at each site were spaced by 50 m.

to measure vertical profiles of conductivity, temperature, pressure and suspended sediment concentration throughout the water column using arrays of CTDs (Conductivity-Temperature-Depth) and OBS (optical backscatter) sensors, from which salinity and density profiles were derived. Five CTDs (Seabird) and five OBSs were placed at the 12 m mooring, whereas four CTDs and five OBSs were placed at 18m depth, providing a detailed description of both salinity and sediment concentrations throughout the tidal cycle. A schematic of the 12m mooring is shown in Figure 2.1b. Sampling periods were typically 30 seconds, but ranged between 20 and 50 seconds depending on the instrument. OBS sensors were intercalibrated using formazine solutions prior to deployment in the laboratory in order to account for sensor sensitivity and the data was converted to mass concentrations using a conversion based on over 400 bottle samples collected by the Port of Rotterdam in this region of the Dutch coast.

Vertical profiles of current speed were measured at each location using a bottom-mounted 4 beam Acoustic Doppler Current Profiler (ADCP; 1200 kHz RDI WorkHorse), sampling at 1 Hz, with the first bin centered approximately 1.5 m above the seabed and vertical resolution of 0.25 m (bin size).

The raw data were averaged into 10 minute blocks to obtain mean current profiles, and the N-E velocity components were rotated to alongshore and cross-shore components using the inclination of the major axis of the tidal ellipses, which resulted in a rotation angle of 42.5 degrees from the North. Alongshore velocities are positive towards the northeast and cross-shore velocities are positive in the offshore direction. The harmonic analysis done to obtain tidal ellipses was performed using the T-TIDE code (*Pawlowicz et al.*, 2002).

Hydrodynamic flow conditions were complemented with the measurement of 3D near-bottom dynamics and turbulence at the 12m site, using three synchronized 6MHz Sontek Acoustic Doppler Velocimeters (ADV), sampling at 16 Hz and mounted on a frame 0.25, 0.5 and 0.75 m above the bottom, respectively. The ADVs were mounted on an arm away from the frame to avoid turbulent perturbations due to the frame itself. The raw ADV data were quality controlled and de-spiked using the three-dimensional phase space algorithm of *Goring and Nikora* (2002). Near-bottom mean tidal velocities were estimated by time averaging over a 10-min period, and turbulent velocity components u', v' and w' were obtained by removing the tidal trend. The mean and the turbulent horizontal velocity components were rotated to alongshore and cross-shore components, using the same procedure as with the ADCP velocities. Colocated fast sampling OBSs were also deployed and synchronized with the ADVs to measure near-bottom concentrations and fluxes (Figure 2.1b).

2.3.2 Conditions

Figure 2.2 shows the forcing conditions observed during the deployment. The Rhine River discharge ranged from approximately 500 m^3s^{-1} to 2500 m^3s^{-1}, with a mean value of 1500 m^3s^{-1}, which corresponds to a 60% of the annual mean. The mean wind intensity was approximately 6.4 ms^{-1}, but variability was high in both magnitude and direction throughout the experiment. At the start of the deployment wind speeds were low (5 ms^{-1}), predominantly from the east. Winds intensified significantly during the first storm from days 264 to 266, reaching peak speeds of nearly 15 ms^{-1} persistently from the north. Towards the middle of the experiment winds decreased and ranged between 3 to 7 ms^{-1}, but an acute peak of 17 ms^{-1} was observed on day 278. Southerly winds on the order of 10 ms^{-1} were persistently observed during the second storm on days 280 to

284.

Wave statistics were measured with a Waverider buoy located 1 km to the southwest of the 12 m mooring. Significant wave heights followed winds closely, remaining less than 1 m for almost half of the deployment but peaking at nearly 2.5m during the first storm and 1.5m during the second storm (Figure 2.2b). Differences in wave heights between storms are attributed to wind direction; for the first storm winds were blowing from the north with a much greater fetch. Wave periods were generally less than 4s, but peaked at almost 6s during storms.

Tides in the vicinity of the Rhine ROFI are semidiurnal with amplitudes in the range of 1 to 2 m. During neap tides (see black periods on Figure 2.2 c), the maximum tidal range was 1.6 m, whereas during spring tides (red periods Figure 2.2 c) the maximum tidal range was 2.3 m.

2.3.3   *Calculation of friction velocities and sediment fluxes*

Reynolds stresses $\overline{u'w'}$ and $\overline{v'w'}$ can be estimated directly from the time-averaged correlations in turbulent velocity components, using the covariance method (*Kim et al.*, 2000). Provided the turbulence measurements are located within the bottom boundary layer, bottom stresses can be obtained as $\tau_b = \rho \left(\overline{u'w'}^2 + \overline{v'w'}^2 \right)^{1/2}$, where ρ is the density of seawater.

The separation of shear stresses exerted on the bed by the tidal currents and wave motion is a necessary step to investigate the dynamics of sediment resuspension in shallow depths subjected to wave forcing. As noted in Figure 2.2, wave heights up to 2.5 m were observed during storm periods, which would certainly make bottom shear stresses estimates unreliable since wave motions likely penetrate all the way to the seabed. To reduce the wave-induced bias on the Reynolds stresses we use the linear filtration technique proposed by *Shaw and Trowbridge* (2001), which relies on 2 ADVs separated by a vertical distance larger than the length scale of the turbulent eddies (which scale with the vertical distance from the bottom) but smaller than the correlation scale of wave motion. Here, we have used a vertical separation between instruments of $\Delta z = 0.5$ m using our lowest and highest ADVs. Figure 2.3a shows the covariance of turbulent velocity components and
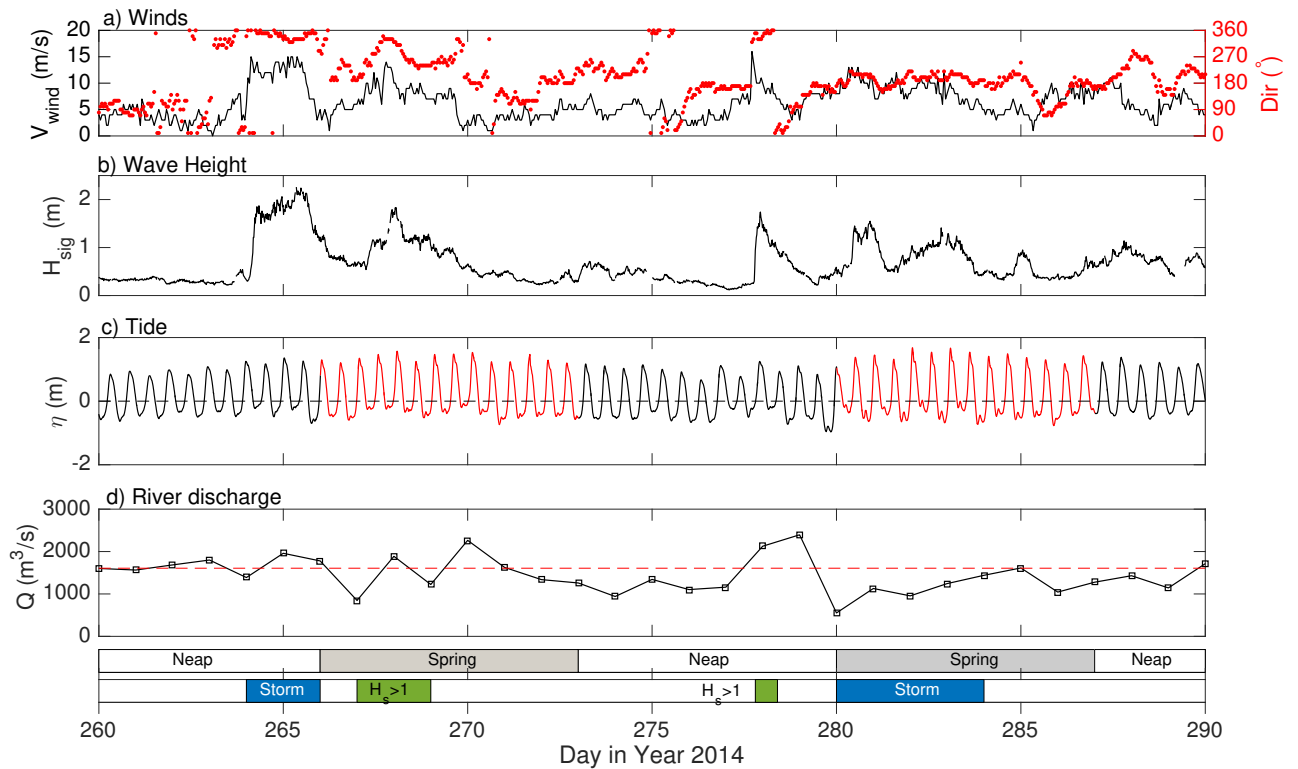
Figure 2.2: Conditions. (a) Wind speed (solid black line) and wind direction (solid gray line). Meteorological convention is followed. (b) Significant wave height from Waverider buoy. (c) Tidal elevation measured at Scheveningen station. Colors indicate neap (black) and spring (red) tide. (d) Rhine River discharge. Dashed red line represent the average discharge for the study period. Bars indicate spring/neap periods and the occurrence of storms and $H_{sig} > 1$ (m).

the Reynolds stresses after the removal of wave contamination, for a period centered around the first storm. Both estimates give very similar values when wave activity is low, but differ considerably during energetic conditions when wave-induced turbulence is significant. Frequency spectra for one burst is shown as an example of the turbulence decomposition method in Figure 2.3b. For this burst, indicated by the vertical line in Figure 2.3a, the influence of wave motions is significant in the range from 0.07 to 0.3 Hz. Agreement with the -5/3 slope characteristic of the inertial subrange for frequencies above 1 Hz confirms that the instruments are resolving turbulence over a decade of frequencies in the inertial subrange, even in the presence of large waves. Bottom shear stresses due to current-induced turbulence were estimated from the wave-filtered Reynolds stresses, and the current friction velocity was calculated as $u_{*c} = \sqrt{\tau_b/\rho}$.

Representative wave parameters at our 12m site were computed using the high-frequency ADV velocity measurements. Representative bottom orbital velocity (u_{br}) and the representative wave frequency associated to u_{br} were obtained from the frequency spectra of horizontal velocities, following *Madsen* (1995) and *Wiberg and Sherwood* (2008). Maximum wave-induced stresses at the bed are commonly parametrized in terms u_{br} and a wave friction factor f_w as $\tau_{bw} = \frac{1}{2}\rho f_w u_{br}^2$. In field conditions we expect to have a hydraulically rough bed due to the presence of bedforms and sediment transport processes, particularly if the bed is sandy and exposed to waves capable of moving sediment. Therefore, we expect the wave friction factor to fall within the rough turbulent regime such that f_w is only a function of the relative roughness parameter, $f_w = f(k/a_b)$, where k is the bed roughness and a_b is the maximum wave orbital excursion. Bed roughness is hard to measure in the field and is usually estimated indirectly using the particle size of bottom sediment. The wave friction factor is computed by $f_w = \exp\left(5.213(k/a_b)^{0.194} - 5.977\right)$ (*Swart*, 1974), which is a commonly used parametrization for hydraulically rough flows in mobile beds. In the absence of bedform information, bed roughness was taken as $k = 2d_{50}$ (obtained from samples of bed sediment) and orbital excursion is computed as $a_b = u_{br}/\omega$, where ω is the wave frequency. Wave friction velocity is obtained as $u_{*w} = \sqrt{\tau_{bw}/\rho}$.

Suspended sediment fluxes are computed directly from observations. Near-bottom sediment fluxes are computed using the 3 synchronized ADV and OBS measurements available from the bottom
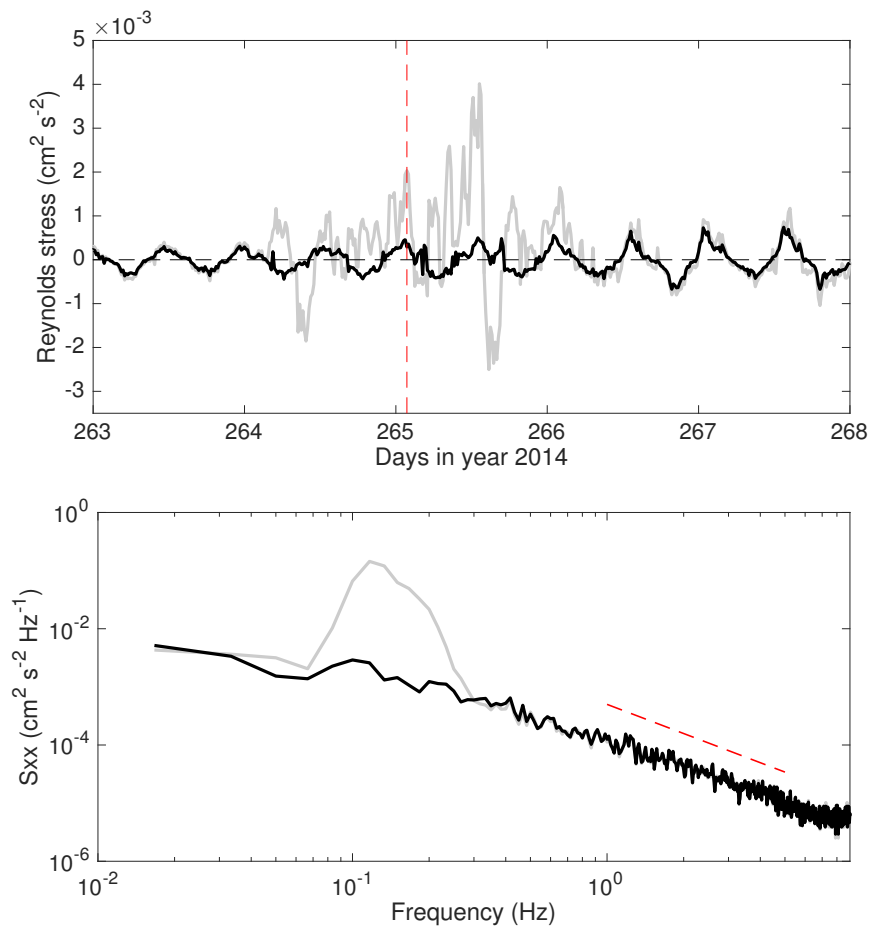
Figure 2.3: Wave-turbulence decomposition. (a) Turbulent stresses after wave removal (black line) and covariance of combined wave and turbulent velocities (gray line). (b) Spectral density for the x-velocity component before and after wave removal (gray and black lines, respectively). Red dashed line indicates the -5/3 slope. The time of the burst for which spectrum is shown is indicated by the red vertical line in panel (a).

frame, which are averaged to obtain a representative value for the near-bottom suspended sediment fluxes. Near-surface fluxes were computed using a 1 m averaged velocity window (ADCP data) around the OBS sensor, placed in the surface line of the mooring (4m below surface). Total fluxes, i.e. top to bottom, were computed by interpolating the OBS measurements onto the ADCP velocity grid. This calculation was not sensitive to the interpolation method, and linear interpolation between sensors was used.

2.4 Results

2.4.1 Density and current structure

The vertical and cross-shore structure of the observed density and velocity fields were highly variable during the observational campaign (Figure 2.4). Here we summarize the observed variability, focusing specifically on the relative influence of tidal straining, stratification, storms and fronts on sediment transport. A more detailed description of the physical processes that dictate the plume behavior during this period will be described in subsequent work.

The beginning of the observational record (days 260-264) coincided with neap tides and low wind and wave mixing, which allowed the development of persistent and periodic stratification. The maximum top-bottom salinity difference was 8 psu and the mean was 3.5 psu, while maximum near-bottom currents were on the order of 0.3 ms^{-1} during flood tide. Tidal mixing is never sufficient to destroy stratification during these low-energy conditions, and the counter-rotating tidal straining velocity field is evident in the highly sheared cross-shore current structure (Figure 2.4 c). The signature of the plume front is observed as a sudden drop in surface density, associated with onshore surface velocities. Similar behaviour is observed during the second neap tide period (days 273-280), where winds and waves remained less than 5 ms^{-1} and 1 m, respectively. Cross-shore current structure is dominated by onshore currents near the bottom, whereas offshore currents occur persistently in the top layer (except when the front is passing over the mooring). Depth-averaged alongshore currents during neap tides were on the order of 0.4-0.6 ms^{-1}.

Our observations show that storms can effectively eliminate vertical stratification in this mid-field

plume region. A big storm is observed during days 264-266, where wind speeds on the order of 15 ms^{-1} from the north and wave heights greater than 2 m (Figure 2.2) resulted in the complete homogenization of the water column (Figure 2.4a). The state of local vertical mixing at our 12m site is primarily set by the combination of direct wind mixing and the offshore advection of the entire plume due to Ekman transport. During this event, cross-shore velocities are severely reduced as the effect of stratification on the velocity field is suppressed and currents become unidirectional throughout the water column (Figure 2.4b and c). Similar effects were observed during the second storm (days 280-284), however, lower wind speeds and wave heights (Figure 2.2a) allowed for weak stratification in the top-layer (1-3 m) at certain times.

The current and density structure during spring tides with weak to moderate wind forcing (less than 8 ms^{-1}) responded differently according to wind direction. During spring tide days 267-270, the winds are downwelling favorable, which shifts the freshwater toward the coast. This shift is evident in the daily averaged salinities (not shown), which are lower during this period than any other time in the observational period and also a maximum in the cross-shore density difference. This period is also marked by strong fronts, which might be strengthened by the onshore wind forcing. Under these conditions, surface currents were persistently directed offshore while bottom currents are directed towards the coast, similar to a classic density-driven circulation profile (Figure 2.4c). This cross-shore flow structure has been previously observed in the Rhine ROFI by *Souza and Simpson* (1997) and *Souza et al.* (1997) in response to large horizontal density gradients. The signature of the tidal plume front was still strong in both density and velocity fields, with strong offshore current pulses at depth observed in response to a fast moving front with onshore surface velocities (Figure 2.4a,c). On the other hand, wind magnitude and direction during spring days 284-287 (see Figure 2.2a) were highly variable and allowed for both mixed and stratified periods. The relaxation of winds during day 284 resulted in an immediate onset of stratification, whereas stronger winds favoring the offshore or northeastwards movement of the plume during days 285-287 led to more a vertically mixed state with freshwater observed only in the top CTD sensor. However, forcing was not strong enough to eliminate the presence of fronts at our site. Under these conditions, offshore currents seem to dominate cross-shore current structure, particularly in the top layer (Figure 2.4 c). Maximum depth-averaged alongshore currents were on the order of 1 ms^{-1} for
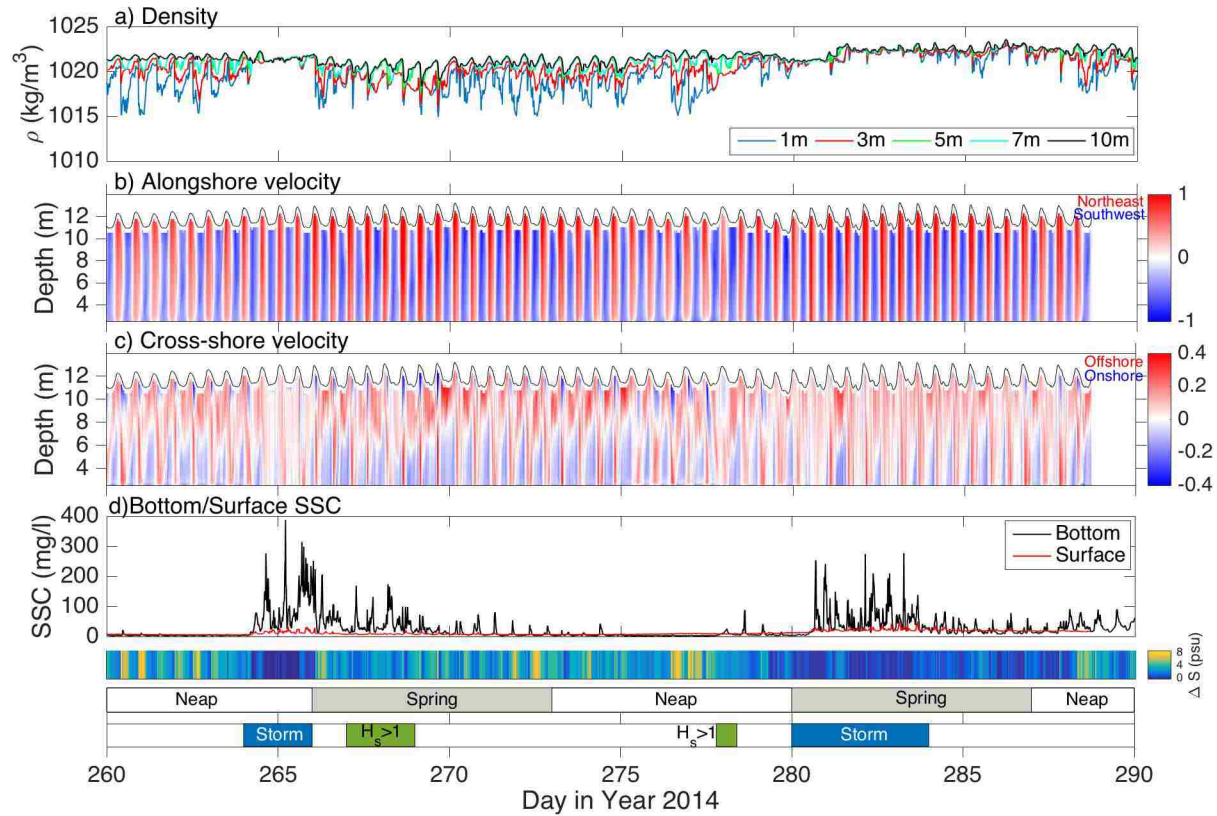
Figure 2.4: Density, current structure and SSC at 12m mooring. (a) Density. (b) Alongshore velocity (ms^{-1}). (c) Cross-shore velocity (ms^{-1}) (d) Near-bottom (black line) and near-surface (red line) suspended sediment concentration. Bottom bars show vertical stratification in terms of top-bottom salinity difference ΔS (psu), neap/spring and storm periods, and the occurrence of $H_{sig} > 1$ (m).

both spring tide periods.

2.4.2   Suspended sediment concentrations and fluxes

Sediment concentrations were highly variable during the study period and reveal the importance of wave forcing in sediment resuspension in this shallow ROFI region. We observe peak near-bottom concentrations on the order of 400 mgl^{-1} during storms (Figure 2.4d); however, significantly lower peak near-bottom concentrations around 80 mgl^{-1} during spring tides and 40 mgl^{-1} during neap tides were observed during calm periods with wave heights less than 1 m. The influence of large waves on sediment resuspension is examined by comparing SSC and wave and current friction velocities (Figure 2.5). No correlation between near-bottom suspended sediment concentration and tidal friction velocity u_{*c}^2 is observed when the complete data set is used (Figure 2.5 a), whereas for wavy periods ($u_{br} > 5$ cms^{-1}), when the greatest concentrations are observed, SSC is strongly correlated with the wave stresses ($R^2 = 0.83$) suggesting that waves are primarily responsible for resuspension and the elevated near-bottom concentrations observed at the 12m site (Figure 2.5b). When wave-current interaction was considered, no significative improvement in correlation was observed (not shown here), however, the magnitude of the total shear stress was at times much greater than stresses due to waves acting alone.

Near-surface suspended sediment concentrations are much lower than near-bottom concentrations and are less variable. When stratification is reduced during storms, peak near-surface concentrations can reach up to 50 mgl^{-1} as sediment is mixed from the bottom (Figure 2.4d). During calm periods near-surface concentrations were on the order of 10 mgl^{-1} and remarkably constant, particularly during stratified neap tide conditions. After day 280 an increase in background concentration is observed (Figure 2.4d), for both near-bottom and near-surface signals, which is attributed to the reduction in stratification and the presence of a very shallow pycnocline (Figure 2.4a). Nevertheless, near-surface concentrations were still below 25 mgl^{-1}.

Near-bottom cross-shore fluxes result in a net export of suspended sediment by the end of the observational period, but the direction and intensity of transport was variable (Figure 2.6a,b). Though
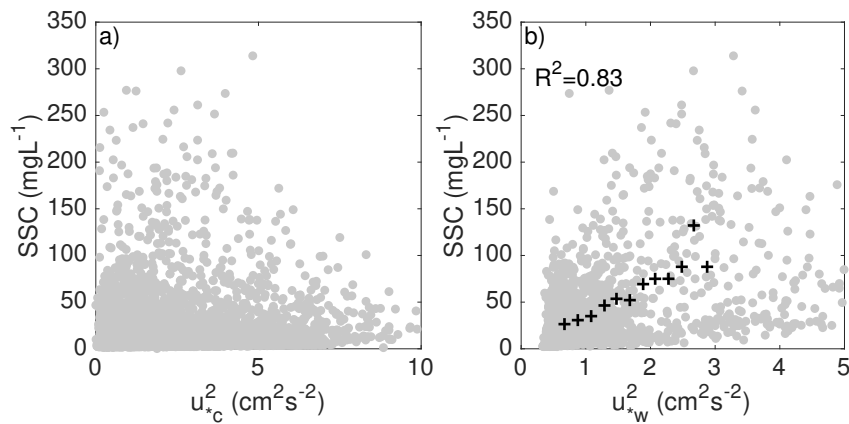
Figure 2.5: SSC versus wave and current friction velocities. (a) SSC versus current friction velocity for the complete dataset. (b) SSC versus wave friction velocity u_{*w}^2 when $u_{br} > 5$ cms^{-1}. Data every 15 min was binned on u_*^2 (black crosses). R^2 value corresponds to the binned data.

density-driven cross-shore velocities during stratified neap tides can be relevant as a consequence of tidal straining, the corresponding transport at depth is very small as a result of low sediment concentrations (Figure 2.6a, days 260-264 and 273-280).

Significant net offshore transport is observed during both storms (days 264-266 and 280-284), however, the transport direction varied within those periods. High cross-shore sediment fluxes during storms are the result of very high suspended sediment concentrations, since the absence of stratification resulted in a considerable reduction of the cross-shore currents.

Near-bottom transport during spring tides is much higher relative to the transport observed during neap tides. The direction of net (cumulative) transport during spring tide was variable; net onshore transport was observed during days 266 to 270, and offshore transport was observed during days 284-288. It is of note that the system is effectively reset by stratified spring transport after the big storm of days 264-266, as the onshore fluxes brought back an equivalent amount of sediment to what was previously exported during the storm (Figure 2.6a,b).
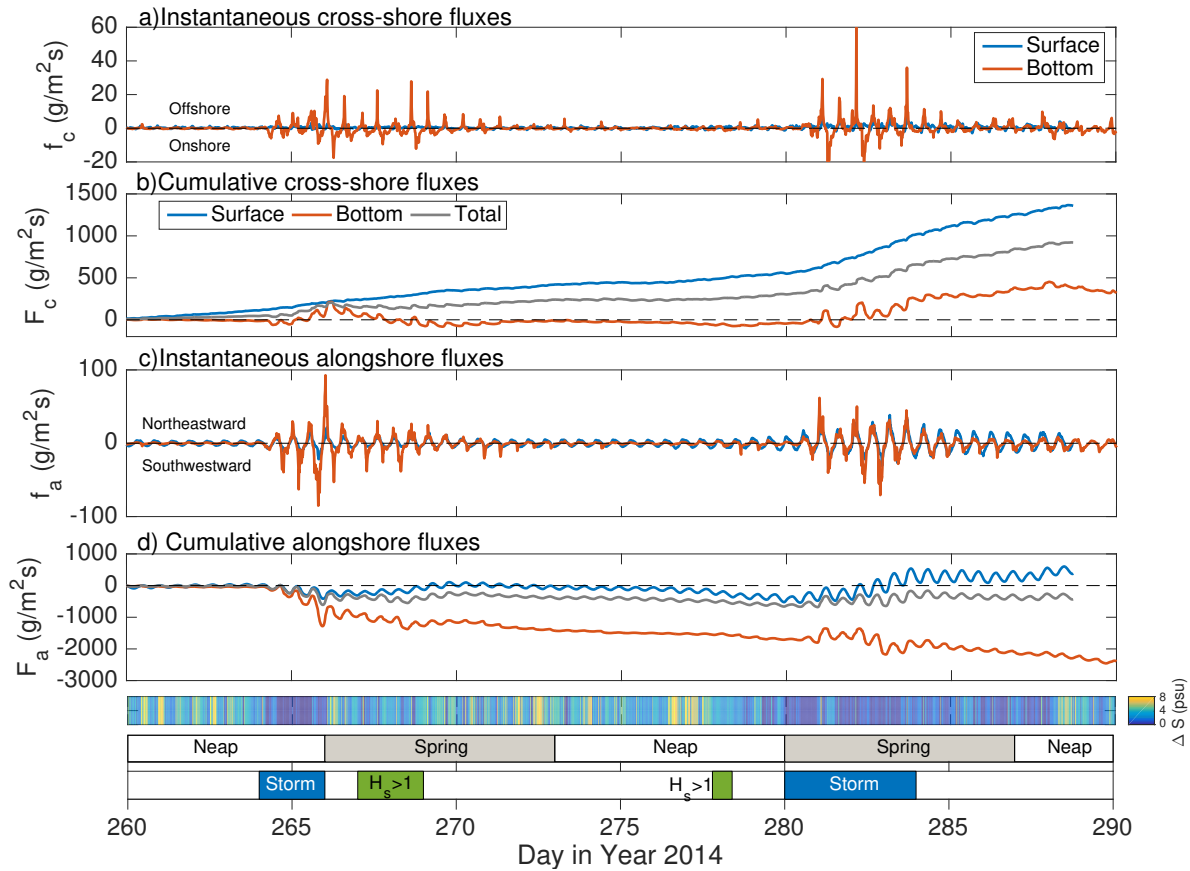
Figure 2.6: Near-bottom, near-surface and total (top to bottom) suspended sediment fluxes. (a) Instantaneous cross-shore fluxes. (b) Cumulative cross-shore fluxes. (c) Instantaneous alongshore fluxes. (d) Cumulative alongshore fluxes. In all panels the red line represents near-bottom fluxes and the blue line represents near-surface fluxes. In panels (b) and (d) the gray line represents the cumulative total (top to bottom) flux. Bottom bars show vertical stratification in terms of top-bottom salinity difference ΔS (psu), neap/spring and storm periods, and the occurrence of $H_{sig} > 1$ (m).

The cumulative near-surface cross-shore sediment transport was always directed seaward (Figure 2.6b). The intensity of near-surface transport was relatively constant, with increased transport during storms, most notably during days 280-284 as a result of increased background concentrations. The overall magnitude of near-surface transport is approximately four times greater than net transport at depth, which is attributed to persistent offshore flows near the surface as a result of the density-driven circulation.

Net near-bottom alongshore sediment transport was always directed to the southwest (Figure 2.6 d), with episodes of elevated transport during storms (Figure 2.6 c). The magnitude of transport was higher than the corresponding cross-shore transport, as alongshore velocities are much higher and do not depend on the mean state of stratification. By the end of the deployment the near-surface cumulative alongshore transport was directed towards the northeast (Figure 2.6d), however, it was much smaller than transport at depth. Tidal asymmetries seem to be responsible for the shift in direction between neap and spring tides; during neap tides, a longer ebb duration dominates over higher flood velocities and results in southward transport, and during spring tides, higher flood velocities dominate over the effect of a longer ebb duration resulting in northward transport.

Total (top to bottom) cross-shore sediment flux was directed offshore, while the total alongshore transport was directed to the southwest (Figure 2.6b,d), similar to what was reported by *Horner-Devine et al.* (2017) based on field work in winter 2013.

2.4.3 Near-bottom cross-shore transport mechanisms

In this section we focus in detail on distinct periods in the record to identify the mechanisms that generate cross-shore transport at depth, and specify the forcing conditions under which they occurred. We describe three transport mechanisms; the observed water column response and a conceptual schematic for each is presented in Figures 2.7 to 2.11.

It is worth mentioning that in this section we describe the clearest transport signals, but that other mechanisms were observed in addition to the ones presented here. In particular, we observed

periodic peaks in near-bottom suspended sediment concentrations occurring approximately 30-60 min after flow reversal that are not timed with high flow velocity or high bed stresses. These peaks appear to be the result of an eddy that forms on the flood phase of the tide on the lee side of the Sand Engine (*Radermacher et al.*, 2016) and advects sediment offshore as the tidal velocities reverse. The formation of the eddy is similar to that reported by *Geyer and Signell* (1990) for tidal currents around a headland. This signal was clearest during calm neap tides (days 260 to 264), as background concentrations were low, but resulted in negligible transport when compared to the mechanisms described in the following subsections (Figure 2.6b).

Storm transport

Our measurements included two significant storms that are typical of the fall season along the Dutch coast and have a large impact on coastal suspended sediment concentrations (Figure 2.4d). Sediment transport during storm events results from the combination of high near-bottom sediment concentrations, primarily as a result of wave-induced resuspension, and weak cross-shore currents. Sediment availability dominates over the fact that cross-shore currents are very small, yielding high sediment fluxes with transport preferentially directed offshore.

The local response of salinity, velocity, bed stresses and suspended sediment concentrations during the first storm period (days 264-266) is examined in detail in Figure 2.7. Stratification is nearly zero during the storm as high winds and waves mix out the water column (Figure 2.7a). Under well-mixed conditions, tidal currents are primarily rectilinear and coast parallel according to the progressive Kelvin wave character of the semidiurnal tide along the Dutch coast (*Simpson*, 1997). However, as shown by *De Boer et al.* (2006), small ellipticities are still present due to Earth's rotation and the proximity of the coastal wall. As a result, very weak cross-shore currents still occur, particularly near the bottom, with maxima below 0.1 ms^{-1}. Tidal current asymmetry (with higher flood velocities) and the absence of tidal straining and results in higher offshore velocities occurring during the flood phase of the tide.

During this unstratified period the cross-shore velocities are reduced compared to the previous
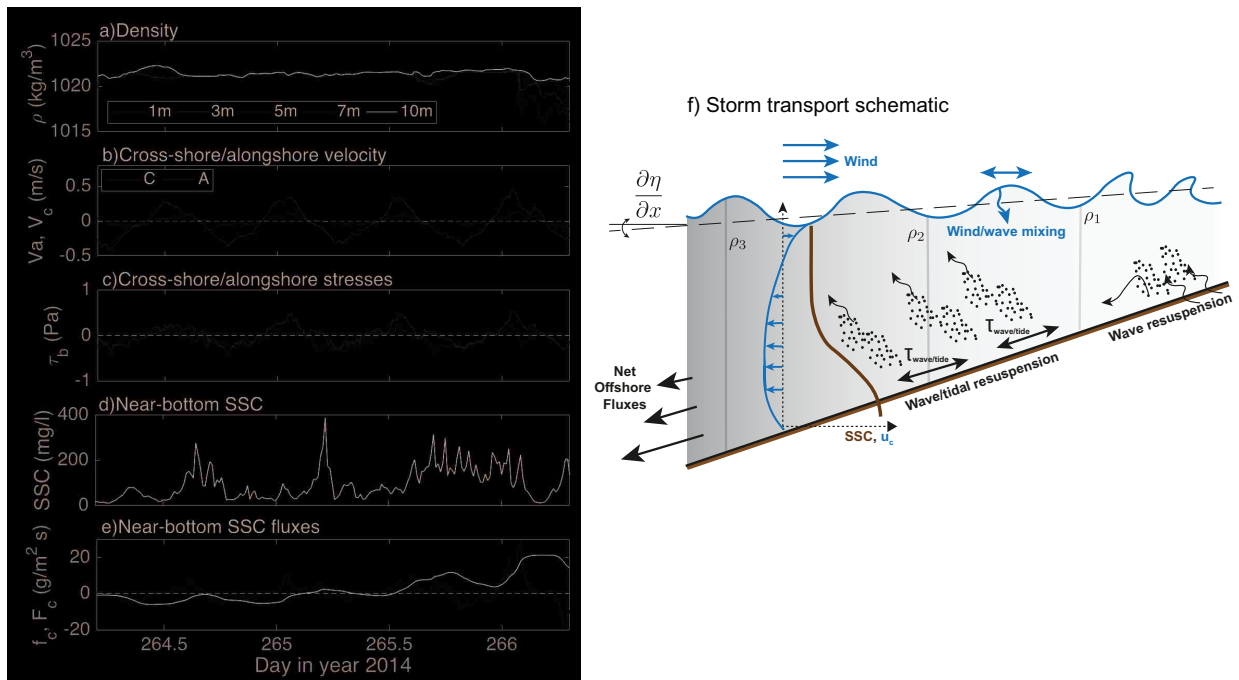
Figure 2.7: Storm Transport. (a) Salinity, 12m mooring. (b) Near-bottom cross-shore (blue line) and alongshore (red line) velocities. (c) Bottom cross-shore (blue line) and alongshore (red line) stresses. (d) Near-bottom suspended sediment concentration. (e) Instantaneous (blue line) and cumulative (black line) near-bottom SSC fluxes. Cumulative sediment flux has been scaled for plotting purposes. (f) Schematic of transport process.

stratified neap tide period, are almost in phase with the alongshore velocities, revealing the absence of tidal straining (Figure 2.7b). Peaks in suspended sediment concentration are not aligned with the peaks in tidal velocity or stress, suggesting that tidal motions are not sufficient on their own to generate the observed resuspension (Figure 2.7 b, c and d). We conclude that resuspension is primarily wave-induced. Offshore (positive) cross-shore velocities are larger than the onshore velocities (Figure 2.7 b), even though onshore (negative) velocities persist longer. Because suspended sediment concentrations remain elevated during this period the asymmetry in the velocity magnitude contributes to the net offshore transport during this 2 day period (Figure 2.6e, Figure 2.7e).

In addition to tidal currents, cross-shelf winds contribute to cross-shelf exchange during storms. Strong onshore winds occurred during the first storm (days 264-266), with wave heights on the order of 2m. During this period, cross-shore currents are offshore through the entire water column, except for a thin surface layer ($\sim 1-2$ m) flowing onshore. We hypothesize that this current structure is the result of a cross-shore barotropic pressure gradient associated with wind-induced coastal setup. We estimate the cross-shore sea surface slope using the residuals from a harmonic analysis fit performed to the ADCP depth measurements at our 18m and 12m locations, which are separated by 3.5 km (Figure 2.8a,b). Sea surface slope is strongly correlated with observed variations in near-bottom low-passed cross-shore and alongshore velocities (Figure 2.8b,c). A residual offshore flow is observed during days 264-266, with a 16-hour delay between maximum setup and maximum cross-shore residual velocity. Onshore propagating waves can also contribute to the mean offshore flow at depth in response to the onshore Stokes drift at the surface (*Lentz et al.*, 2008; *Fewings et al.*, 2008).

Gutierrez et al. (2006) suggest that the relative strength of the wind and pressure gradient terms in the momentum equation influences the structure of the flow in the inner shelf; flow opposes the wind when the pressure gradient term exceeds the wind stress term. Comparison of the wind stress and setup terms in the depth-averaged cross-shore momentum balance for our data shows that the pressure gradient is in fact large enough during the first storm to drive flow against the wind through most of the water column (Figure 2.8d). The difference between these two momentum terms is expected to be due to the contributions from bottom stress and wave radiation stresses, both of which are expected to be high during storms, and Earth's rotation.
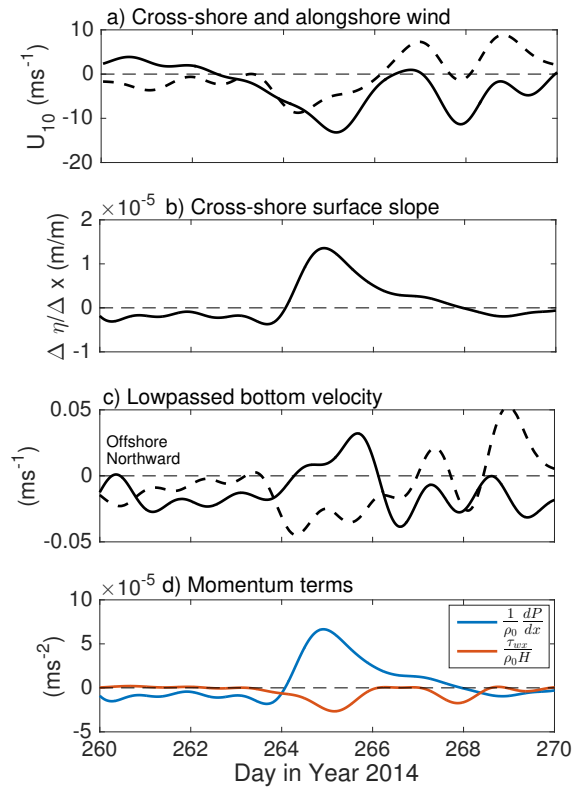
Figure 2.8: Wind forcing during storm 1. (a) Cross-shore wind (solid line) and Alongshore wind (dashed line). Positive cross-shore wind is directed offshore and positive alongshore wins is directed northwards. (b) Lowpassed cross-shore sea surface slope, computed from ADCP depth measurements at 18m and 12m. (c) Lowpassed near-bottom cross-shore (solid line) and lowpassed near-bottom alongshore velocity (dashed line). Positive cross-shore velocity is directed offshore and positive alongshore velocity is directed northwards. (d) Wind (red line) and pressure gradient (blue line) terms from the depth-averaged cross-shore momentum balance.

Offshore winds during the second storm (days 280-284) also generate a persistent offshore flow through most of the water column. The situation is different from the previous storm, however, in that the flow follows the wind direction. Low-passed near-bottom cross-shore velocities are directed offshore (not shown) and their magnitude is on average larger than those observed during the first storm, probably due to the alignment of the wind and wave forcing (*Fewings et al.*, 2008). It is also important to note that the second storm occurs during spring tide so offshore directed tidal currents are larger. No data is available to compute the pressure gradient during the second storm since the ADCP at our 18m mooring stopped working around day 279.

Frontal transport

The passage of distinct freshwater lenses at the surface, and the fronts that bound them, is an important dynamical component of the mid-field region. Implications for sediment transport have been previously reported by *Horner-Devine et al.* (2017) and were described in Section 2. Figure 2.9 illustrates the frontal pumping mechanism for a single tidal cycle, where the observed lag (~ 0.5 hr) between the drop in salinity at the plume front and peak suspended sediment concentrations (Figure 2.9a,d) is interpreted as the plume pumping wave-suspended sediment from the inshore. Bed stresses (Figure 2.9c) are low when the plume passes over our instruments, confirming that the suspended sediment peak is not due to local re-suspension and is instead the result of advection from inshore. Our observations show that cross-shore transport driven by frontal dynamics is significant only during spring tides with low to moderate wind forcing (wind speeds lower than ~ 10 ms^{-1}), such that the freshwater lens is not driven offshore or rapidly mixed with ambient ocean waters.

In addition to the frontal pumping mechanism, our turbulence measurements show that near-bottom turbulence spikes during frontal passages. In particular, the cross-shore component of the Reynolds stresses ($\overline{u'w'}$) exhibits peaks right when the freshwater plume passes over the instruments. This effect can be seen in 2.10c, which is intended to describe transport processes during a stratified spring tide period (see Section 4.3.3) but shows significant frontal activity. Peaks in $\overline{u'w'}$ are often
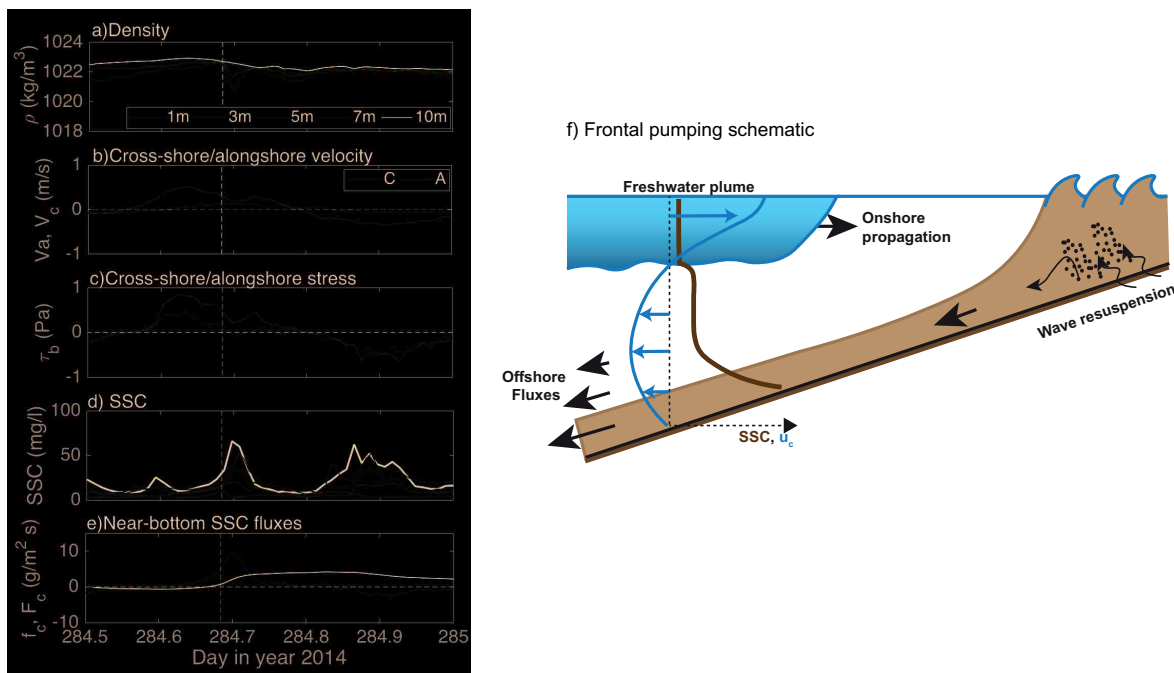
Figure 2.9: Frontal Pumping. (a) Density. (b) Cross-shore (blue line) and alongshore (red line) near-bottom velocities (c) Cross-shore (blue line) and alongshore (red line) bottom stress. (d) Suspended sediment concentration. Black line represents near-bottom concentration, blue line represents 3m above bottom, green line is 5 mab, red lines is 7mab and gray line is surface concentration. (e) Instantaneous (blue line) and cumulative (black line) near-bottom cross-shore fluxes. Vertical dashed line represents the arrival time of the front. (f) Schematic of transport mechanism.

timed with peaks in near-bottom sediment concentration suggesting local resuspension of sediment and subsequent offshore advection due to the passing of the tidal plume front (Figure 2.10c,d). It is worth noting that the increase in bottom turbulence is only observed during the passage of thick fronts with cross-shore propagation speed on the order of 0.4-0.5 ms^{-1}. This processes likely becomes even more important as the front propagates to shallower depths, as stresses could be further increased resulting in enhanced re-suspension.

The net effect of frontal processes therefore is to generate offshore sediment transport (Figure 2.9d), by means of high offshore flux pulses that can be readily identified in the near-bottom sediment

fluxes (Figure 2.6a, days 266-270).

Stratified tidal transport

Stratification is expected to strongly influence transport processes in ROFIs. Here we define stratified tidal transport as those transport processes occurring during stratified periods at timescales longer than the passage of the tidal plume front. During stratified periods, observed near-bottom cross-shore currents are predominantly directed onshore resulting in net onshore sediment transport.

High cross-shore transport at depth is observed during spring tide days 267-270 with moderate downwelling wind forcing. A distinct two-layer density structure is observed with cross-shore flow driven by large horizontal density gradients resulting in the onshore movement of denser water close to the bottom (see Section 4.1). Surface and bottom mixing due to winds, waves and spring tides contribute to mixing the upper and lower layers, resulting in a 3-4 m thick surface layer and a 7-8 m thick bottom layer of uniform density that breaks down only when the plume front passes through our field site (Figure 2.10a). The effect of the tidal plume front can be clearly observed in the near-bottom cross-shore velocity and sediment fluxes (Figure 2.10 b,d) as described in section 4.2. No apparent tidal variability is observed in the suspended sediment concentrations (Figure 2.10d), suggesting that waves and advection are responsible for concentrations exceeding 100 mgL^{-1}. The density-driven circulation profile results in onshore velocities and sediment transport in the lower layer that persist for most of the tidal cycle (Figure 2.10b and e). Despite the fact that the magnitude of onshore transport is typically much less than the transport peaks resulting from frontal dynamics, the cumulative transport is dominated by persistent onshore fluxes resulting from the density-driven flow (Figure 2.10e).

Cross-shore tidal straining dynamics appear to gain importance during the more vertically stratified neap tides, as has been previously reported for the far-field (*De Boer et al.*, 2006; *Simpson and Souza*, 1995) when cross-shore horizontal density gradients are not particularly high. For these periods, the tidal ellipses are more circular than during storm or spring tide periods (anticyclonic near the surface and cyclonic near the bottom) with current patterns that are not symmetrical as
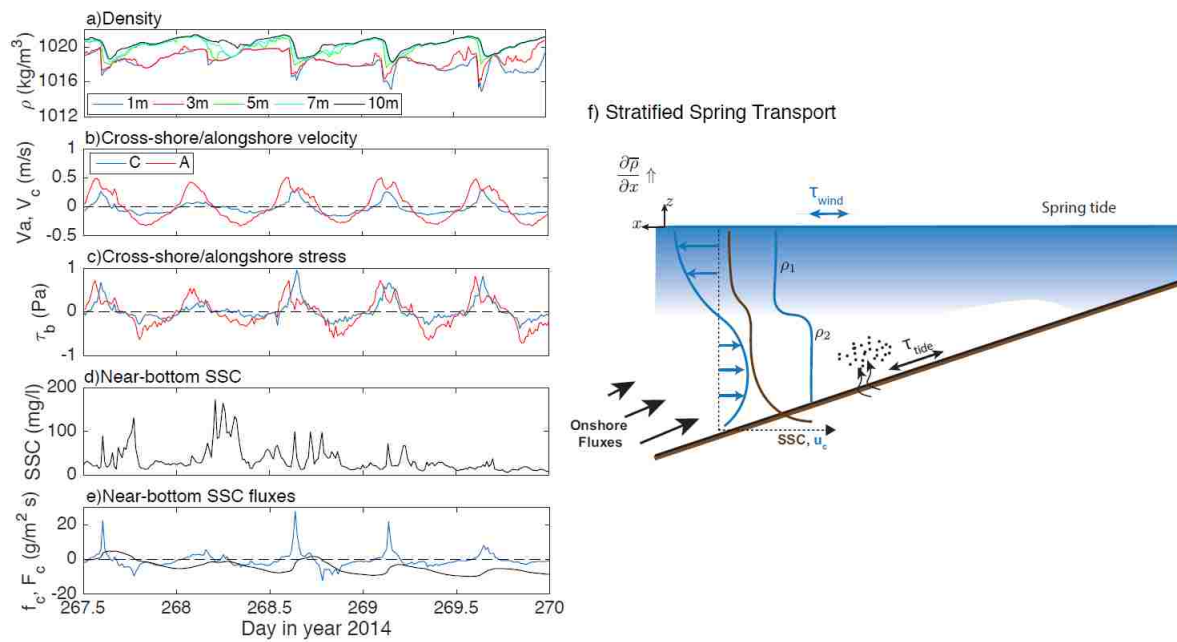
Figure 2.10: Stratified Spring Transport. (a) Salinity, 12m mooring. (b) Cross-shore and alongshore velocity. (c) Cross-shore and alongshore bottom stresses. (d) Near-bottom SSC. (e) Near-bottom suspended sediment fluxes, instantaneous (blue) and cumulative (black, scaled). (f) Schematic of transport process during stratified spring tide after frontal passage.

in the far-field region, and we observe that the timing of offshore/onshore directed currents also differs. Figure 2.11 examines in detail the local response under stratified neap tide conditions. Cross-shore and alongshore currents are out of phase due to effect of vertical stratification and cross-shore current asymmetry, favoring onshore velocities near the bottom (Figure 2.11b), results in net onshore sediment fluxes (Figure 2.11d). However, the magnitude of transport is negligible when compared to transport during spring tide due to low sediment concentrations (Figure 2.11d) resulting from low wave forcing and low tidal stresses.
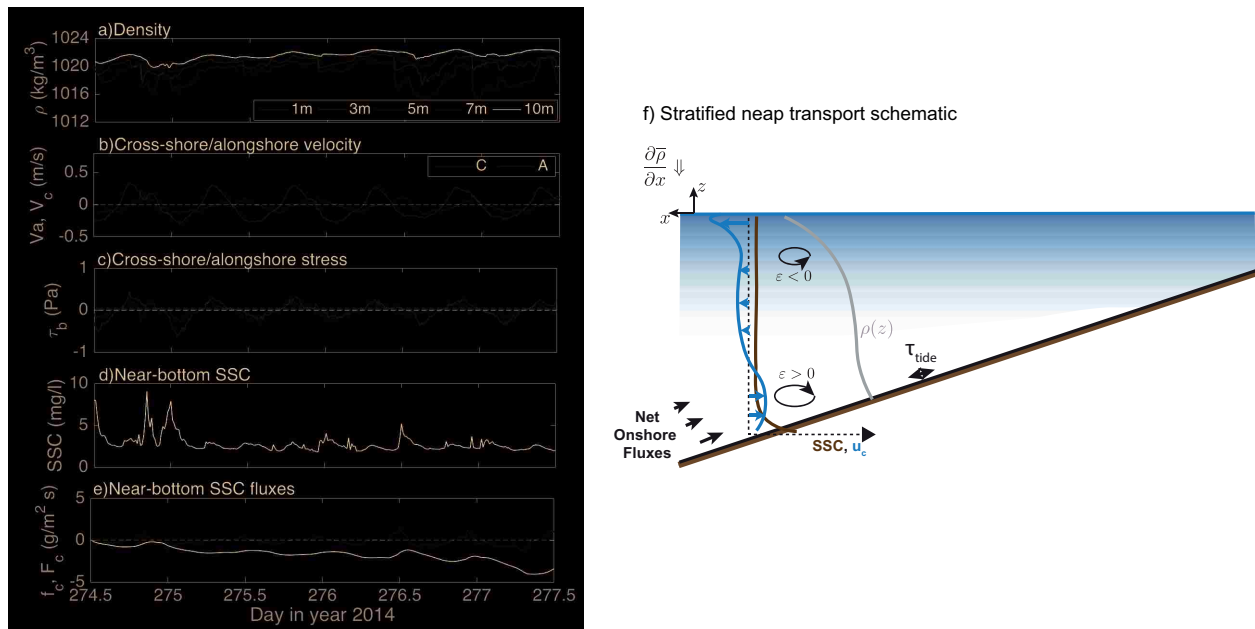
Figure 2.11: Stratified neap transport. (a) Density at 12m mooring. (b)Near-bottom cross-shore velocity. (c) Near-bottom suspended sediment concentration.(d) Near-bottom cross-shore suspended sediment fluxes. Blue line represents the instantaneous flux and black line represent the cumulative sediment flux. (e) Schematic of transport mechanism. ε represents ellipticity (see Section 5.3 for definition).

2.5 Discussion

2.5.1 Net transport and the role of individual transport mechanisms

In this section we examine the net cross-shore transport, considering in particular the relative contributions of each of the transport mechanisms described in Section 4. The direction of cross-shore transport switches and its magnitude changes several times during the observational period (Figure 2.12b) as the dominant transport mechanisms turn on and off in response to the tidal, wind and wave forcing. Storm transport is dominant when wind and wave conditions are sufficient to homogenize the water column and preferentially transports near-bottom sediment offshore during our study period. Frontal transport is active under moderate to low wind conditions and during

spring tides, and preferentially transports near-bottom sediment offshore. Stratified spring and neap tide transport preferentially transports near-bottom sediment onshore, although the magnitude of cross-shore transport during neap tides is very low.

Net transport results from the combination of these different modes, which contribute to onshore or offshore fluxes at different rates. Net transport by the end of our deployment was offshore, however, significant episodes of landward transport were observed (Figure 2.12b) as the forcing conditions changed in time. Figure 2.12c provides a basis for comparing the relative strength of each process in terms of the observed transport rates and the total transport during each period. The highest transport rates are observed during storms, with the first storm being particularly intense and contributing almost as much net transport as the second storm in approximately half of the time. Net transport and transport rates during both spring tide periods were also significant. The stratified spring period following the first storm transports more sediment landward than is transported seaward by the preceding storm. Transport is also significant during the second spring tide; however, it is directed offshore due to reduced stratification at our site as the whole plume was displaced towards the north and the influence of the fronts. In all, the net transport during the two storm periods accounts for 45% of the total transport over the observational period; transport during the stratified spring tide and transport during the frontal periods account for 25% and 15% of the total, respectively.

It is important to note that the observed transport mechanisms often occur at the same time, reinforcing or competing with each other, or may influence subsequent periods by modifying ambient conditions. For example, both spring tide periods in our study are influenced by preceding storm conditions, which may impact transport processes after their occurrence. The episode of elevated landward transport due to stratified spring tide transport occurring after the first storm is likely influenced by the storm itself, as sediment may remain in suspension or be easily re-suspended during the days that follow. Also, plume fronts often propagate on a vertically and horizontally stratified ROFI , and the magnitude and direction of transport results from the interaction of these processes. A clear example of this is observed during the stratified spring transport period that follows the first storm (days 266 - 270; Figure 2.10). During this period, strong plume fronts compete

with cross-shore currents resulting from large horizontal density gradients, such that the seaward transport resulting from frontal processes is countered by onshore tidal transport. Although frontal processes generate very large pulses of seaward transport, landward transport is more persistent and ultimately results in a net landward transport during this period. Interestingly, the direction of transport switches to offshore toward the end of this spring tide period. Detailed examination of the data suggest that the transport during this latter period is more pulsed, suggesting that fronts may play an increasingly important role.

As noted in Section 4.3, additional transport due to the formation and advection of a headland eddy as a consequence of the interaction of the tidal currents and the Sand Engine is evident on our measurements, but yielded no significant contribution to the overall cumulative near-bottom transport (see days 260-264 in Figure 2.12b).

2.5.2   Relevance of frontal pumping

Frontal pumping was found to be the dominant mechanism of cross-shore transport of fines at depth in a field experiment conducted in the same location in winter 2013 during a period when wind and wave forcing was moderate (*Horner-Devine et al.*, 2017). One objective of this study is to investigate whether plume pumping is the dominant transport mechanism under a different set of forcing conditions.

We observe that most of the cross-shore transport at depth occurs during days 264-270 and days 280-287 (Figure 2.6a,b). The first period is strongly influenced by the energetic storm of days 264-266, however, the signature of frontal processes is clear during days 267-270 (spring tide) where significant pulses in offshore transport are observed. As described in Section 5.1, cumulative transport during days 267-270 is directed onshore, despite the seaward transport pulses. During days 280-287 (spring tide) net near-bottom transport is offshore, and again it is strongly influenced by the storm-induced sediment concentrations of days 280-284. However, the situation is different from the previous spring tide in that net transport after day 284 continues to be in the offshore direction. After the storm, the rate of transport decreases but it is still dominated by offshore pulses (Figure

2.6a)), and a detailed inspection of this period (Figure 2.9) reveals the continuous occurrence of frontal pumping, though not as strong as observed during days 267-270.

From our observations, we conclude the following: frontal pumping is significant during spring tides and contributes to seaward sediment transport. It produces cross-shore fluxes comparable in magnitude to those observed during storms. However, when considering a frontal period, such as days 267-270, frontal transport will sometimes compete with other transport mechanisms and will not necessarily dominate the transport signal. In particular, we observe that frontal pumping dominates when the ambient stratification is low, as observed in 2013 (*Horner-Devine et al.*, 2017) and in the second spring period (days 284 - 287), but that its impact is diminished in the presence of higher persistent stratification.

2.5.3 Role of stratification

The role of stratification on the direction of net transport can be better understood in terms of a mean state of vertical stratification, at timescales equal or longer than the tidal period. Figure 2.12a shows the time series of top-bottom salinity difference (1m and 10m below the surface) at the 12m site and depth-averaged horizontal salinity difference between the 18m and 12m sites. The data were low-pass filtered to remove variability at tidal and shorter time scales, thus removing the influence of the plume fronts. The relation between cross-shore transport and the mean state of stratification can be observed in Figure 2.12a,b; stratification leads to onshore transport at depth whereas mixed periods lead to seaward transport. It is important to note the role of high winds in destroying stratification and also influencing current structure. The water column tends to be strongly stratified for over half of the deployment ($\Delta S \sim 4 - 5$ psu); however, negligible sediment concentrations during neap tides result in only one stratified period with significative transport.

One effect of stratification and the straining of the density field is the generation of residual currents (*Stacey et al.*, 2001; *Burchard and Hetland*, 2010), which also contributes to the trends observed in Figure 2.12. The decomposition of the observed velocities into tidal and residual components (Figure 2.12b) reveals that bottom sediment fluxes are in large part dominated by the residual trans-
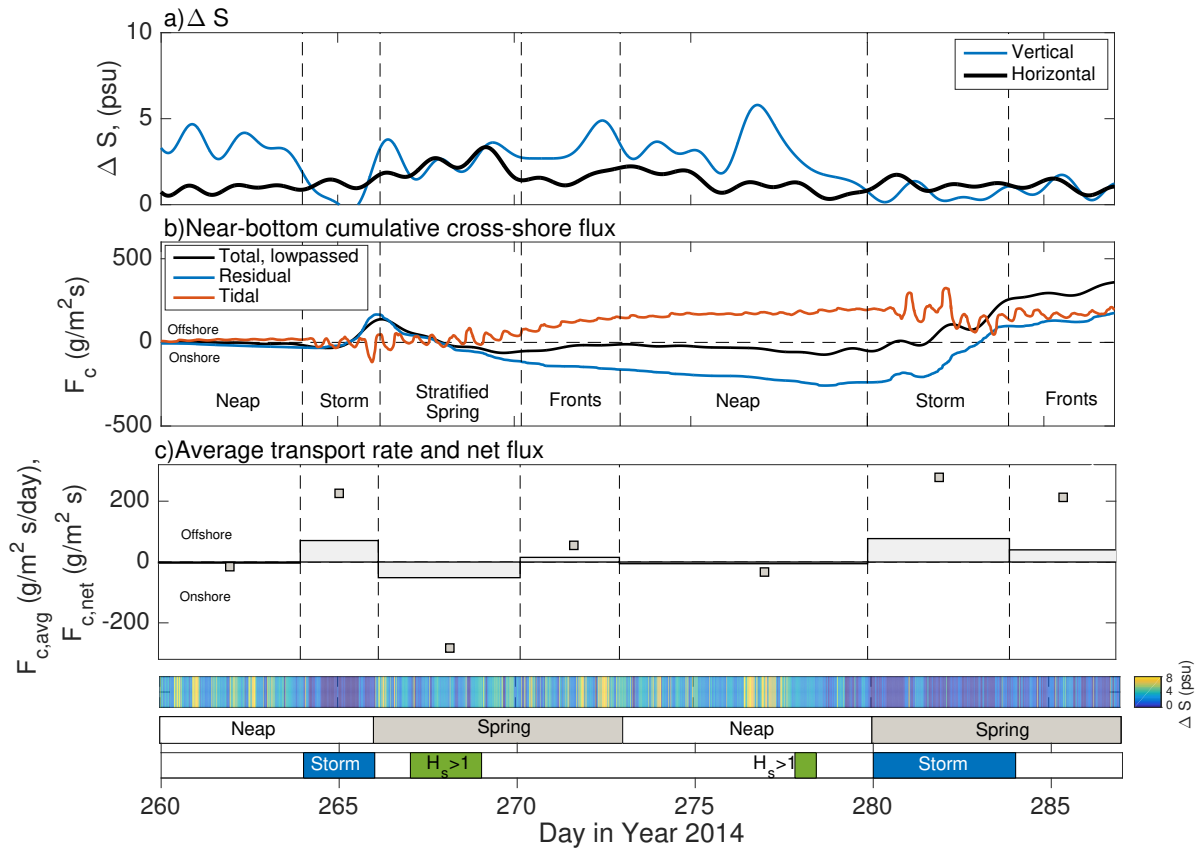
Figure 2.12: Drivers of cumulative cross-shore flux (a) Top-bottom salinity difference (blue line) and mean horizontal salinity difference between 18m mooring and 12m mooring (black) (b) Near-bottom cumulative cross-shore flux (black line), Near-bottom cumulative tidal flux (red line) and near-bottom cumulative residual flux (blue line) (c) Average transport rate (bars) and net transport (squares) in each period. Bottom bars show vertical stratification in terms of top-bottom salinity difference ΔS (psu), neap/spring and storm periods, and the occurrence of $H_{sig} > 1$ (m).

port. In this region, tidal straining processes are asymmetric and tend to favor onshore currents near the bottom. The density-driven circulation also induces onshore currents in the near-bottom layer. When these processes occur, that is, when stratification is present, residual velocities and associated transport are directed landward. On the other hand, when stratification is significantly reduced (or completely eliminated), the velocity field characteristic of tidal straining circulation breaks down, cross-shore shear decreases and the velocity is vertically unidirectional. Under conditions of strong meteorological forcing, the tidal asymmetry with higher flood velocities and an offshore mean flow created by coastal setup and waves led to seaward net transport over the tidal cycle.

Tidal straining is the dominant process influencing the dynamics of bottom-attached plume systems such as the Rhine ROFI, and it is clear that the tidal straining velocities far from the river mouth influence the movement of sediment (*Joordens et al.*, 2001; *van der Hout et al.*, 2015). In the following we consider the importance of tidal straining on sediment transport in this mid-field plume region. Ellipticity, defined as the ratio of minor to major axis of the tidal ellipses (negative for anticyclonic rotation), has been considered as a metric of tidal straining (*De Boer et al.*, 2008) as it quantifies the deviation from the rectilinear current pattern typical of a progressive Kelvin wave ROFI regime (with zero ellipticity) as a result of vertical stratification. Periods of strong vertical stratification show high counter-rotating ellipticity in the upper and lower layers and very high top-bottom ellipticity difference, whereas the opposite is true for well-mixed periods. Figure 2.13 shows the relation between the mean state of stratification and net sediment fluxes in terms top-bottom ellipticity difference and top-bottom salinity difference. Wind speed has been included as an indicator of meteorological stirring and the occurrence of storms. Calculation of ellipticity requires the use of a moving window tidal harmonic analysis, and each data point corresponds to a 25 hour period. The highest sediment fluxes are observed at very low ellipticity and salinity differences values ($\Delta\varepsilon < 0.1$ and $\Delta S < 1$ psu) and high wind speeds, suggesting that barotropic processes dominate near-bottom cross-shore transport during this period. Intermediate ellipticities and salinity differences (see $1 < \Delta S < 3$) during spring tides with moderate to low wind forcing also result in significant cross-shore transport, suggesting that baroclinic processes are also important to cross-shore transport. However, sediment fluxes are severely reduced for values of
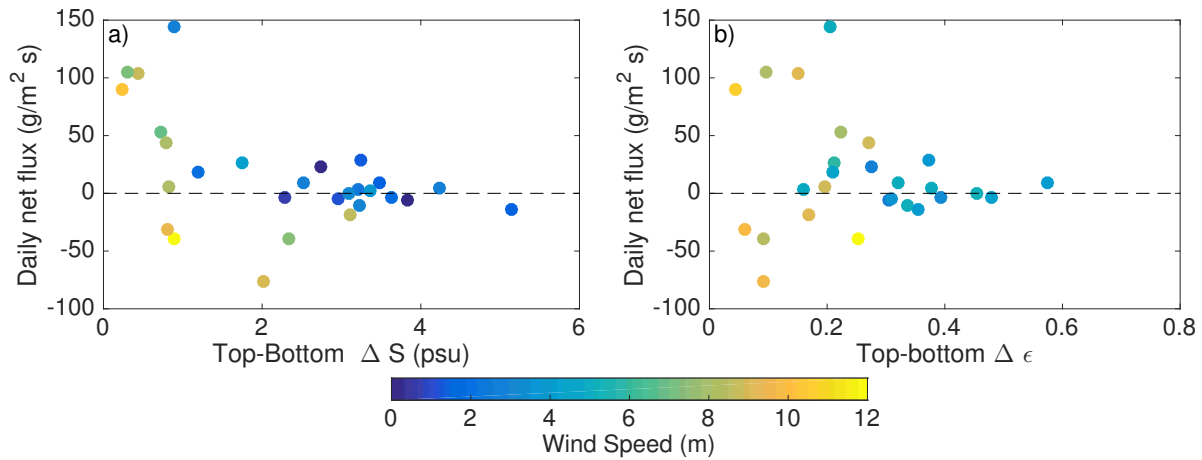
Figure 2.13: Stratification and bottom sediment fluxes. (a)Top-bottom salinity difference (averaged over a day) versus daily net flux. (b) Top-bottom ellipticity difference versus daily net flux. Colors indicate mean wind speed (averaged over a day).

$\Delta\varepsilon >= 0.3$, corresponding primarily to stratified neap tide periods under weak wind forcing, and $\Delta S >= 3$ (psu). This suggests that tidal straining on its own does not contribute significantly to the net cross-shore sediment flux in the mid-field plume region during this period. The reason for this is that strong vertical stratification and tidal straining occur during low energy periods, when sediment concentrations are low. Indeed, analysis of the neap tide data (not shown) confirm that there is a residual onshore velocity that is sufficient to generate onshore sediment flux of a similar magnitude to the spring tide and storm fluxes, if the near-bed sediment concentration were similar to that observed under more energetic conditions.

It is interesting to note that near-bottom cross-shore transport was very low during unstratified conditions in 2013 and significant transport was only observed during periods of strong frontal activity, which accounted for more than 85% of the total transport during that measurement period (*Horner-Devine et al.*, 2017). Sampling in winter 2013 followed a period of very stormy conditions and we hypothesize that the difference in behavior is a result of lower sediment availability on the bed in 2013 because of these preceding storms. This hypothesis is supported by the observations

that average near-bottom sediment concentrations in the winter 2013 sampling period were less than half those observed in fall 2014. It is likely that sediment accumulates on the seabed during the calmer summer months, resulting in higher concentration of suspended sediment during the first storms in the fall.

2.6   Conclusions

We used detailed measurements of density, suspended sediment concentration and current structure to investigate transport processes in the mid-field region of the Rhine River plume. This work establishes how tidal, wind and wave forcing in a region strongly influenced by river-generated density stratification result in along- and across-shore sediment transport. Furthermore, we identify the dominant mechanisms driving the cross-shore transport of fine sediments at depth. The work has particular significance because the measurements were made in the vicinity of the Sand Engine, a mega-nourishment project that could potentially change coastal protection practices. The primary conclusions of the work are as follows:

- During the four week study period in fall 2014, cumulative suspended sediment fluxes near the surface were offshore and upcoast (northeast). Cumulative fluxes near the bed were offshore and down coast (southwest). Cumulative top to bottom fluxes were offshore and down coast.

- Three mechanisms of cross-shore transport at depth were observed. Net transport results from the combination of these mechanisms as they turn on and off in response to the forcing conditions, and the relative importance of each mechanism explains the variability observed in both magnitude and direction of transport.

- Storms contribute most to the cross-shore sediment transport during the observation period. During those periods the water column is vertically well-mixed and high waves play a dominant role in sediment resuspension. Barotropic transport during storms accounts for almost half of the observed transport at depth and results in net offshore transport. The occurrence of cross-shelf winds generated a coastal setup that contributed substantially to the offshore flux of fine sediment.

- During stratified periods, transport at depth depends on wind magnitude and direction, which set the location of the freshwater plume, determine the strength of the cross-shore density gradients and the strength of the fronts. Tidal straining on its own does not appear to generate significant sediment transport as it is strongest during neap tides when vertical stratification is higher and sediment concentrations are very low. Net transport during stratified periods is onshore.

- Tidal plume fronts are clearly observed in density and cross-shore velocity profiles, presenting a dynamical component not observed in the far-field. Their contribution to sediment transport is only significant during spring tides, when they manifest as strong pulses of seaward transport at depth that can be of similar magnitude to storm fluxes. However, the overall effect of fronts on net transport depends on the mean state of stratification; net seaward transport due to fronts is only realized when the ambient coastal stratification, which generates onshore transport, is low.

- Over the course of the measurement period, near-bottom suspended sediment flux is offshore during unstratified periods, primarily due to storms and to a lesser degree fronts, and onshore during persistently stratified periods, primarily during spring tide. Net cross-shore transport was offshore during our observation period; however, the magnitude of the onshore and offshore transport mechanisms were close enough that a different combination or sequence of forcing conditions could conceivably result in net shoreward transport instead.

Overall, we conclude that both barotropic and baroclinic dynamics are relevant for sediment transport processes in the mid-field region of the Rhine ROFI. On longer time scales, we expect seaward transport to dominate during winter time as the water column would tend to be mixed more frequently. On the contrary, calm weather during summer time would lead to shoreward transport because increased stratification could be expected.

Chapter 3

WAVE GENERATION OF GRAVITY-DRIVEN SEDIMENT FLOWS ON A PREDOMINANTLY SANDY SEABED

3.1 Introduction

Sediment gravity flows move large amounts of sediments from deposition zones in shallow coastal areas to deeper ocean regions, contributing substantially to the morphological evolution of continental shelves (*Wright et al.*, 2001; *Wright and Friedrichs*, 2006; *Walsh et al.*, 2004; *Parsons et al.*, 2007) and the export of sediment, with associated nutrients, contaminants and carbon, to the abyssal ocean (*Puig et al.*, 2003, 2004). Over the last two decades, several field and modeling studies have demonstrated the importance of wave-supported gravity flows (WSGF) to the cross-shelf transport of muds on continental shelves and have provided a description of the governing mechanisms (*Ogston et al.*, 2000; *Traykovski et al.*, 2000; *Scully et al.*, 2002, 2003; *Wright and Friedrichs*, 2006; *Parsons et al.*, 2007; *Macquaker et al.*, 2010). In WSGF, turbulence and shear stress derived from wave energy resuspends bed sediment and generates a thin near-bed high concentration layer that moves downslope due to gravity. Cross-shelf gradients in near-bottom wave energy result in large amounts of deposition in regions where waves can no longer maintain sediment in suspension (*Wright et al.*, 2001; *Scully et al.*, 2002; *Traykovski et al.*, 2007).

The dynamics of WSGF are thought to be governed by a force balance between the downslope gravitational component resulting from the sediment-induced buoyancy anomaly, and friction arising from flow over the stationary seabed (*Wright et al.*, 2001; *Scully et al.*, 2002; *Wright and Friedrichs*, 2006). In its simplest form, this force balance has been written as a linearized Chezy equation (*Wright et al.*, 1988, 2001; *Traykovski et al.*, 2007)

$$Hg' \sin \alpha = C_D u_g \left| u_{max} \right| \tag{3.1}$$

where the left-hand and right-hand sides represent the buoyancy and friction terms, respectively.

In Equation 3.1, H is the thickness of the high-concentration layer (~ 10 cm), g' is the reduced gravity, $\sin \alpha$ is the seabed slope, C_D is the drag coefficient, u_g is the gravitational flow velocity and u_{max} corresponds to the maximum velocity at the top of the high concentration layer, accounting for wave velocities and water column velocities, $u_{max} = \sqrt{u_w^2 + u_g^2 + u_c^2}$ (*Wright et al.*, 2001). The downslope transport, which depends on the suspended sediment concentration and the gravitational velocity, can be estimated from Equation 3.1 if the sediment concentration can be related to the wave forcing. This relationship is often expressed in terms of a bulk Richardson number (*Trowbridge and Kineke*, 1994; *Wright et al.*, 2001; *Wright and Friedrichs*, 2006),

$$Ri_b = \frac{B}{u_{max}^2} \tag{3.2}$$

where $B = \dfrac{gs}{\rho_s} \displaystyle\int_0^H C(z)dz = g'H$ is the buoyancy anomaly integrated over the high-concentration layer of thickness H, $C(z)$ is suspended sediment concentration (kg/m^3), s is the submerged weight of the sediment relative to seawater and ρ_s is the density of the sediment. In general, both u_g and B are unknown and model closure can be achieved by assuming that the feedback between turbulence and suspended sediments maintains Ri_b at a critical value of $Ri_c = 0.25$ (*Trowbridge and Kineke*, 1994; *Scully et al.*, 2002, 2003; *Friedrichs and Wright*, 2004); if $Ri_b > 0.25$ the damping of turbulence by stratification will cause sediment to settle, reducing Ri_b towards Ri_c, whereas if $Ri_b < 0.25$ the enhanced turbulence will resuspend more sediment causing Ri_b to increase back to Ri_c. Many recent models are based on Equation 3.1 and use a critical $Ri_b = Ri_c$ for model closure (*Scully et al.*, 2002, 2003; *Friedrichs and Wright*, 2004), assuming an unlimited supply of fine sediment that allows the turbid boundary layer to remain critically stratified at all times.

An alternative approach to modeling WSGF is to solve a mass balance within the high concentration near-bed layer, with gravitational velocities obtained from Equation 3.1 and the entrainment of sediment into overlaying waters based on stratified mixing formulations (*Traykovski et al.*, 2007; *Harris et al.*, 2004, 2005; *Chen et al.*, 2013). Sediment concentrations are related to the wave and current forcing in terms of bottom stresses and turbulence without invoking a critical Richardson number (*Traykovski et al.*, 2007; *Harris et al.*, 2004). While these models rely on parametrizations for a suite of near-bed processes such as settling speed, deposition and erosion from the seabed,

their applicability is not restricted to environments with an unlimited supply of fine sediment.

Although depositional patterns due to WSGFs have been successfully reproduced in several locations around the world using both type of models (*Scully et al.*, 2002, 2003; *Harris et al.*, 2004, 2005; *Traykovski et al.*, 2007), neither the force balance, the critical Richardson number assumption or the range of applicability of WSGF models have been rigorously tested in the field. Moreover, current observations suggest that WSGF are very limited in terms of locations and conditions. It is widely acknowledged, however, that the body of literature documenting these flows is still small and a complete understanding of the conditions required to generate them has not been achieved (*Wright and Friedrichs*, 2006), with the possibility that they are actually much more prevalent than expected.

In order to support downslope transport, sediment particles must generate a layer of very high concentration that influences the bulk density of the sediment-water suspension. It is generally assumed that this can only be achieved in fluid muds, in which hindered settling is significant, the particle size is small and the sediment concentration exceeds a threshold of approximately ∼2-10 g/l (*Winterwerp*, 2002). Under these conditions the timescale for particle settling is long relative to timescales of the waves and turbulence. As a result of the above requirements for formation, the vast majority of observations of WSGF have been reported on continental shelves near the mouths of rivers where the combination of a large supply of fine sediment and high wave energy results in the resuspension of recently deposited and unconsolidated sediment (*Ogston et al.*, 2000; *Traykovski et al.*, 2000, 2007; *Ma et al.*, 2010; *Hale and Ogston*, 2015). When samples of bottom sediments were acquired, field studies have predominantly reported distributions dominated by clays and silts, with mean (or median) particle sizes typically on the order of 4-8 μm and containing very small percentages of sand (*Traykovski et al.*, 2000, 2007; *Ma et al.*, 2008; *Jaramillo et al.*, 2009).

3.2 Study site and methods

The Stratification Impacts on Nearshore Sediment (STRAINS) experiment made hydrodynamic and sediment transport measurements in the region of freshwater influence formed by the Rhine River along the Dutch coast in 2013 and 2014 (*Horner-Devine et al.*, 2017; *Flores et al.*, 2017).

The measurements presented here document a WSGF event during the first major storm of the 2014 fall season (Figure 3.1c), which coincided with a period of low river outflow; discharge from the Rhine River was persistently below its annual average of 2500 m^{3}s^{-1} during the 30 days prior to our deployment (Figure 3.1d). High waves and strong tides occur in this region and are mostly responsible for the observed sediment transport patterns (*Pietrzak et al.*, 2011; *Flores et al.*, 2017). Depth-averaged tidal currents are on the order of 1 ms^{-1} and severe storms during the fall and winter generate wind waves that can easily reach 4-5 m. Nonetheless, the conditions and setting are unique relative to previous observations of WSGF. The Rhine River is not a significant source of coastal sediments, with the exception of extreme flood events (*Pietrzak et al.*, 2011), and seabed composition consists primarily of fine to medium sands with particle size ranging between 100-300 μm in 8-10 m depth and typically decreasing in the offshore direction (*Janssen and Mulder*, 2005).

The measurement location is adjacent to the Sand Engine (*Stive et al.*, 2013), a mega nourishment completed in 2012 (Figure 3.1 a). While the emplacement of the Sand Engine undoubtedly provides a large source of coastal sediment, monitoring has shown that the particle size distribution around it has coarsened since its construction *Huisman et al.* (2016). Moreover, observed suspended sediment concentrations are in the same range as those observed prior to its construction (*van der Hout et al.*, 2015; *Flores et al.*, 2017; *Horner-Devine et al.*, 2017). This suggests that the Sand Engine does not provide a large source of fine sediments. Seafloor slopes and median grain sizes around the Sand Engine (*Huisman et al.*, 2016) show values that are representative of many continental shelf areas; thus, while this is a unique setting in which a WSGF has been documented, it is not unique in terms of coastal morphology and sedimentology.

The measurement site was 10 km north of the Rhine River mouth and consisted of two frames, one in 8m and one in 12m of water (Figure 3.1 a, b). Suspended sediment concentration and velocity profiles were obtained using acoustic and optical instrumentation. Down-looking Acoustic Backscattering Systems (ABS) were used to estimate near-bottom sediment concentration profiles at both sites, with transducers measuring at frequencies of 1, 2, 3 and 4 MHz with 1 cm vertical resolution from approximately 1 m above the bottom to the seabed (*Betteridge et al.*, 2008; *Thorne et al.*, 2011). They were calibrated in the laboratory using particle size distributions representative
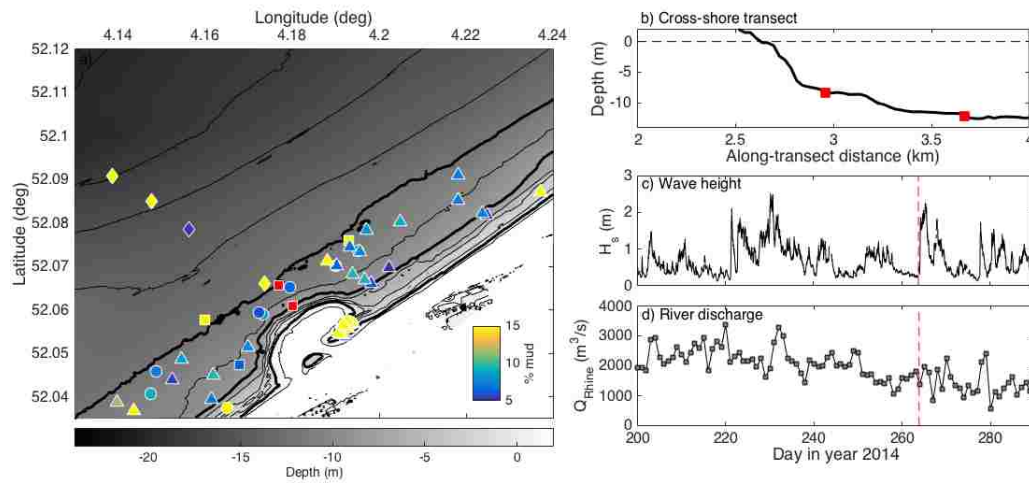
Figure 3.1: Study area, wave heights and Rhine River discharge. (a) Bathymetry of the study area, including tripod locations (red squares). Thick black lines indicate the 0m, 8m and 12m depth contours. Contours have been drawn every 2m. Color squares, circles and triangles represent locations with mud fraction greater than 5%, for surveys taken in October 2013, August 2014 and February 2015, respectively. Diamonds correspond to bed samples taken on deployment day, in September 2014 (b) Cross-shelf profile. Red squares mark tripod locations. (c) Significant wave height. (d) Rhine River discharge. Dashed red line in panels c) and d) indicate the beginning of the 2-day storm that generated the wave-supported gravity flow event.

of the field site. Sediment concentrations at four elevations (10, 20, 30 and 50 cmab) were collected using Optical Backscatter Sensors(OBS) at the 8m site, which were calibrated in the laboratory using sediment collected in the field. The ABS data are used primarily in the analyses since they provide much better vertical resolution, though the magnitude of the observed concentrations is confirmed in the OBS measurements.

Velocity profiles were measured using a combination of acoustic instruments. At the 8m site, near-bed velocity profiles were obtained using a down-looking acoustic doppler profiler (Nortek Aquadopp) measuring at 2Hz with 1 cm vertical resolution. An up-looking profiler measured velocities through the upper portion of the water column, with the first bin centered 1.6 m above the bottom and vertical resolution of 0.5m. An ADV (Acoustic Doppler Velocimeter) was placed approximately 70 cm above the bottom and was used to connect the near-bottom and upper water column velocity profiles, as well as to obtain estimations of the bottom stress and drag coefficient. The velocity measurements were averaged in 10-min bursts and cubic splines were used to smooth vertical profiles. Unfortunately, the down-looking profiler at the 12m site did not give usable data due to a battery malfunction. Data quality measures showed ping-to-ping correlations and signal-to-noise ratios within the recommended range of values in the near-bottom region. East-North velocity components were rotated to alongshore and cross-shore components using tidal ellipse properties, obtained by performing harmonic analysis (*Pawlowicz et al.*, 2002) on the velocity data.

Bed elevation was determined using both the location of maximum acoustic backscatter (ABS) and the hydrodynamic bottom, where the mean velocities become zero in the down-looking Aquadopp data. In general, the surface of maximum acoustic backscatter agreed well with the location of zero mean velocities.

Wave orbital velocities were computed from the spectra of the ADV data over the typical wave frequency range from 0.02 to 0.3 Hz (*Wiberg and Sherwood*, 2008). Bed shear stress was calculated using a 1D wave-current bottom boundary layer model (*Grant and Madsen*, 1986). Wave direction was estimated from directional data from a WaveRider buoy located 1km northeast of the measurement site, and bottom roughness was estimated from ripple heights (η) and wavelengths (λ)

derived from an Acoustic Ripple Profiler using $k_b = 27.7\eta^2/\lambda$ (*Grant and Madsen*, 1986).

3.3   Observations and results

At the beginning of the storm, wave heights increased to 2.5 m (Figure 3.1c) resulting in near-bottom wave orbital velocities on the order of 0.45 ms^{-1} at the 12m site (Figure 3.2a). Combined with the large tidal velocities in the area (*Rijnsburger et al.*, 2016; *De Boer et al.*, 2006), this resulted in high bed stresses that peaked during flood tides and showed an overall five-fold increase with respect to the preceding calm period (Figure 3.2a). Bottom stresses remained elevated for almost 2 days and reached values well above the threshold of resuspension for silts and fine sands. Following the large stresses, sediment concentration profiles measured by the ABSs showed maximum near-bottom concentrations of 40 (g/l) and 50 (g/l) at the 12m and 8m sites (Figure 3.2 b and c), respectively, which are of similar magnitude to those of previously reported WSGF events (*Hale and Ogston*, 2015; *Traykovski et al.*, 2007). Peak concentrations of 10 (g/l) were reported by the OBS 20 cmab at the 8m site (Figure 3.2b), suggesting that at times the high-concentration layer was at least 15-20 cm thick.

Significant bed elevation changes were observed during this event at both sites based on ABS data (Figure 3.2 b, c). At the 12m site these changes resulted in approximately 10 cm of deposition over the course of the event with most of the deposition occurring within a few hours of the beginning of the storm, suggesting that the WSGF was initiated as soon as wave energy increased (Figure 3.2 c). Records from pressure sensors on the frames did not show variations that could be related to instrument settling. The bed elevation also increased by more than 10 cm at the 8 m site; however, the net bed elevation change during the storm was only 5 cm (Figure 3.2 b). The increase in concentration at the 12m site lags that at the 8m site by approximately 2 hours, which is consistent with downslope transport.

The velocity and sediment profiles during the event period reveal clear evidence of gravitational transport (Figure 3.3). Sediment concentration profiles at both sites show a high concentration layer with a thickness ranging between 5-20 cm and high concentration gradients (Figure 3.3 g-
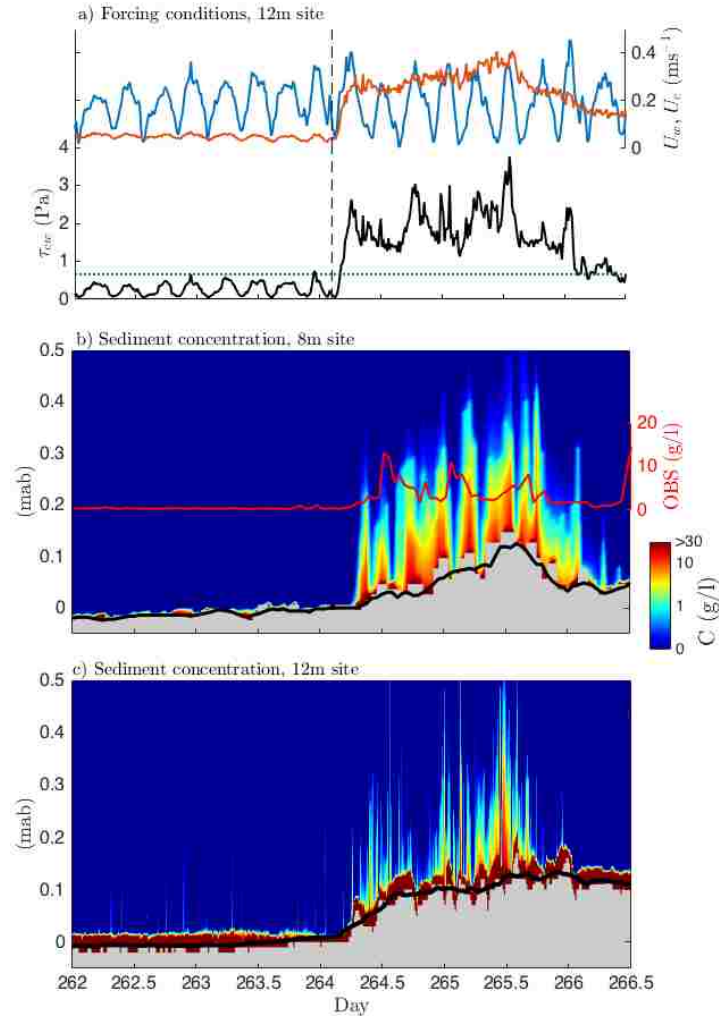
Figure 3.2: Forcing conditions and suspended sediment concentrations. (a) Near-bottom wave orbital velocity (red line), near-bottom tidal currents measured 0.25 mab (blue line) and combined wave-current bottom stress (black line) at the 12m site. Vertical dashed line indicates the arrival of the storm. Horizontal dotted line indicates the critical stress for fine sand particles with $d_{50} = 280$ (μm) (b) Sediment concentrations at the 8m site. Red line represents sediment concentrations measured by the OBS placed 20 cmab (c) Sediment concentration at the 12 m site. The thick black lines in panels (b) and (c) correspond to a lowpass filter of the bed elevation.

i). The concentration profiles show an exponential decay with maximum concentrations near the bed (Figure 3.3 g-i), similar to other field and laboratory experiments (*Lamb and Parsons*, 2005; *Traykovski et al.*, 2007; *Hooshmand et al.*, 2015; *Souza et al.*, 2004).

Phase averaged velocity profiles reveal the vertical structure of the current during slack, peak flood and peak ebb tide periods (Figure 3.3). When tidal currents cease during slack, an offshore-directed jet is observed in the lower 10 cm with weaker offshore flow above it (Figure 3.3 d). The maximum average downslope flow during slack is approximately 2 cm/s, however, individual profiles show cross shore velocities reaching 5 cm/s (Figure 3.3 e,d). This jet is attributed to gravitational flow since it occurs when other forcing ceases and it is vertically confined to the layer of high sediment concentration.

The tidal flow in this region is strongly influenced by density stratification associated with the nearby discharge from the Rhine River (*Visser et al.*, 1994; *Simpson and Souza*, 1995), resulting in cross-shore tidal flow that is onshore during flood tide and offshore during ebb tide (Figure 3.3 b-c). Thus, the tidal current opposes the gravitational flow during flood tide, and we observe that this thins the layer of near-bed offshore flow, but does not completely suppress it (Figure 3.3 e). In contrast, offshore tidal velocities during ebb tide thicken the near-bed layer to approximately 15 cm (Figure 3.3 f). Tidal changes in the thickness of the high concentration layer are consistent with those observed in the velocity profiles; a thin layer during flood and thicker layers during slack and ebb. The alongshore velocity profiles are approximately logarithmic, although modification in the profile due to the influence of stratification is expected (Figure 3.3 a-c). Despite these modulations of the layer thickness by tidal velocities, the average layer thickness remains small $(0.05 - 0.20$ m$)$ compared with the much thicker turbid layers $(1 - 2$ m$)$ observed in systems in which stress from currents are of first order importance to the dynamics of the gravity flow (*Ma et al.*, 2008, 2010). Thus, the dynamics of the gravity flow observed here appear to be dominated by wave stress, even though tidal currents also exert an influence on their structure and direction.

The high concentrations observed during the WSGF resulted in elevated cross-shore sediment transport (Figure 3.4d). The net cross-shore sediment flux due to the WSGF event was an order of
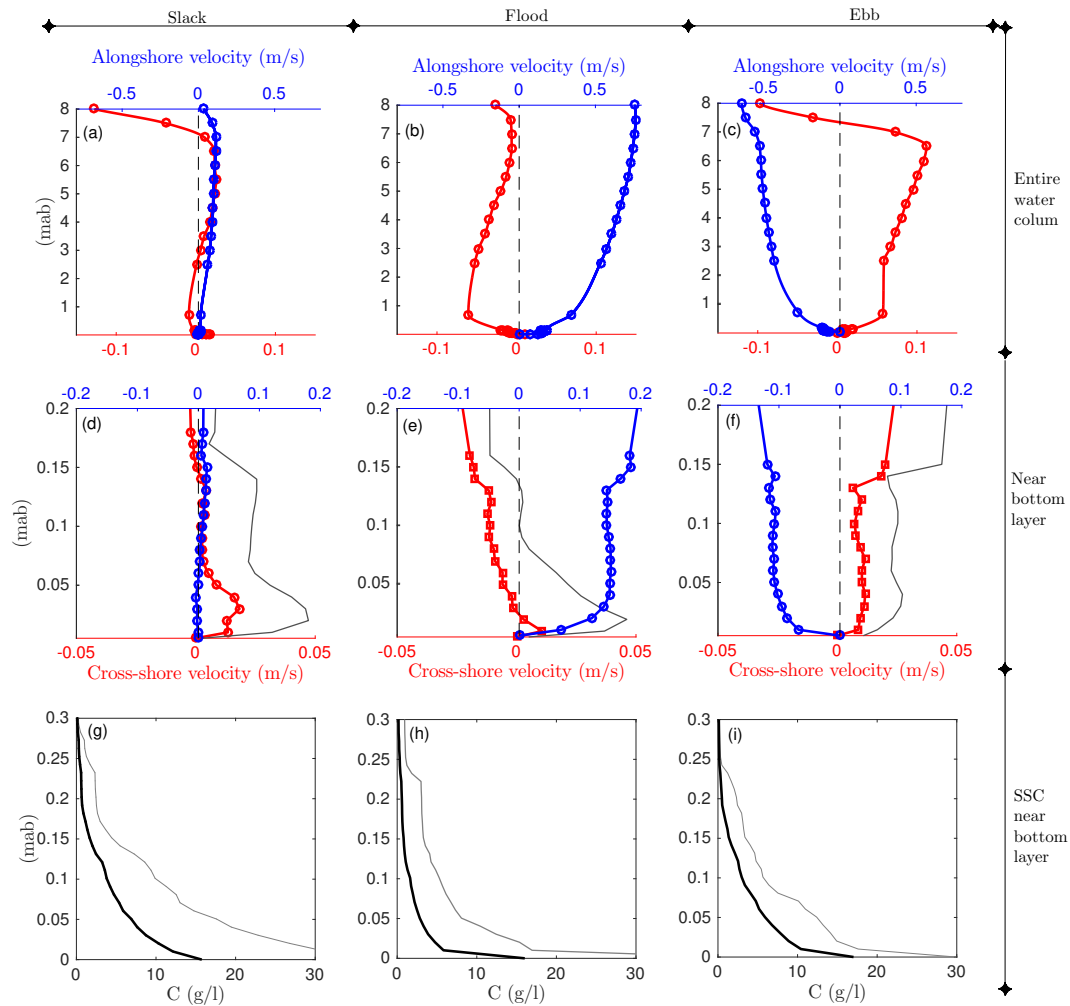
Figure 3.3: Velocity and sediment concentration profiles. (a)-(c) Alongshore (blue) and cross-shore (red) velocity profiles for the entire water column. (d)-(f) Alongshore (blue) and cross-shore (red) velocity profiles over the bottom 20 cm. Gray lines represent the envelope of maximum velocities. (g)-(i) Sediment concentration profiles over the bottom 30 cm. Gray lines correspond to the envelope of maximum observed concentrations at each elevation. Velocity and concentration profiles correspond to phase-averages for the slack, peak flood and peak ebb tidal phases. Each profile was computed using between 6-8 individual profiles. Individual profiles were obtained by averaging the 2Hz data into 10-min bursts. Positive values correspond to flow directed to the northeast (alongshore) and offshore (cross-shore).

magnitude greater than the suspended load transport in the overlying water column (0.5mab to the surface) measured nearby at the 12m site (*Flores et al.*, 2017) or the bedload transport based on the formula of *Madsen* (1991) for the same time period (Figure 3.4 d). In fact, the offshore transport during this 1.5 day WSGF event was much higher than the suspended sediment transport observed during a 30 day period at the nearby 12m site. Sediment concentration measurements were not made in the upper water column at the 8m site.

3.4 *Gravitational velocity, force balance and Richardson number*

The gravitational velocity component, u_g, can be estimated using our near-bed measurements and the force balance presented in Equation 3.1. The thickness of the high concentration layer, H, and the reduced gravity, g', are estimated directly from the sediment concentration profiles (*Traykovski et al.*, 2007). The seabed slope at the 8m site was estimated from bathymetry data as $\alpha = 0.008$. The maximum velocity u_{max} was computed including wave, current and gravitational velocities. The value for the drag coefficient at the 8m site was estimated as $C_D = 0.003$, based on the ADV turbulence measurements outside the wave boundary layer. This value is consistent with values used in previous WSGF studies (*Scully et al.*, 2002, 2003). A detailed presentation of the methods for estimating C_D and its tidal variability are presented in Appendix A. Figure 3.4c shows the comparison between u_g predicted from Equation 3.1 and the measured cross-shore velocity averaged over the high-concentration layer, U_{cross}. Although predicted u_g values are almost always greater than the observed cross-shore velocity, the variability in U_{cross} is well explained by the u_g prediction during slack tides ($R^2 = 0.92$, Figure 3.4c - inset), which suggests that U_{cross} responds directly to changes in the sediment-induced buoyancy, B (Equation 3.1). However, the tidally-influenced variability in U_{cross} exceeds that due to changes in buoyancy except close to slack tide (Figure 3.4c). This is particularly true during flood tides, when the poorest agreement between U_{cross} and u_g is observed as the onshore tidal flow opposes the gravitational flow (Figure 3.4c and Figure 3.3).

In order to evaluate the subtidal momentum balance (Equation 3.1) we set $u_g = 1.6$ cm/s, which corresponds to the average magnitude of U_{cross} during slack tides. This provides a representative gravitational velocity that results from the available sediment-induced buoyancy, without signifi-
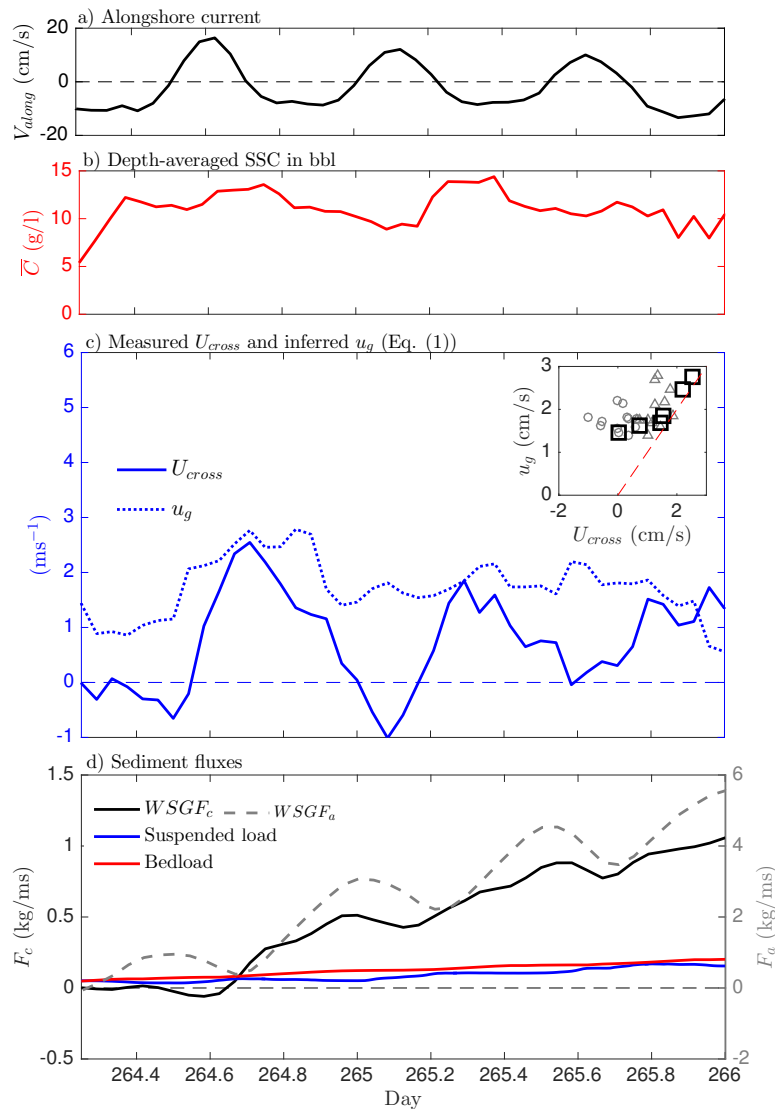
Figure 3.4: Velocity components and sediment fluxes. (a) Near-bed alongshore current. (b) Depth-averaged suspended sediment concentration in the turbid near-bottom boundary layer (c) Gravitational velocity (u_g, dotted blue line), as inferred from the force balance (Equation 3.1), vertically averaged cross-shore velocity over the high-concentration layer (U_{cross}, solid blue line). Inset shows a scatter plot comparison between u_g and U_{cross} for slack (black squares), ebb (gray triangles) and flood (gray circles) tidal phases. (d) Cumulative cross-shore sediment fluxes for the WSGF event (black line), suspended load at the nearby 12m site (blue line) and bedload (red line) and cumulative alongshore flux for the WSGF event (gray dotted line, axis on the right). Positive cross-shore fluxes are offshore, positive alongshore fluxes are directed northwards.

cant tidal influence. Using the mean observed slack tide cross-shore velocity for u_g, the frictional and gravitational terms balance to within 6% after an initial adjustment period (Figure 3.5 b). This good agreement supports previous findings suggesting that WSGF dynamics are governed by a buoyancy-friction balance (*Traykovski et al.*, 2007) and further confirms that the observed flow is indeed a WSGF. The initial adjustment provides information on the initiation and temporal evolution of WSGF. Immediately after the start of the storm the wave forcing, via the friction term, exceeds the buoyancy term, suggesting that the high concentration layer may still be forming. Subsequently, the buoyancy term exceeds the friction term for several hours. This imbalance may have been caused by a slumping event that occurred shortly after the wave energy increased, which may also help to explain the sudden change in bed elevation observed at the 12m site (Figure 3.2 c). The high near-bottom offshore velocities also support the hypothesis that strong gravitational flow occurred during the initial stage of the storm (Figure 3.4 c).

The bulk Richardson number is relatively constant, with the exception of a few hours early in the storm (Figure 3.5c). The constant value observed after day 264.8 supports the hypothesis that a dynamical feedback is established, forming a quasi-steady suspension (*Wright et al.*, 2001). However, we observe a constant value of $Ri_b = 0.01$, which is more than one order of magnitude lower than the canonical value of $Ri_b = 0.25$ typically assumed in WSGF models (*Wright et al.*, 2001; *Scully et al.*, 2002; *Friedrichs and Wright*, 2004; *Friedrichs and Scully*, 2007).

3.5 Discussion

3.5.1 Modeling WSGF

The Richardson number is one of the key parameters often used in the modeling of WSGF. Although $Ri_b = 0.25$ has been widely adopted, data from several previous studies also result in values of the Richardson number below this critical value (*Traykovski et al.*, 2007; *Hsu et al.*, 2009; *Lamb and Parsons*, 2005). Low values of Ri_b, such as those observed in this study, have been ascribed to finite bed erodibility (*Hsu et al.*, 2009). On the Dutch coast it is likely that low erodibility results from the high sand content in the bed; winnowing of fine sediment from the bed during the initial stages of the event will coarsen the bed and reduce erodibility.
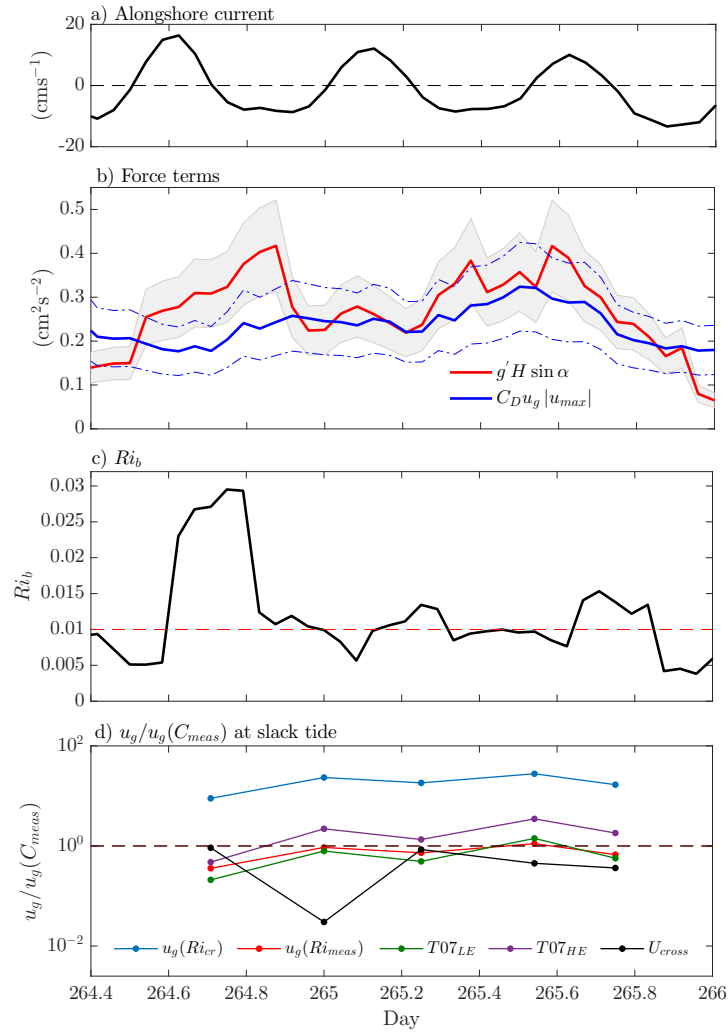
Figure 3.5: Dynamics of the WSGF. (a) Alongshore current. (b) Chezy balance: gravitational (solid red line) and frictional (solid blue line) terms. Gray area is associated to the uncertainty in seabed slope ($\pm 20\%$). Dashed blue line is associated to the uncertainty in u_g, determined based on the standard deviation of u_g during slack tides. (c) Richardson number (Equation 3.2). (d) Gravitational velocities at slack tide, normalized by $u_g(C_{meas})$. Gravitational velocity inferred from Equation 3.1 using a critical Richardson number ($R_c = 0.25$, blue), gravitational velocity inferred from Equation 3.1 using measured Richardson number ($Ri = 0.01$, red), gravitational velocity obtained from *Traykovski et al.* (2007) 1D model using a resuspension parameter $\gamma_0 = 0.002$ ($T07_{LE}$, green), gravitational velocity obtained from *Traykovski et al.* (2007) 1D model using a resuspension parameter $\gamma_0 = 0.005$ ($T07_{HE}$, purple), and measured cross-shore velocity (U_{cross}, black).

In order to test the applicability of WSGF models to our observations, we have estimated gravitational velocities using constant Richardson numbers ($Ri_b = 0.25$ and $Ri_b = 0.01$) and a 1D WSGF mass balance model (*Traykovski et al.*, 2007). These estimates are shown in Figure 3.5d. For the vertical mass balance model, we have included estimates using both low and high erodibility coefficients (commonly referred to as γ_0). As these models rely on the use of Equation 3.1 but differ on how they estimate sediment concentrations, the gravitational velocities in Figure 3.5d have been normalized by $u_g(C_{meas})$. This represents the gravitational velocities obtained from Equation 3.1 using the measured sediment concentrations profiles (as in Figure 3.4c), which we consider to be the best estimation these models could provide. For reference, we have also included the measured cross-shore velocities, U_{cross}. The best agreement is achieved with the use of $Ri_b = 0.01$, although $u_g(Ri = 0.01)$ underpredicts $u_g(C_{meas})$ at times when the peak in Ri_b is observed (Figure 3.5c, around day 264.6). The use of $Ri_b = 0.25$ results in u_g values with a mean of 27 cm/s, an order of magnitude higher than the observed velocities or $u_g(C_{meas})$. The mass balance model gives results that are much closer to $u_g(C_{meas})$, with estimates obtained using low bed erodibility showing a better performance overall than those obtained with high erodibility.

The models used in our comparison differ in terms of the physical processes that are assumed to be responsible for limiting cross-shore transport in WSGF. The use of $Ri_b = 0.25$ assumes that sediment availability is unlimited and that the high suspension layer is critically stratified. This model significantly overpredicts transport in the observed WSGC. However, Ri_b is observed to be constant during most of the WSGF event, albeit at a value much lower than 0.25, suggesting that a critical Ri_b model may still be appropriate. Use of such a model for coarse particle suspensions would require a suitable prediction of Ri_b. In the mass balance model (*Traykovski et al.*, 2007), on the other hand, sediment suspension is limited by erosion from the seabed. This model compares well with the current observations, especially when the bed erodibility is assumed to be low.

3.5.2   The role of fine sediment

Hindered settling, which occurs preferentially in fine sediments, is thought to be a key component in the maintenance of high density suspensions (*Winterwerp*, 2002). This suggests that fine sediment is likely to have played an important role in the observed WSGF, despite the fact that the bed sediment is predominantly sandy. Our measurements did not resolve the particle size distribution of the sediment suspension, and thus we cannot determine the fraction of fine sediment present in the high concentration layer or how important fine sediment was in the generation of the WSGF.

Field surveys have confirmed the presence of fines in the region; mud deposits and areas with high turbidity are frequently observed off the Dutch coast and along the southern bight of the North Sea (*Fettweis and Van den Eynde*, 2003; *Van Alphen*, 1990; *Visser et al.*, 1991; *van der Hout et al.*, 2015, 2017). Detailed surveys of the size distribution of sands (*Huisman et al.*, 2016) give a reasonable estimate of the fraction of fine sediment ($< 63 \ \mu m$) on the seabed and the spatial and temporal variability of transient mud deposits close to our measurement sites (Figure ?? a). Locations with seabed fine sediment fractions greater than 5% were frequently observed all around the measurement sites, and some of them showed fractions reaching up to 30% particularly near the 12 m isobath (Figure 3.1 a). Hindered settling has been shown to occur when the sediment concentration exceeds 2-10 g/l (*Winterwerp*, 2002). Near-bed concentrations of fine sediment in this range can be achieved even in this relatively coarse mixture considering that the observed near-bed concentrations ranged from 10 - 50 g/l (Figures 3.3 and 3.4b) and bed fractions ranged from 5% to 30%. This estimate assumes that the high concentration layer has a similar size distribution to the seabed. While this is not know, winnowing may actually result in a finer size distribution in the layer than on the seabed.

3.6   Summary

The movement of sediment across gently sloping continental shelves has long been one of the most poorly understood components of source-to-sink sediment budgets (*Nittrouer and Wright*, 1994). Previous studies have identified WSGF as a leading process for cross-shelf transport of muds, but the measurements presented here are the first to document the importance of WSGF to cross-shelf

transport and morphological evolution on sandy inner shelves. Offshore transport associated with this 1.5 day WSGF event was much higher than estimates of bedload transport and measurements of suspended sediment transport at a nearby site during a 30 day period. During this period WSGF was the dominant mechanism of cross-shore transport in this region, however, the frequency of occurrence is unknown.

The observed WSGF dynamics support the use of the Chezy balance for modeling WSGF on sandy seabeds. They also suggest that particle size plays a key role in determining the intensity of downslope transport, and that a critical Richardson number ($Ri_c = 0.25$) cannot be achieved in sandy environments. Coarse particles may influence WSGF transport either by modifying the dynamics of the turbulent suspension due to higher settling rates or by reducing the bed erodibility. Future work is necessary to determine the relative importance of these processes in limiting transport in mixed sediment suspensions.

Nonetheless, the occurrence of this event under conditions unique from previous observations suggests that WSGF may occur more frequently and in a much wider range of shelf locations than previously thought.

3.7   Appendix A: Estimation of the drag coefficient, C_D

The dynamics of wave-supported gravity flows (WSGF) are thought to be governed by a force balance between the downslope gravitational component resulting from the sediment-induced buoyancy anomaly, and friction arising from flow over the stationary seabed (*Wright et al.*, 2001; *Scully et al.*, 2002; *Wright and Friedrichs*, 2006). This force balance is usually written as

$$Hg' \sin \alpha = C_D u_g \left| u_{max} \right| \tag{3.3}$$

In order to evaluate Equation 3.3 using measured near-bed velocities and sediment concentrations, we require prior knowledge of the drag coefficient, C_D. We estimated the drag coefficient based on the turbulence measurements (ADV sampling at 8 Hz) taken close the bed, as the mean value of

two methods: i) the wave-current boundary layer model of *Grant and Madsen* (1979) and ii) the eddy correlation method (*Kim et al.*, 2000). For each method, the drag coefficient is computed as $C_D = u_*^2/U^2$, where u_* is the friction velocity and U is the speed of the mean current. The *Grant and Madsen* (1979) model outputs u_* directly based on the wave and current forcing input. Provided that the turbulence measurements were taken in the region of constant stress, the eddy correlation method establishes that $u_*^2 = \overline{u'w'}$, where u' and w' are the horizontal and vertical velocity fluctuations, respectively. Values for the drag coefficient were computed for the time period when the WSGF was observed, and then a mean value was obtained. We recognize that the application of these methods may not be ideal to this particular situation but our measurements did not resolve the variability of C_D within the wave boundary layer. Application of these methods during the time when the WSGF was observed yielded a value of $C_D = 0.0032 \approx 0.003$, which was found to be consistent with values of the drag coefficient previously used in WSGF modeling studies (*Scully et al.*, 2002; *Friedrichs and Wright*, 2004). Figure 3.6a shows C_D as inferred from the near-bottom turbulence measurements.

The drag coefficient can also be inferred directly from Equation 3.3 if estimates of the gravitational velocity u_g are available. This approach was not used in the manuscript since we were looking to evaluate the force terms to investigate WSGF dynamics rather than focusing on one particular term of Equation 3.3. However, direct measurements of C_D in WSGF are not commonly available and might be valuable in future WSGF studies. We estimated C_D from Equation 3.3 using measured sediment concentrations, wave and current velocities and two estimates for gravitational velocities: i) the measured cross-shore velocities (U_{cross}) and ii) $u_g = 1.6$ (cm/s), which corresponds to the average of U_{cross} at slack tides, as discussed in the manuscript. These estimates are shown in Figure 3.6b. For case i), C_D shows a mean value of $C_D = 0.0043$ (dashed red line in Figure 3.6b), which is indeed a little higher than the value obtained from our turbulence measurements. For case ii) C_D has a mean value of $C_D = 0.0034$, which is very close to the estimates obtained from the ADV measurements. As was shown in the manuscript, our measurements of near-bed velocity agree well with u_g at times close to slack tide, when tidal currents cease. If we only consider slack tides to obtain an averaged C_D, we get $C_D = 0.0045$ when using U_{cross} and $C_D = 0.0037$ when using $u_g = 1.6$ (cm/s). Both of these results are still close to the estimate obtained using the ADV

Chapter 4

THE INFLUENCE OF TIDAL STRAINING IN THE FORMATION OF NEARSHORE TURBIDITY MAXIMUM ZONES IN REGIONS OF FRESHWATER INFLUENCE

4.1 Introduction

Density stratification has a profound influence on circulation and sediment transport dynamics in estuaries (*Hansen and Rattray*, 1965; *Burchard et al.*, 2013; *Geyer and MacCready*, 2014) and in shallow coastal seas (*Simpson et al.*, 1990; *Stacey et al.*, 1999; *Pietrzak et al.*, 2011). Shallow coastal seas that are strongly influenced by riverine freshwater discharge, such as Liverpool Bay (*Rippeth et al.*, 2001), San Francisco Bay (*Stacey et al.*, 2001) and the Rhine outflow region (*Simpson and Souza*, 1995) are often referred to as regions of freshwater influence (ROFIs) (*Simpson*, 1997). In the absence of surface gravity waves, the instantaneous movement of sediments is usually related to the tidal flow, however, the long term transport is driven by the residual currents and turbulent dispersion processes which are significantly modified by the presence of longitudinal and lateral density gradients (*Jay and Musiak*, 1994; *Lerczak and Geyer*, 2004; *Scully and Friedrichs*, 2007). An important consequence of density gradients in estuaries and ROFIs is the generation of subtidal (low frequency) landward sediment fluxes near the bed, which may lead to sediment convergence and regions of very high turbidity (*Jay and Musiak*, 1994; *Geyer et al.*, 2001; *Burchard et al.*, 2013; *Souza and Lane*, 2013).

In estuaries, subtidal landward sediment fluxes and the formation of estuarine turbidity maxima (ETM) are generally attributed to tidal asymmetries in eddy viscosity generated by tidal straining (*Jay and Musiak*, 1994; *Scully and Friedrichs*, 2007). Tidal straining (*Simpson et al.*, 1990) leads to a periodic cycle of stratification and destratification in which the water column has the tendency to become more mixed during flood tide. Stronger mixing during the flood transports more momentum to the near-bed region, enhancing the near-bed landward currents relative to the ebb currents and resulting in upstream residual transport (*Jay and Musiak*, 1994; *Geyer et al.*, 2000; *Scully and*

Friedrichs, 2007). While other density-driven mechanisms, such as gravitational (*Burchard and Hetland*, 2010) and lateral (*Lerczak and Geyer*, 2004) circulation, typically support the formation of ETMs, tidal straining has been systematically identified as the most important contributor to landward sediment fluxes in estuaries with strong tidal forcing (*Geyer et al.*, 2001; *Burchard et al.*, 2011, 2013). The effects of tidal straining on circulation and sediment transport dynamics have been extensively documented in the York Estuary (*Simpson et al.*, 2005), the Columbia River (*Jay and Smith*, 1990; *Jay and Musiak*, 1994), the Hudson River estuary (*Geyer et al.*, 2000), the Dee River estuary (*Amoudry et al.*, 2014) and the Rotterdam waterway (*de Nijs et al.*, 2011).

Tidal straining has also been observed along the coast in ROFI systems (*Simpson et al.*, 1990; *Simpson and Souza*, 1995; *Souza et al.*, 2008), where it likewise results in periodic variations in stratification that control turbulence (*Rippeth et al.*, 2001; *Fisher et al.*, 2002; *Souza et al.*, 2008). An example of the semi-diurnal variations in stratification, current structure and near-bed sediment transport induced by tidal straining is shown in Figure 4.1 for a shallow site along the Rhine ROFI (*Flores et al.*, 2017; *Horner-Devine et al.*, 2017); a strongly sheared alongshore (Figure 4.1a) and cross-shore current profile (Figure 4.1b) that results from the differences (Figure 4.1c) leads to a net landward transport at depth (Figure 4.1d). Despite the fact that landward sediment fluxes are frequently observed in ROFIs during stratified conditions (*Souza and Lane*, 2013; *van der Hout et al.*, 2015; *Brown et al.*, 2015; *Flores et al.*, 2017), the occurrence of tidal straining has not been explicitly linked to observations of turbidity maximum zones in coastal regions.

The occurrence of turbidity maximum zones (TMZs) is relevant for a wide variety of ecological problems, as they are often related to the inhibition of primary production, hypoxia and the accumulation of contaminants (*Eisma*, 1990; *Yoshiyama and Sharp*, 2006). High concentrations of suspended sediments can impair the optimal functioning of coastal engineering projects, which may then require unplanned modifications. The accumulation of fine sediments in estuarine waterways and coastal regions usually results in the need for further human intervention, that often materializes in the form of dredging activities. Thus, a better understanding of the physical processes that determine sediment pathways and accumulation zones is essential to improve our capability to sustainably managing coastal areas.
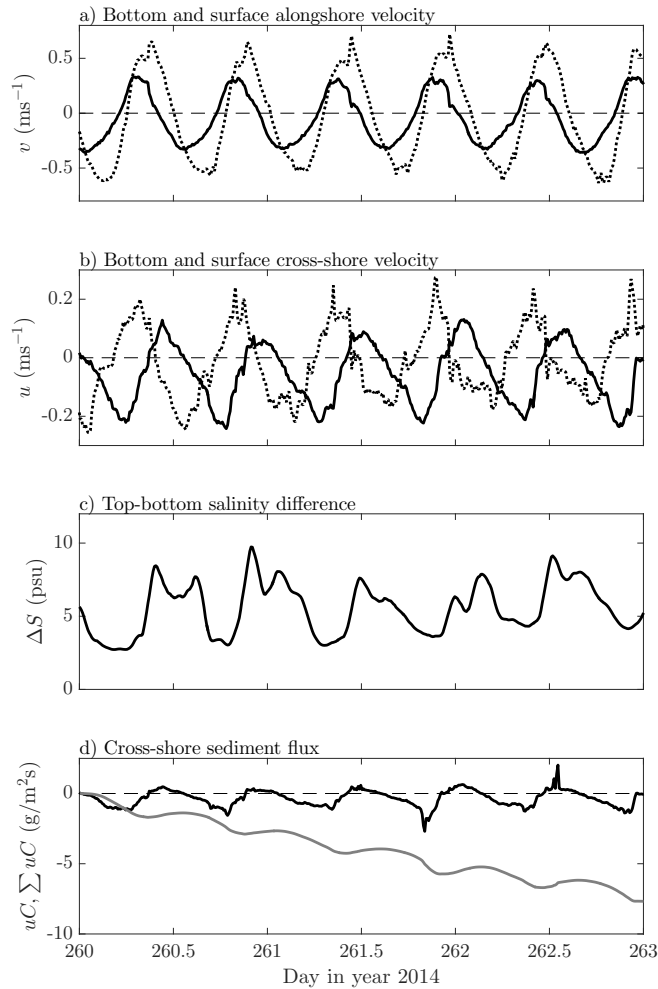
Figure 4.1: Field measurements along the Rhine ROFI. (a) Bottom (solid line) and surface (dotted line) alongshore velocities. (b) Bottom (solid line) and surface (dotted line) cross-shore velocities. (c) Top-bottom salinity difference. (d) Instantaneous (black line) and cumulative (gray line) near-bottom cross-shore sediment fluxes. These measurements were part of the STRAINS (Stratification Impacts on Nearshore Sediment) field campaign (*Flores et al.*, 2017; *Rijnsburger et al.*, 2018) and were taken 10 km north of the mouth of the Rhine River, in 18 m of water, approximately 5 km off the coast. In all panels, bottom refers to measurements collected approximately 0.5 m above the bed and surface refers to measurements collected 1 m below the surface.

In the Rhine ROFI, a persistent turbidity maximum zone is observed between 1-3 km from the coast (Figure 4.2a), spanning tens of kilometers in the alongshore direction and with peak sediment concentrations typically located 1.25-1.5 km off the coast (*van der Hout et al.*, 2015, 2017). Based on data collected during several measurement campaigns along the years (*Van Alphen*, 1990; *Joordens et al.*, 2001; *van der Hout et al.*, 2015), this TMZ is thought to extend at least 80 km downstream of the mouth of the Rhine-Meuse estuary (Figure 4.2b), making it the main feature of the fine sediment dynamics along the Dutch coast. As a result of vertical stratification, high suspended sediment concentrations are usually confined to the lower half of the water column (Figure 4.2a) and are not detectable by remote sensing or satellite imagery (*Pietrzak et al.*, 2011; *van der Hout et al.*, 2015). The nearshore location of this TMZ is certainly relevant for the coastal engineering solutions implemented along the Dutch coast in response to climate change and sea level rise (e.g. *Stive et al.*, 2013), and it has also been shown to control the distribution of nutrients, plankton and chlorophyll-a in the coastal ecosystem (*Joordens et al.*, 2001; *van der Hout et al.*, 2017). While the mechanisms leading to the maintenance of this extensive TMZ have not yet been fully investigated, tidal straining has been hypothesized to be one of the principal processes contributing to its formation (*van der Hout et al.*, 2015).

Although dynamics similar to those observed in estuaries frequently extend out onto the shelf in river plumes (*Horner-Devine et al.*, 2015) and ROFI systems (*Simpson*, 1997), particle trapping and the formation of persistent turbidity maximum zones are rarely observed in coastal seas. One notable exception are ROFIs, where the interplay between tides, density gradients and bottom friction seem to favor convergence processes that may lead to the formation of turbidity maximum zones (e.g. *Souza and Lane*, 2013; *van der Hout et al.*, 2015; *Brown et al.*, 2015; *van der Hout et al.*, 2017). The aim of this study is to investigate the mechanisms by which tidal straining in ROFIs generates offshore turbidity maximum zones.

From the dynamics shown in Figure 4.1 it is clear that while the term tidal straining has been used in both estuaries and open coastal seas, the mechanics of the tidal straining process can be different in these two settings. In ROFIs where the tide behaves as a standing wave, such as Liverpool Bay
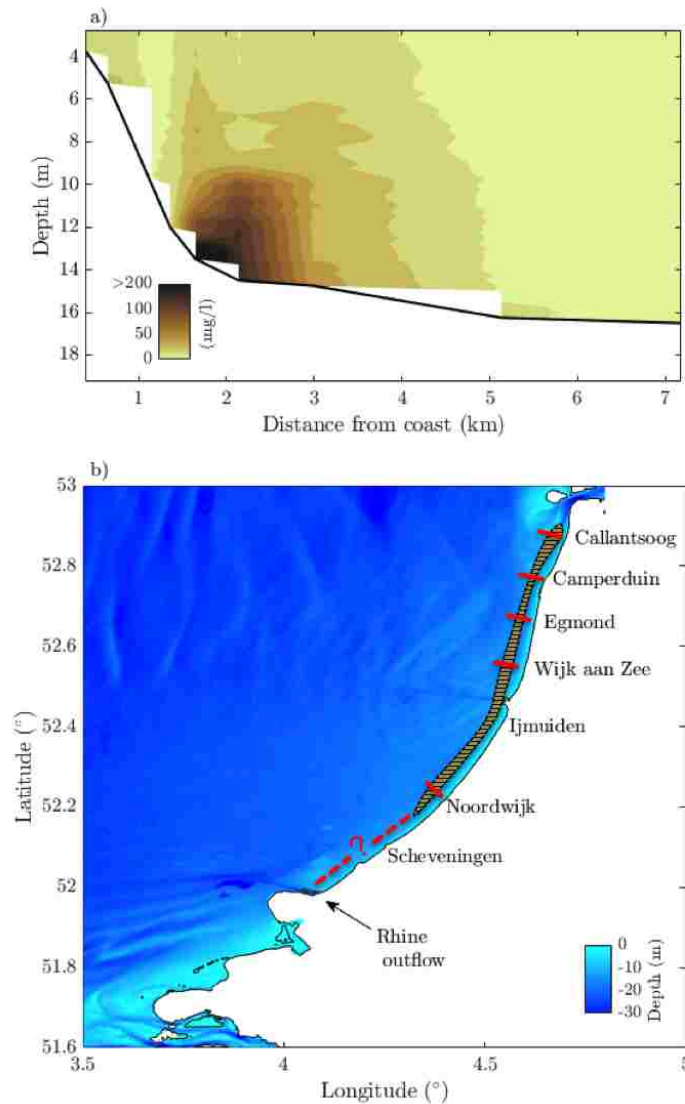
Figure 4.2: Observation of a nearshore turbidity maximum zone along the Dutch coast. (a) Suspended sediment concentrations along a transect off the coast at Egmond (see panel b). These measurements correspond to those of *van der Hout et al.* (2015). (b) Bathymetry along the Dutch coast. Red lines represent locations were a coastal TMZ was observed in the field measurements of *van der Hout et al.* (2015) and *Van Alphen* (1990). The alongshore extension of the TMZ has been indicated by the brown filled area. The red dashed line indicates that the TMZ could potentially extend to the river mouth, although no measurements have been reported in that area.

(*Rippeth et al.*, 2001; *Palmer*, 2010), the major axis of the tidal currents is aligned with the horizontal density gradient and tidal straining occurs similarly as it does in estuaries. The situation is different in regions where the tide behaves as a progressive wave, such as the Rhine (*Simpson et al.*, 1993), since the tidal currents are not aligned with the main horizontal density gradient. Tidal straining cannot occur in these systems without additional processes that enable the interaction between the tidal shear and the density gradients (*Visser et al.*, 1994; *Simpson and Souza*, 1995; **?**). Earth's rotation, which is usually neglected in estuaries (*Scully and Friedrichs*, 2007; *Burchard et al.*, 2013), plays a key role in the generation of tidal straining in these ROFI systems by setting the thickness of the cyclonic and anticyclonic boundary layers (*Prandle*, 1982; *Visser et al.*, 1994; *Palmer*, 2010; *Souza*, 2013).

Tidal straining in ROFIs with progressive tides is a frictional process that relies on the anticyclonic frictional boundary layer being much thicker than the water depth, such that in the presence of a pycnocline the top and bottom layers become dynamically decoupled (*Visser et al.*, 1994; *Verspecht et al.*, 2010). The decoupling of the top and bottom layers by the reduction of eddy viscosity at the pycnocline leads to the modification of the tidal ellipses, which develop a strong cross-shore component (*Visser et al.*, 1994; *Simpson and Souza*, 1995; *Souza et al.*, 1997). As the upper layer does not feel bottom friction, it develops strong anticyclonic rotation, which in turns enhances the cyclonic character of the near-bottom currents. The surface and bottom currents rotate in opposite directions, leading to the high cross-shore shear that results in the periodic cross-shore straining of the density field (*Visser et al.*, 1994; *Simpson and Souza*, 1995; *Palmer*, 2010; *Souza*, 2013). Tidal current ellipticity, defined as the ratio of semi-minor to semi-major axes of the tidal ellipses, has therefore been considered a direct measure of the occurrence of tidal straining in ROFI systems (*Visser et al.*, 1994; *Souza et al.*, 1997; *De Boer et al.*, 2006). In the Rhine, ellipticities approaching 0.4 have been observed both in the field (*Visser et al.*, 1994; **?**; *Flores et al.*, 2017) and numerical simulations (*De Boer et al.*, 2006) during stratified conditions.

Tidal straining can then occur in the direction of the main tidal flow, as in estuaries or coastal regions where the tide propagates as a standing wave, or in a direction that is perpendicular to it, as in coastal systems with progressive tides. In order to clearly differentiate these environments,

here we will refer to the tidal straining that occurs in progressive wave ROFI systems as elliptical tidal straining (ETS).

In the present study, we focus on the role that ETS plays in the generation of turbidity maximum zones in coastal regions. An idealized numerical model is specifically designed to reproduce the cross-shore circulation dynamics that are primarily set by the tidal straining mechanism, characteristic of ROFI systems with progressive tides. We test the hypothesis that tides and elliptical tidal straining result in the formation of a coastal turbidity maximum that is detached from the shoreline (as in Figure 4.2), and investigate the mechanisms by which cross-shore sediment convergence is generated. The parameter space under consideration covers primarily variations in the horizontal density gradients and the Coriolis parameter, which are thought to be the the critical parameters governing tidal straining dynamics, as discussed in Section 4.2. The sensitivity of the location of the TMZ and the magnitude of the suspended sediment concentrations is also tested with regard to sediment particle size (Rouse number). Based on the results of our simulations, we provide a parameter space for the formation of TMZs in shallow coastal seas, specified in terms of non-dimensional numbers controlling the buoyancy and frictional influence.

This chapter is organized as follows: In Section 4.2 we explore the scaling relationships that define the parameter space for ETS and define the major non-dimensional numbers that are used throughout the paper. In Section 4.3 we describe the numerical model, grid setup, simulation scenarios, parameters and forcing required to perform the hydrodynamic and sediment transport simulations. In Section 4.4 we use model results to describe the processes leading to the formation of a TMZ for a base case scenario. In Section 4.5 we investigate the parameter space for the the generation of TMZ by tidal straining, including the influence of particle size distributions and sensitivity to seabed slopes and water depth. We present our final conclusions in Section 4.6.

4.2 Non-dimensional parameters

An important goal of this paper is to develop a predictive understanding for the occurrence of ETS and turbidity maximum zones in coastal shelf seas. To this end, we use key non-dimensional parameters that have been previously identified as controls on the dynamics of tidal flows subjected

to the influence of horizontal density gradients and Earth's rotation (*Simpson et al.*, 1990; **?**; *Burchard et al.*, 2013; *Souza*, 2013). The relative importance of the horizontal density gradients on the dynamics of estuarine and coastal flows is typically quantified in terms of the Simpson number (*Simpson et al.*, 1990; *Stacey et al.*, 2010; *Burchard et al.*, 2013; *Geyer and MacCready*, 2014):

$$Si = -\frac{g}{\rho_0} \frac{\partial \rho}{\partial x} \frac{H^2}{u_*^2} \tag{4.1}$$

where g is the gravitational acceleration, ρ_0 is a reference density, ρ is density, H is water depth, and $u_* = \sqrt{C_D} U$ is the friction velocity, where C_D is a drag coefficient and U is a tidal velocity scale. The Simpson number has also been referred to as the horizontal Richardson number, Ri_x (*Monismith et al.*, 1996; *Stacey et al.*, 2001; *Burchard and Hetland*, 2010), and represents the ratio of potential energy change due to straining to the rate of production of turbulent kinetic energy (*Geyer and MacCready*, 2014). The Simpson number quantifies the importance of tidal straining in the generation of residual flows in estuaries and ROFIs (*Simpson et al.*, 1990, 2005; *Burchard and Hetland*, 2010). For small values of Si, tidal mixing is able to eliminate the stratification caused by tidal straining and by the baroclinic mean flows, whereas for large values of Si ($Si \sim 1$) the water column will stratify (*Monismith et al.*, 1996). For intermediate values of Si, the SIPS (strain-induced periodic stratification) regime is expected to occur (*Simpson et al.*, 1990).

The Stokes number has been used to quantify the relative importance of friction and inertia in oscillatory tidal flows (*Prandle*, 1982; *Baumert and Radach*, 1992; *Winant*, 2007; *Burchard and Schuttelaars*, 2012; *Souza*, 2013), and is defined as as the ratio of boundary layer height to total water depth,

$$Stk = \frac{\delta}{h} \tag{4.2}$$

Souza (2013) used the Stokes number to explain frictional tidal dynamics and water column structure in the Irish Sea, concluding that $Stk \sim 1$ is a good predictor for the location of tidal mixing fronts. A Stokes number $Stk \geq 1$ means that the frictional layer is greater than the water depth, which in practical terms is interpreted as a boundary layer that covers the full water column.

ROFIs are frictional systems with strong rotational currents (*Souza et al.*, 1997; *De Boer et al.*, 2006), and therefore the effects of Earth's rotation have to be accounted for when estimating the frictional depth, δ. The effects of Earth's rotation on friction and boundary layer height can be accounted for by decomposing the tidal ellipses into cyclonic and anticyclonic rotational components (*Godin*, 1972; *Prandle*, 1982), each of which has a boundary layer thickness given by (*Godin*, 1972; *Prandle*, 1982; *Soulsby*, 1983; *Souza*, 2013),

$$\delta_{\pm} = \frac{C_0 u_*}{\omega \pm f} \tag{4.3}$$

where C_0 is a constant with value 0.075 (*Soulsby*, 1983; *Souza*, 2013), f is the Coriolis parameter and ω is the tidal frequency. In Equation 4.3, the plus sign is used to obtain the height of the cyclonic boundary layer and the minus sign to obtain the height of the anticyclonic boundary layer. For the rest of this paper, we will use the anticyclonic Stokes number (*Prandle*, 1982; *Soulsby*, 1983; *Souza*, 2013),

$$Stk_- = \frac{\delta_-}{h} \tag{4.4}$$

which can be readily computed for any given latitude (f) by only specifying a tidal velocity scale. For tidal ellipses to be modified by stratification, it is necessary that $Stk_- \geq 1$, i.e., that the anticyclonic boundary layer reaches the surface (*Souza*, 2013; *Visser et al.*, 1994; *Simpson and Souza*, 1995).

As pointed out earlier, in regions such as the Rhine and Liverpool Bay ROFIs, the interaction between the tidal shear and the horizontal density gradient results in tidal velocity profiles that deviate significantly from the otherwise rectilinear tidal flow (*Visser et al.*, 1994; *Palmer*, 2010). Hence, a third non-dimensional parameter that is of dynamical interest in ROFIs is the tidal current ellipticity, and more specifically, the top-bottom ellipticity difference

$$\Delta \varepsilon = \varepsilon_b - \varepsilon_s \tag{4.5}$$

In the presence of ETS, $\Delta \varepsilon$ will always be a positive number since the bottom layer will have positive (cyclonic) rotation and the surface layer will have negative (anticyclonic) rotation. Large

values of $\Delta\varepsilon$ are indicative of the development of strong counter-rotating top and bottom cross-shore current components, while low values of $\Delta\varepsilon$ are associated to the absence of ETS and a rectilinear alongshore tidal flow (*Souza et al.*, 1997).

The occurrence of turbidity maximum regions is also conditioned to the particle size distribution of bed sediments. The influence of particle size and associated settling velocities is usually assessed in terms of the Rouse number (*Rouse*, 1937; *Hunt*, 1954), which describes the balance between particle settling and upward turbulent transport of sediment,

$$Ro = \frac{w_s}{\kappa u_*} \tag{4.6}$$

where w_s is the particle settling velocity (constant), $\kappa = 0.4$ is the von Karman constant, and u_* is the friction velocity scale ($u_* \sim \sqrt{C_D}U$).

4.3   Numerical Model

We use the Regional Ocean Modeling System (ROMS) to simulate circulation and sediment transport dynamics in an idealized ROFI ETS system. ROMS is a three-dimensional, free surface, primitive equation ocean model with a curvilinear orthogonal horizontal grid and a stretched terrain-following vertical grid. The model solves finite-difference approximations of the Reynolds-averaged Navier-Stokes equations using the Boussinesq and hydrostatic approximations (*Shchepetkin and McWilliams*, 2005; *Warner et al.*, 2008a), and has been extensively used in idealized and realistic numerical simulations of shelf dynamics and associated transport processes (*Harris et al.*, 2008; *Warner et al.*, 2008b; *Chen et al.*, 2013; *Horwitz and Lentz*, 2014; *Kumar et al.*, 2015). This section describes the model configuration and the physical parameters used in the numerical simulations.

The model is intended to reproduce the hydrodynamics and sediment transport processes characteristic of systems with ETS, such as the Rhine ROFI. Early studies in the far field of the Rhine ROFI (*Simpson and Souza*, 1995; *Souza and James*, 1996) have suggested that the dynamics are, to a first order, two-dimensional, with cross-shore variability in density and currents dominating over those in the alongshore direction. More recently, *De Boer et al.* (2008) showed that cross-shore

straining is the dominant mechanism controlling the variability in water column stability and current structure in this region. Consequently, all of our analyses is then focused on the cross-shore dynamics that may lead to the formation of a TMZ. Our model is not intended to resolve along coast variability and does not simulate processes that are characteristic of the near-field (and mid-field) river plume region, such as the propagation of tidal plume fronts (*Horner-Devine et al.*, 2017) and alongshore advection or straining (*De Boer et al.*, 2008). While alongshore processes have implications for ROFI sediment transport, the simulations presented here focus on the simplest case in order to understand the fundamental processes that lead to cross-shore sediment convergence along this type of ROFI system.

4.3.1   Model setup

The model domain consists of open ocean boundaries at the north, south and west boundaries and a coastal wall at the eastern boundary. The bathymetry is alongshore uniform, with a minimum depth at the coastal wall of $h = 3$ (m) and maximum depth of $h = 30$ (m). The bathymetry was taken from the bathymetric profile presented in *van der Hout et al.* (2017) (Figure 4.2a), which we approximated to a 2-slope profile; a steep profile in the nearshore region ($x < 1500$ m) with slope of $\alpha = 0.01$ and a much milder profile towards deeper shelf waters with a slope of $\alpha = 0.001$. An exponential fit was later performed to obtain a smooth transition between slopes (Figure 4.3a). The choice of a maximum depth of $h = 30$ (m) is representative of the Rhine ROFI region along the southern North Sea (*Pietrzak et al.*, 2011). The stretched vertical grid has $N = 32$ levels with enhanced resolution in the near-bottom and near-surface regions (Figure 4.3a).

In order to avoid undesirable boundary effects, the alongshore domain was set 50 to km with a resolution of $\Delta y = 500$ (m), for a total of 100 grid cells. All of the analyses and figures presented here were made using model output from cross-sections located towards the middle of the domain. The tide is specified as a progressive Kelvin wave and, in order to let the Kelvin wave decay completely, the cross-shore domain spans 700 km (only part of the domain is shown here) but with variable grid resolution; grid size increases linearly from a minimum of $\Delta x = 20$ m in regions adjacent to the coastal wall to a maximum of $\Delta x = 5000$ m in offshore regions with flat bottom where dynamics
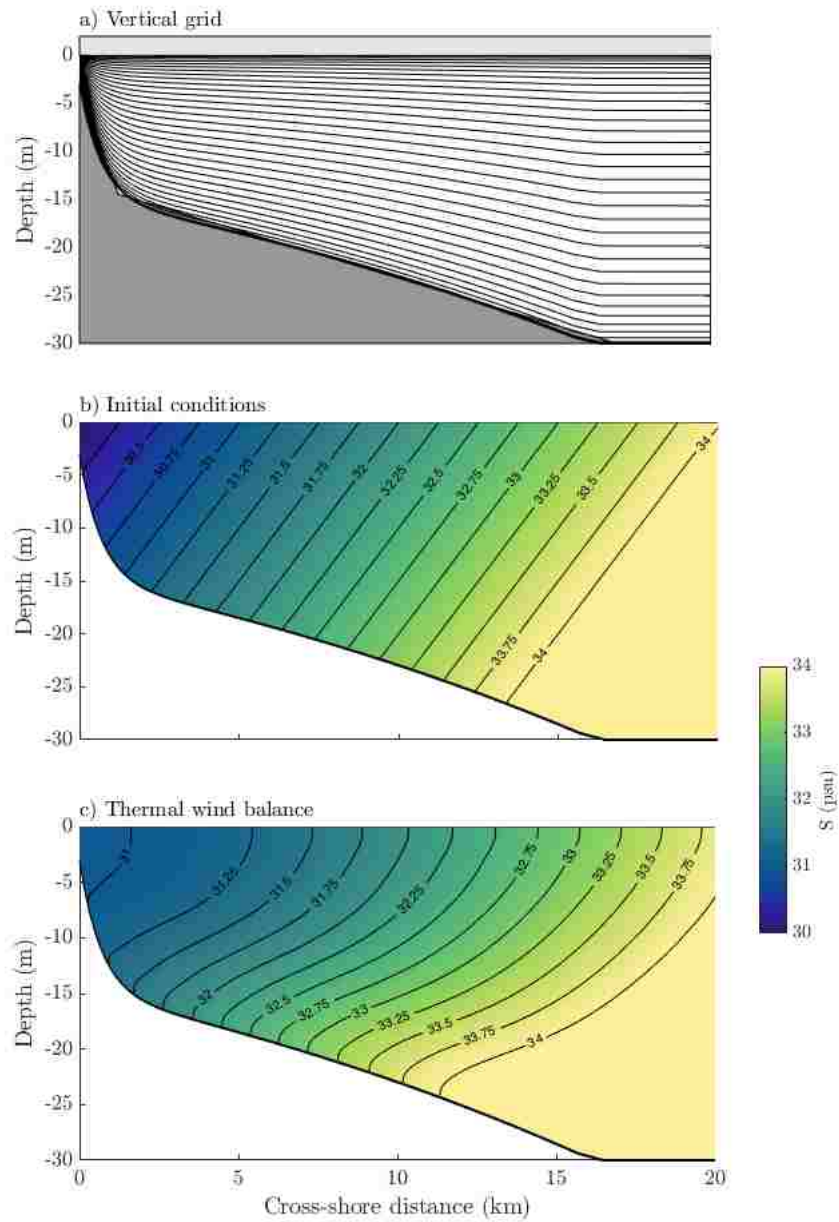
Figure 4.3: (a) Model bathymetry and vertical terrain-following grid with near-surface and near-bottom increased vertical resolution. Initial (b) and adjusted (c, due to thermal wind balance) salinity structure for the base case scenario.

are not of interest for this study.

Simulations are conducted following two steps; first, we let the system develop a thermal wind balance in response to an imposed depth-uniform cross-shore density gradient (Figure 4.3b,c). Salinities and temperatures are then clamped at the thermal wind values at Northern boundary, in order to provide a constant buoyancy forcing that would result in the establishment of a bottom attached buoyant coastal current (Figure 4.3c). No gradient boundary conditions are specified for the salinity, temperature and suspended sediments at the Southern and Eastern boundaries. After the thermal wind equilibrium has been reached and the buoyant coastal current has developed, we force the system with tidal elevations and velocities at each of the open boundaries, which are specified based on the expressions for a Kelvin wave with linear bottom friction (*Jacobs*, 2004; *De Boer et al.*, 2006; *Roos et al.*, 2011). Chapman and Flather boundary conditions (*Marchesiello et al.*, 2001) were used for the tidal elevation and depth-averaged veloctiies, respectively, at the Northern, Southern and Western boundaries.

In ROMS, the system of governing equations is closed using parameterizations of the Reynolds stresses in terms of eddy viscosities and eddy diffusivities. Eddy viscosities and eddy diffusivities were estimated using the $\kappa - \epsilon$ turbulence closure model (*Umlauf and Burchard*, 2003; *Warner et al.*, 2005). Background values for eddy viscosities and diffusivities are taken as $K_v = 10^{-5}$ m^{2}s^{-1} and $K_s = 10^{-6}$ m^{2}s^{-1}, respectively. Bottom stresses are determined using a logarithmic drag layer with a roughness length that results in a drag coefficient of approximately $C_D = 0.003$.

The sediment transport calculations used ROMS algorithms, which are described in detail in (*Warner et al.*, 2008a). Calculations are initialized with zero concentrations in the water column, thus all the sediment in suspension in the model results from tidally-induced erosion from the seabed. Boundary conditions for the sediment calculations are specified as zero gradient boundary conditions at all boundaries.

4.3.2 Base Case

We start by describing the parameters used in the base case. Unless otherwise specified, all results shown here correspond to this set of parameters. Runs are initialized with a cross-shore uniform salinity gradient of 2×10^{-4} (psu/m), which results in a depth-uniform cross-shore density gradient of approximately 1.523×10^{-4} (kg/m^{-4}). This value is representative of the far field region of the Rhine ROFI (*Rijnsburger et al.*, 2016). Vertical stratification is imposed with a constant salinity gradient of 0.05 (psu/m), which results in a buoyancy frequency of $N^2 = 1.2 \times 10^{-4}$ (s^{-2}). The width of the stratified region is set as 20 km, which is the typical cross-shore extension of the plume (*Souza et al.*, 2008). As a result of the horizontal and vertical stratification, the isopycnals start uniformly diagonal as shown in Figure 4.3b. The model is forced with semi-diurnal tides with a frequency of $\omega = 1.4054 \times 10^{-4}$ s (M2 tidal constituent) and amplitude of $\eta_0 = 0.8$ m, which is characteristic of neap tides along the Rhine region (*Flores et al.*, 2017; *Rijnsburger et al.*, 2018). The Coriolis parameter was set as $f = 1.13 \times 10^{-4}$ (s^{-1}), corresponding to a latitude of 51°. No additional forcing is included in the simulations (e.g. winds, waves) since our primary focus is the effect of ETS dynamics.

The sediment bed consists of 1 layer, with one class of fine and one class of coarse (sandy-sized) sediments. Particle sizes are specified as 10 μm and 200 μm, respectively, corresponding to fine silts and fine sands. Settling velocities and critical stress for erosion are specified based on the chosen particle size; the settling velocity and threshold for erosion for the fine fraction are 0.1 mms^{-1} and 0.05 Pa, whereas for the sandy fraction these parameters are specified as 1 cms^{-1} and 0.2 Pa. The erodibility constant is chosen to be 5×10^{-4} (kg/m^{2}s) for both classes of sediment, which falls within the range of reported values (*Sanford and Maa*, 2001). The bed is initialized with a silt fraction of 20% and a fine sand fraction of 80%, following observations along the Dutch Coast (*Flores et al.*, 2018; *Huisman et al.*, 2016).

4.3.3 Numerical simulations

Other model runs start with the base case parameters, and they typically vary one of the remaining model parameters. Horizontal density gradients range from 3.81×10^{-5} to 2.3×10^{-4} (kgm^{-4}),

corresponding to salinity gradients ranging from 5×10^{-5} to 3×10^{-4} (psum^{-1}). A case without stratification has also been included in order to investigate whether a TMZ would form form under well-mixed conditions. The Coriolis parameter was estimated as $f = 2\Omega \sin(\psi)$, where Ω and ψ are the planetary rotation frequency and latitude, respectively, and was chosen to span latitudes from $26°$ to $56°$. Parameters such as settling velocity, tidal range and water depth were also varied. The model runs used in this study are summarized in Tables 4.1 and 4.2. Model runs specified in Table 4.1 were performed using the bathymetric profile shown in Figure 4.3, whereas the models runs specified in Table 4.2 were performed using a bathymetric profile with a much smoother transition between shallow and deeper waters (not shown). In Tables 4.1 and 4.2, $\overline{H}$ refers to a mean water depth computed based on the bathymetric profile,

$$\overline{H} = \frac{1}{x_0} \int_0^{x_0} h(x)dx \tag{4.7}$$

where x_0 corresponds to the cross-shore extension of the initially stratified region, $x_0 = 20$ km. To complete the parameter space with regard to the non-dimensional number described in section 4.2 a small number of simulations were conducted with varying density gradients and the Coriolis parameter.

4.4 Model results

4.4.1 Density and current structure: ETS

The modeled current and salinity structure display periodic variations matching those observed in ROFI systems with ETS (Figure 4.4). The time series shown in Figure 4.4 are for a time period where a quasi-steady state has been reached, several tidal cycles after the tides were initiated. In the Rhine, tidal elevations are in phase with tidal velocities due to the progressive Kelvin wave character of the tide; positive alongshore velocities correspond to flood tide and negative velocities correspond to ebb tide (Figure 4.4a,b). The alongshore velocities are stronger during the flood, as the tidal flow and the density-driven circulation (thermal wind) act in the same direction. The cross-shore velocities are $180°$ out of phase between the surface and bottom (Figure 4.4 c,d), and show a marked two layer structure (Figure 4.4c) that is indicative of the presence of a pycnocline at a depth of approximately 5 m below the surface. Maximum offshore and onshore velocities are

Table 4.1: Model Runs

Cases	Run	$\partial\rho/\partial x$ (10^{-4}kgm^{-4})	f (10^{-4} s^{-1})	$\overline{H}$ (m)	η_0 (m)	w_s (mms^{-1})	Si	Stk_-
Base Case	1	1.52	1.13	22.8	0.8	0.1	1.55	
	2	0					0	
	3	0.381					0.39	
	4	0.762					0.77	
	5	1.143					1.16	2.66
Vary $\partial\rho/\partial x$	6	1.714	1.13	22.8	0.8	0.1	1.75	
	7	1.910					1.94	
	8	2.09					2.12	
	9	2.28					2.33	
	10		0.638				1.47	0.98
	11		0.749				1.49	1.14
Vary f	12	1.52	0.855	22.8	0.8	0.1	1.51	1.35
	13		0.954				1.52	1.65
	14		1.046				1.54	2.06
	15		1.21				1.57	3.71
Vary η_0	16	1.52	1.13	22.8	0.6	0.1	1.78	1.88
	17				1.00		1.03	3.26
	18					0.05		
	19					0.2		
Vary w_s	20	1.52	1.13	22.8	0.8	0.5	1.55	2.66
	21					0.8		
	22					1		
	23	1.910	0.749	22.8	0.8	0.1	1.81	1.14
	24	1.714	0.855	22.8	0.8	0.1	1.69	1.35
	25	1.143	0.954	22.8	0.8	0.1	1.14	1.64
	26	0.762	0.855	22.8	0.8	0.1	0.76	1.35

Table 4.2: Model Runs

Cases	Run	$\partial\rho/\partial x$ (10^{-4}kgm^{-4})	f (10^{-4} s^{-1})	$\overline{H}$ (m)	η_0 (m)	w_s (mms^{-1})	Si	Stk_-
	27	0					0	
	28	0.381					0.22	
	29	0.762					0.45	
	30	1.143					0.68	
Vary $\partial\rho/\partial x$	31	1.52	1.13	17.6	0.8	0.1	0.911	3.53
	32	1.714					1.023	
	33	1.910					1.14	
	34	2.28					1.25	
	35		0.638				0.86	1.28
	36		0.749				0.88	1.49
	37		0.855				0.89	1.77
Vary f	38	1.52	0.954	17.6	0.8	0.1	0.9	2.15
	39		1.046				0.9	2.7
	40		1.13				0.91	3.52
	41		1.21				0.92	4.88
Vary η_0	42	1.52	1.13	17.6	0.6	0.1	1.56	2.65
	43				1.00		0.61	4.28

observed at slack tide, whereas minimum values are observed at times close to peak ebb and peak flood tides. The observed cross-shore shear is on the order of 0.2-0.3 ms^{-1}, which is of similar magnitude as the vertical shear in the dominant alongshore currents (Figure 4.4b,d).

The semi-diurnal cycle of stratification-destratification is clearly observed in Figure 4.4f, with maximum stratification occurring close to high water (peak flood) and minimum stratification at low water (peak ebb) as is characteristic of the Rhine ROFI (*Simpson and Souza*, 1995; *De Boer et al.*, 2006). The stratifying phase occurs from low water to high water, whereas the de-stratifying phase occurs from high water until the following low water (Figure 4.4b,f). Due to the progressive character of the tidal wave both phases include part of the ebb and flood tides, differing from the tidal straining mechanism observed in estuaries and ROFIs with standing tides where stratification increases during the ebb and decreases during flood (*Simpson et al.*, 1990; *Jay and Musiak*, 1994; *Scully and Friedrichs*, 2007). Maximum and minimum top-bottom salinity differences are on the order of 1 psu and 0.05 psu, respectively, suggesting that the water column almost reaches a completely well-mixed state during the peak ebb flow at this particular location in 15 m of water (Figure 4.4f).

The highest suspended sediment concentrations are observed at times when the water column is stratified (Figure 4.4e,g). Suspended sediment concentrations show a marked semi-diurnal variability (Figure 4.4g), indicating that the dynamics at this site are governed by horizontal advection. Despite the fact that a quarter-diurnal signal resulting from local resuspension is not apparent (Figure 4.4g), we note that the source of all sediment in the model is tidally-induced sediment resuspension as we did not provide background concentrations throughout the water column. The absence of a quarter-diurnal signal is explained by a limited supply of erodible sediment from the bed (we only provided one sediment layer) and a small settling velocity. The cross-shore suspended sediment fluxes (Figure 4.4h) shows both onshore and offshore fluxes that occur during the stratifying and de-stratifying phases of the semi-diurnal cycle, respectively. The net near-bed transport is landward (onshore) over the 3.5 tidal cycles shown in Figure 4.4h (gray line). Further examination of the sediment fluxes and the mechanisms leading to subtidal transport is presented in Section 4.4.2.
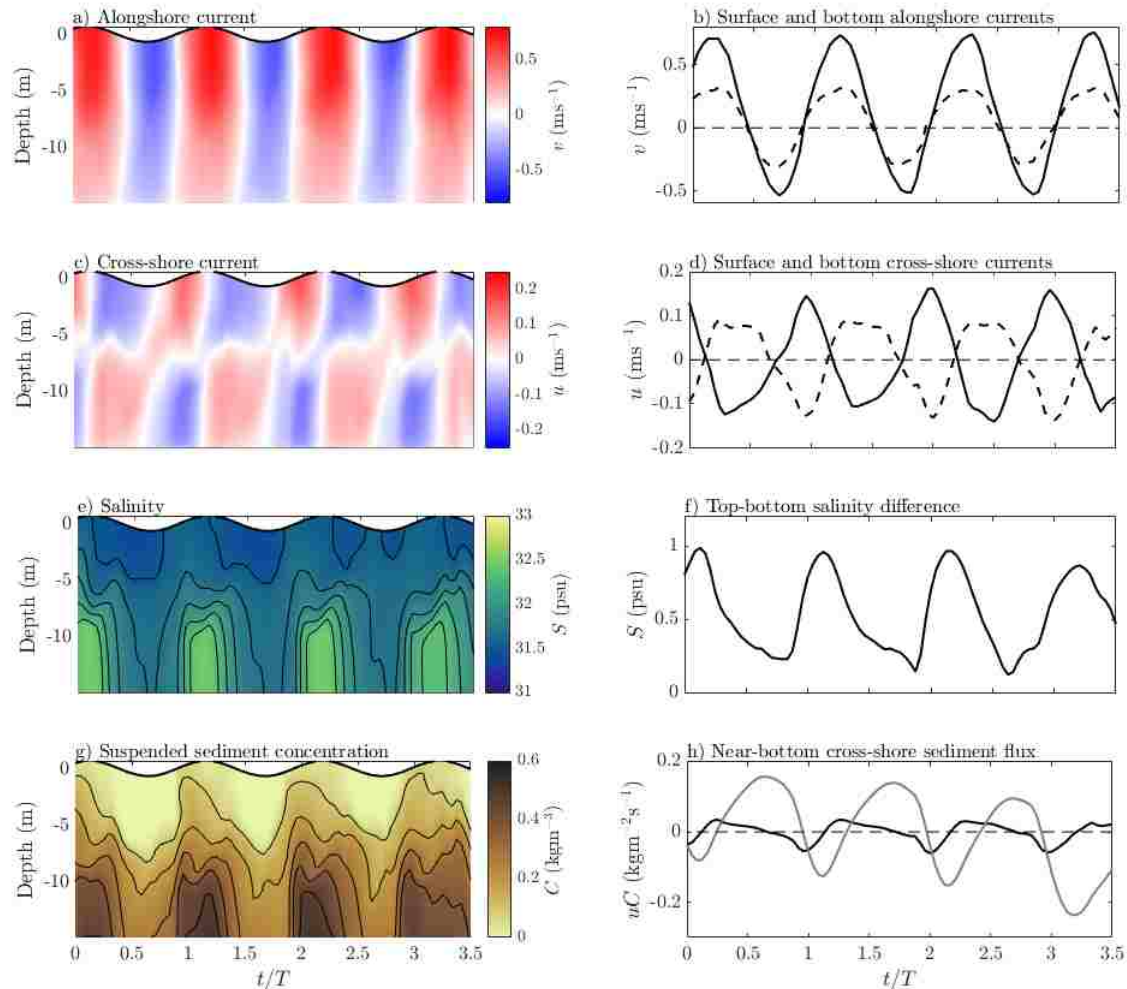
Figure 4.4: ETS and sediment fluxes for the base case. (a) Alongshore current. (b) Time series of bottom (dashed line) and surface (solid line) and surface alongshore current. (c) Cross-shore current. (d) Time series of bottom (dashed line) and surface (solid line) cross-shore current. (e) Salinity structure. (f) Time series of top-bottom salinity difference, ΔS. (g) Suspended sediment concentration. (h) Instantaneous (black line) and cumulative (gray line) near-bottom cross-shore fluxes. All panels show data corresponding to a site located in approximately 15 m of water. Positive alongshore current values correspond to the flood tide. Positive cross-shore current values correspond to offshore flow.

The ellipticity of the bottom and surface currents is shown in Figure 4.5a. Bottom currents show positive ellipticity, consistent with the expected cyclonic rotation, while the surface currents show negative ellipticity and thus rotate anti-cyclonically. Maximum near-bed and near-surface ellipticities reach 0.5 and -0.3, respectively, leading to a maximum top-bottom ellipticity difference of $\Delta\varepsilon \sim 0.8$. These values are consistent with the field observations of *Visser et al.* (1994) and *Souza et al.* (1997), and the model results of *De Boer et al.* (2006). The fact that near-bed currents show greater ellipticity is attributed to the concentration of frictional effects in the lower layer due to the presence of a pycnocline. Maximum tidal current ellipticities (surface and bottom) occur seaward of the region of maximum horizontal density gradient (Figure 4.5a,b), in regions of high vertical stratification. The tidally averaged salinity (Figure 4.5c) shows the structure of a bottom attached buoyant coastal current that is characteristic of shallow river plumes (*Chapman and Lentz*, 1997; *Geyer et al.*, 2004; *Horner-Devine et al.*, 2015). On a subtidal timescale, we observe a two layer structure with a generally well-mixed bottom region as a result of the vertical mixing associated with the tidal currents, and a very stratified upper layer. This is consistent with previous modeling studies in the Rhine ROFI (*Ruddick et al.*, 1995; *De Boer et al.*, 2006).

The density and current structure are thus consistent with the ETS observed in the far field of the Rhine ROFI (*Visser et al.*, 1994; *Simpson and Souza*, 1995; *Simpson*, 1997). They are also consistent with the field measurements presented in Figure 4.1, despite the fact that those measurements were taken close to the Rhine River mouth where other processes, such as the advection of tidal plume fronts (*Horner-Devine et al.*, 2017; *Flores et al.*, 2017; *Rijnsburger et al.*, 2018), may obscure the ETS dynamics.

4.4.2 Turbidity maximum zone and sediment fluxes

The main objective of this modeling study is to investigate whether ETS leads to cross-shore sediment convergence and the formation of a coastal turbidity maximum zone, such as the one depicted in Figure 4.2a. For comparison, we also show the response of the system for the well mixed case, i.e., when no initial stratification is specified. Suspended sediment concentrations for Run 2 (see Table 4.1) are shown in Figure 4.6b, where it is clear that a localized turbidity maximum zone
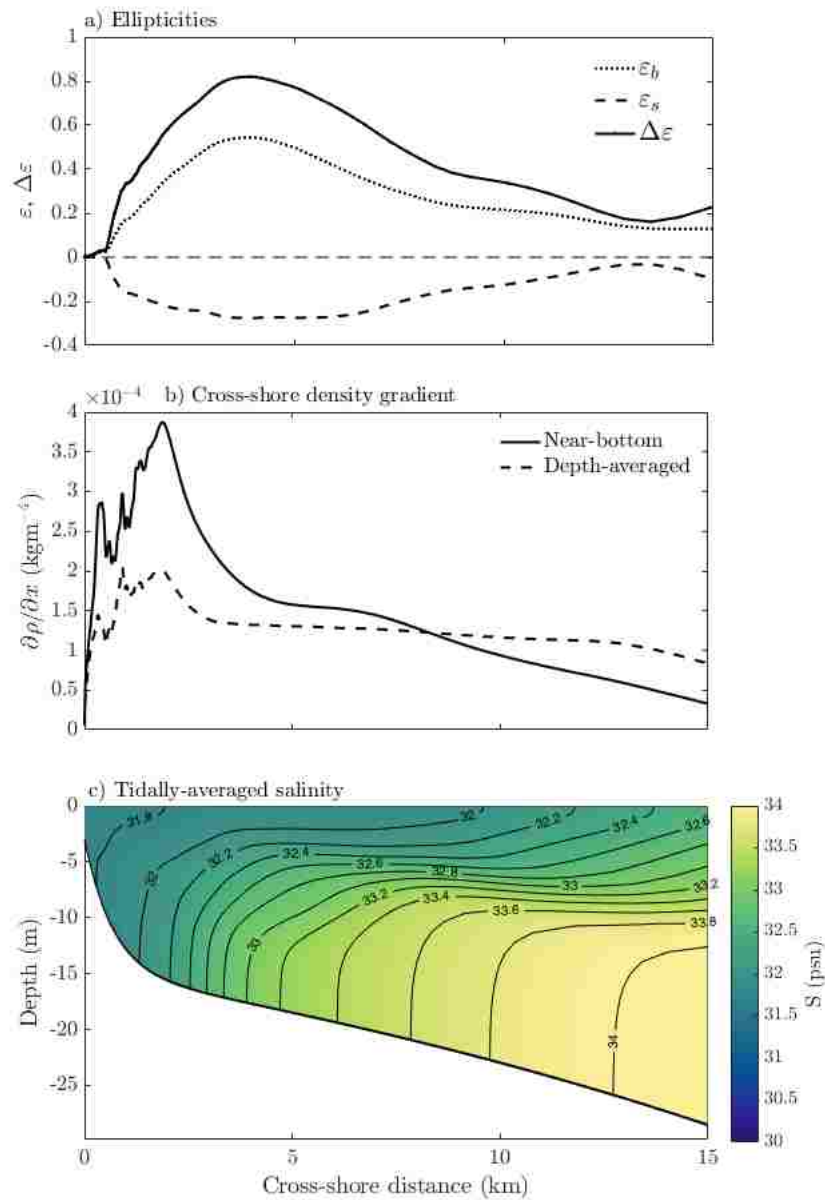
Figure 4.5: (a) Near-bottom (dotted line) and near-surface (dashed line) tidal current ellipticity, and top-bottom ellipticity difference (solid line). (b) Near-bottom (solid line) and depth-averaged (dashed line) cross-shore density gradients. (c) Subtidal salinity structure.

did not form, although suspended sediment concentrations are generally high in nearshore regions. Due to the absence of stratification, suspended sediments are mixed over the entire water column and typical Rouse profiles are observed throughout the domain (Figure 4.6e,f). Suspended sediment concentrations are greater near the shore as a result of enhanced sediment resuspension, and maximum depth-averaged concentrations occur at water depths of 5-8 m (Figure 4.6b). From this, two important observations can be made; first, bed stress resulting from the tidal currents is large enough to erode the seabed and resuspend fine sediments, and second, we do not observe asymmetries between the flood and ebb phases of the tide (Figure 4.6e,f).

The flow is significantly different for the stratified case (Base case, Run 1; Figure 4.6d). We find that the combination of a tidal flow capable of resuspending fine sediments and ETS dynamics (as shown in Figures 4.4 and 4.5) indeed result in the formation of a nearshore TMZ. We observe a localized region with high suspended sediment concentrations extending between 1.5-4 km from the coast and in water depths greater than 12m. Due to vertical stratification, the TMZ is confined to the near-bed region. The location and extension of the TMZ is remarkably similar to the observations reported by *van der Hout et al.* (2015), which are reproduced in Figure 4.2a. The landward limit of the TMZ corresponds well with the tidally-averaged position of the salinity (density) front (Figure 4.4c) and the maximum near-bed horizontal density gradient (Figure 4.4b). The overall extension and position of the TMZ is well predicted by the regions of high tidal current ellipticity, particularly that of the near-bed currents, $\varepsilon_b \geq 0.5$ (Figures 4.5a and Figure 4.6d).

Subtidal sediment fluxes and effective transport velocity

In order to investigate the mechanisms that lead to sediment convergence and the generation of the TMZ, we decompose the residual cross-shore sediment flux into contributions from the residual tidal current and the tidal fluctuations (*Burchard et al.*, 2008; *Schulz and Umlauf*, 2016),

$$\langle uC \rangle = \langle u \rangle \langle C \rangle + \left\langle \tilde{u}\tilde{C} \right\rangle \tag{4.8}$$

where u is the cross-shore velocity, C is the suspended sediment concentration, $\tilde{u} = u - \langle u \rangle$, $\tilde{C} = C - \langle C \rangle$ and the brackets denote the tidal averaging operator $\langle u \rangle = \frac{1}{T}\int_0^T u dt$, where T is
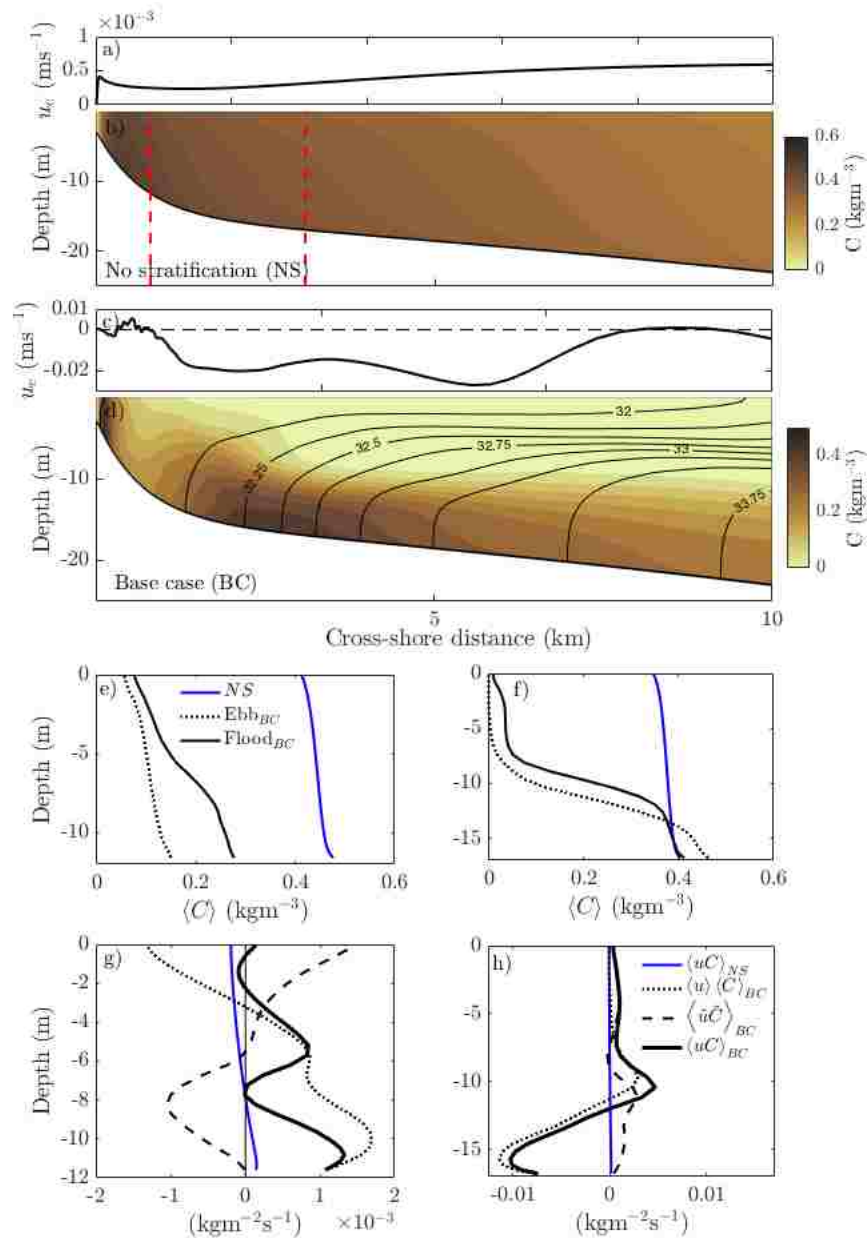
Figure 4.6: (a) Near-bed effective transport velocity (Equation 4.9) for the no stratification (NS) case. (b) Tidally-averaged suspended sediment concentrations for the no stratification case. (c) Near-bed effective transport velocity for the base case (BC). (d) Tidally-averaged suspended sediment concentrations for the base case. (e) Ebb (dotted lines) and Flood (solid lines) suspended sediment concentration profile at a cross-shore section indicated by the leftmost vertical red dashed line in panel (b). Blue indicates concentration for the no stratification case, black indicates concentrations for the base case. (f) Same as e) but at a cross-shore location indicated by the rightmost red dashed vertical line in panel b). (g) Residual transport components at the cross-shore location indicated by the leftmost red dashed line in panel b). Blue indicates values for the no stratification case, black indicates values for the base case. (h) Same as g) but at a cross-shore location indicated by the rightmost red dashed vertical line in panel b).

the tidal period. The first term on the right hand side of Equation 4.8 represents the contribution from the residual currents to the total subtidal transport, whereas the second term represents the contribution from the covariance between the cross-shore velocity and sediment concentration. This last term is usually referred to as tidal pumping (*Scully and Friedrichs*, 2007). Dividing Equation 4.8 by the tidally-averaged sediment concentration, $\langle C \rangle$, gives a quantity that can be interpreted as an effective transport velocity at which suspended sediment is transported across isobaths (*Schulz and Umlauf*, 2016),

$$u_e = \langle u \rangle + \frac{\left\langle \tilde{u}\tilde{C} \right\rangle}{\langle C \rangle} \tag{4.9}$$

The effective transport velocity averaged over the near-bed region for the mixed and base cases is shown in Figure 4.6a and 4.6c, respectively. A clear difference in magnitude is observed between these two cases, with u_e for the Base case being at least an order of magnitude greater than that obtained for the unstratified scenario. Since suspended sediment concentrations are of similar magnitude in both scenarios (Figure 4.6b and Figure 4.6d), the difference in the magnitude of u_e is explained by the differences in the cross-shore flow. Under well-mixed conditions, the Kelvin wave velocities are not modified and the flow is predominantly coast parallel, whereas in the presence of stratification ETS generates strong cross-shore currents (Figures 4.4d and 4.5a). Differences in direction of transport are also observed between these two cases; u_e is persistently directed seaward (positive) for the unstratified case whereas u_e is predominantly landward (negative) for the stratified case. For the stratified case, a transition from offshore to onshore transport is observed in water depths of approximately 15 m, which creates a region of transport convergence that is collocated with the landward limit of the turbidity maximum zone (Figure 4.6c, d). Towards the coast, a region of transport divergence (transition from onshore to offshore) explains the relatively lower suspended sediment concentrations observed in intermediate water depths (6-12 m).

Individual terms contributing to $\langle uC \rangle$ at two cross-shore locations (indicated by the vertical dashed lines in Figure 4.6b) are shown in Figure 4.6g,h. It is clear that the contributions from the residual current dominate the residual sediment flux at both locations, and, since the direction of these fluxes is opposite, it creates the convergence region where suspended sediments preferentially ac-

cumulate. The covariance flux $\left\langle \tilde{u}\tilde{C} \right\rangle$ generally opposes the fluxes driven by the residual current at both locations, and is relatively more important at the shallower location. Notable differences in magnitude exist between the stratified and well-mixed cases, as could be expected from the magnitudes observed for u_e (Figure 4.6a,c).

Mechanism of formation of the TMZ

To examine what is driving the net landward residual transport, Figure 4.7 shows the water column structure over two tidal cycles and subtidal profiles of salinity, eddy viscosity, suspended sediment concentrations, cross-shore velocities and cross-shore sediment fluxes at a cross-shore location in 17m of water (within the TMZ). In order to analyze the effects of ETS, these subtidal profiles have been averaged over the stratifying and de-stratifying phases of the tidal cycle, rather than over flood and ebb tides. The salinity structure shows that the water column is on average stratified at this site during both phases (Figure 4.7a,b), however, the bottom layer is well-mixed during the stratifying phase whereas some stratification is observed during the de-stratifying phase (Figure 4.7b). The near-bed stratification occurring on the de-stratifying phase acts to reduce turbulence and creates an asymmetry in the eddy viscosity profiles that results in higher values of the eddy viscosity during the stratifying phase (Figure 4.7d). The asymmetry in vertical mixing results in larger onshore directed cross-shore velocities near the bed, as shown in Figure 4.7h. As a result of the lower eddy viscosity values, considerable shear is observed in the near-bed cross-shore velocity during the de-stratifying phase of the tidal cycle, which is offshore directed (Figure 4.7h). The net result on a subtidal scale is a landward subtidal residual current near the bed.

Suspended sediments are confined to the lower layer (Figure 4.7e,f) and no significant differences in sediment concentration exist between the stratifying and de-stratifying phases. Thus, the landward subtidal sediment fluxes are predominantly driven by the asymmetries in the residual cross-shore velocity rather than by asymmetries in the suspended sediment concentrations.

The results presented in Figures 4.6 and 4.7 suggest that the subtidal landward sediment fluxes
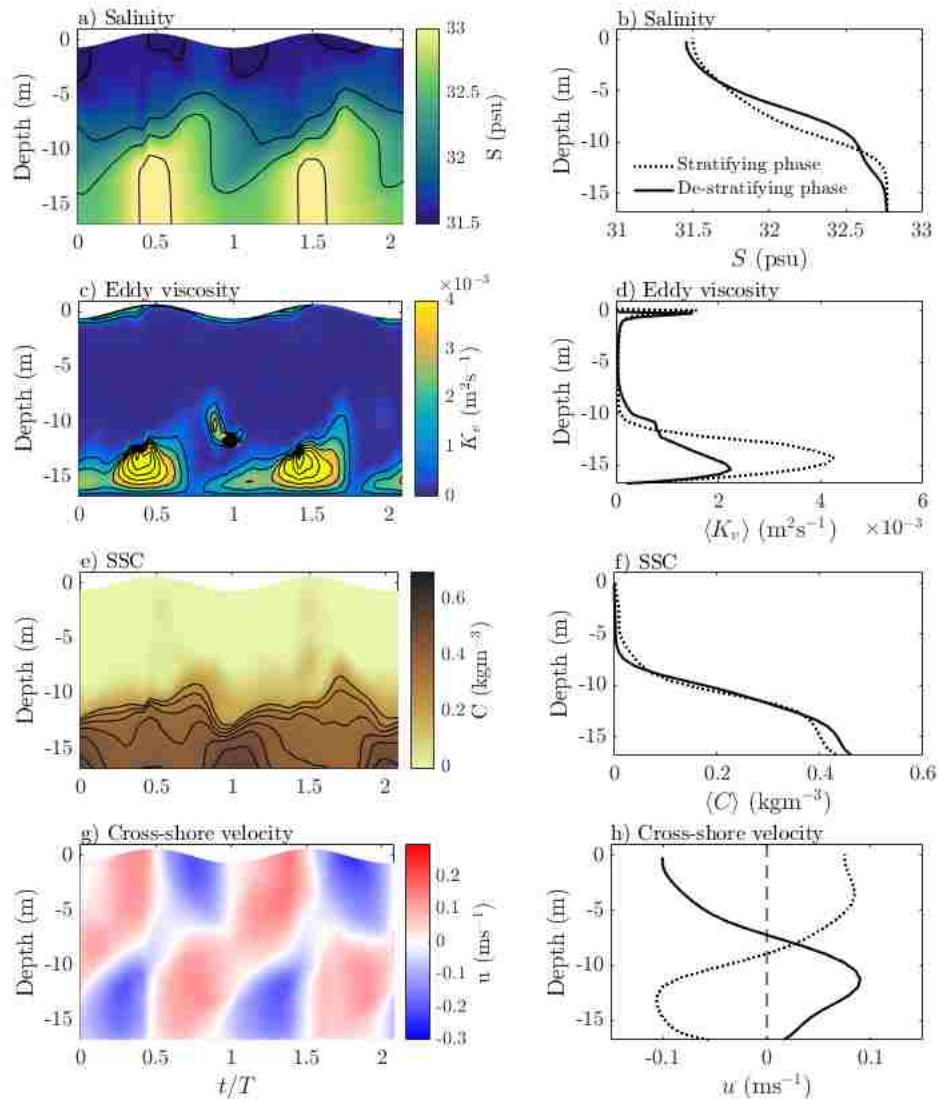
Figure 4.7: (a) Salinity structure. (b) Mean salinity profiles for the stratifying (dotted line) and de-stratifying phases of the tidal cycle. (c) Eddy viscosity. (d) Mean eddy viscosity profiles for the stratifying (dotted line) and de-stratifying phases of the tidal cycle. (e) Suspended sediment concentrations. (f) Suspended sediment concentrations profiles for the stratifying (dotted line) and de-stratifying phases of the tidal cycle. (g) Cross-shore velocity. (h) Cross-shore velocity profiles for the stratifying (dotted line) and de-stratifying phases of the tidal cycle.

are driven by asymmetries in vertical mixing near the bed that result from the stratification cycle created by the ETS dynamics. The cross-shore variability in vertical mixing asymmetry is shown in Figure 4.8, along with the structure of the subtidal cross-shore and alongshore transports. The asymmetry in eddy viscosity is obtained as $|\Delta K_v| = K_{v,s} - K_{v,d}$, where $K_{v,s}$ and $K_{v,d}$ correspond to the mean values of eddy viscosity over the stratifying and de-stratifying phases, respectively. We find that the structure of $|\Delta K_v|$ explains the structure of the subtidal cross-shore transport (Figure 4.8b) and the overall location of the TMZ. The largest values of $|\Delta K_v|$ occur in water depths between 12-20 m (Figure 4.8a), which coincides with regions of elevated landward near-bed transport (4.8b). The change in the direction of transport that is observed in water depths of approximately 15 m is collocated with the location where $|\Delta K_v|$ significantly increases in the offshore direction (Figure 4.7a,b), and, as shown in Figure 4.4b,c, it also coincides with the tidally-averaged position of the salinity (density) front. The strong correlation between $|K_v|$, the subtidal cross-shore transport and the location of the TMZ confirms that the TMZ is driven by the effects of mixing asymmetries on the residual velocity profiles. The alongshore subtidal transport (Figure 4.8c) shows fluxes that can be much higher than those in the cross-shore direction, particularly at intermediate water depths (10-15m). The alongshore shear is centered around the TMZ, and coincides with the region of highest $|\Delta K_v|$ (Figure 4.8a,c). The net residual transport within the TMZ is directed towards the north (positive).

Influence of the horizontal density gradient

The magnitude of the density gradient is expected to have a direct impact on the occurrence, magnitude and location of the TMZ. Figure 4.9 shows the effective transport velocity u_e and suspended sediment concentrations as a function of the initial horizontal density gradient for model Runs 1-9 (see Table 4.1). Results are shown in terms of a normalized cross-shore coordinate, x/W, where W corresponds to the initial width of the stratified region (20 km). Regions of transport convergence (transition from $u_e > 0$ to $u_e < 0$) are clearly identified in Figure 4.9a, and correlate well with regions of high suspended sediment concentrations (Figure 4.9b). These regions of transport convergence set the landward limit of the TMZ, which is clearly identified as a region of elevated sediment concentrations that is detached from the coast, and that is observed to occur for initial
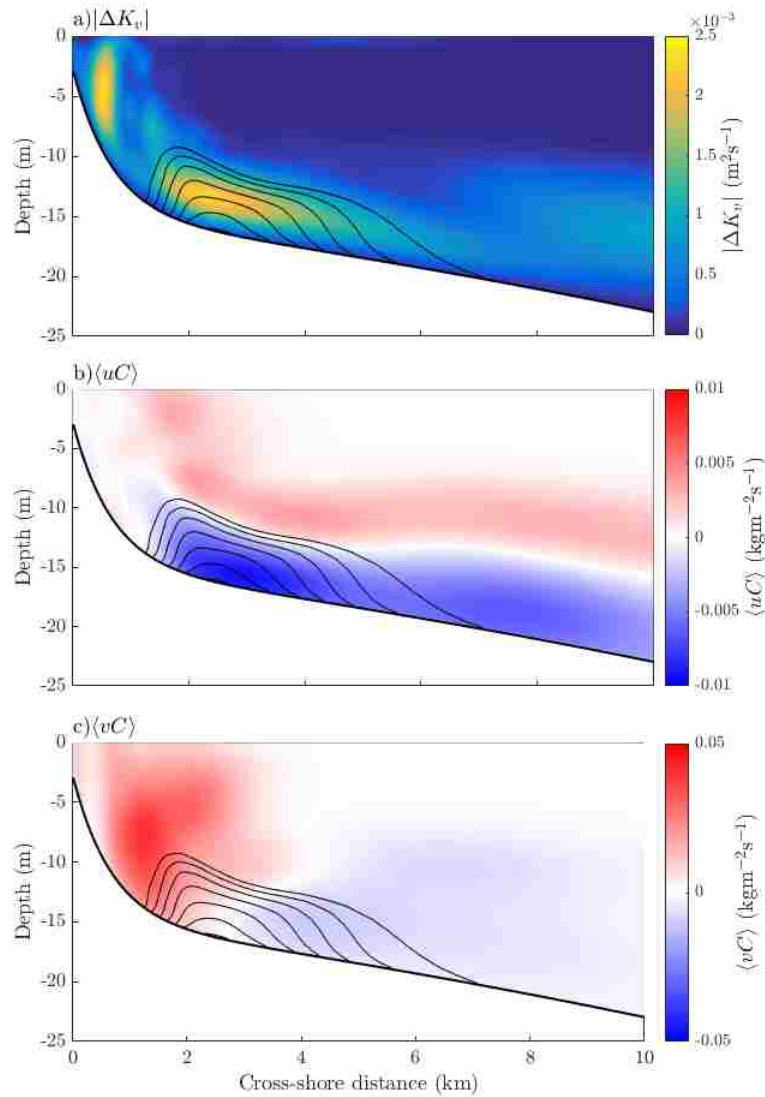
Figure 4.8: Cross-shore structure of the asymmetries in eddy viscosity. (b) Cross-shore residual sediment transport. Negative values correspond to onshore transport, positive values correspond to offshore transport. (c) Alongshore residual transport. Positive values correspond to northward transport and negative values correspond to southward transport. In all panels, the contour lines correspond to the suspended sediment concentrations within the TMZ.

density gradients greater than approximately 10^{-4} (kgm^{-4}). We find that the landward limit of the TMZ moves slightly onshore as the initial density gradient increases (Figure 4.9b), however, not much variation is observed for initial density gradients greater than 1.5×10^{-4} (kgm^{-4}).

The TMZ is always in regions with large values of the top-bottom ellipticity difference, which is indicated by the contour lines in Figure 4.9. Typically, the TMZ occurs in regions where $\Delta\varepsilon > 0.5$, which in turn are observed to occur for large values of the initial horizontal density gradient. It should be noted that high concentrations are also observed in shallow waters ($x/W < 0.1$), but these are not attributed to ETS since they occur in a well-mixed water column with $\Delta\varepsilon \sim 0$ (Figure 4.9b).

4.5   Discussion

4.5.1   Mechanism of formation of the TMZ

Figure 4.9 clearly shows that the occurrence of TMZ is linked to the occurrence of ETS, which manifests in terms of high values of tidal current ellipticity. The existence of stratification, but with no considerable elliptical tidal straining (low values of $\Delta\varepsilon$), does not result in the formation of a TMZ in intermediate water depths (Runs 3, 4, 28, 29). This was confirmed by model simulations in which tidal amplitude η_0 was significantly decreased (not shown). Reducing tidal amplitude leads to a decrease in tidal velocity amplitude, which in turn limits magnitude of the cross-shore velocities that lead to cross-shore straining. This suggests that the sole existence of a horizontal density gradient is not enough to generate a TMZ, and that moderate to high tidal flow velocities are needed in order to generate the convergence in transport.

In this study, we observe that the mechanism leading to residual onshore sediment fluxes in ROFI systems with progressive tides is remarkably similar to the tidal straining mechanism that leads to the formation of TMZ in estuaries (*Jay and Musiak*, 1994; *Scully and Friedrichs*, 2007). Although the final result is arguably the same, the phasing between what was observed in our simulations and observations in estuaries is different. In estuaries, more mixing near the bed is generated during the de-stratifying phase of the tidal cycle that occurs during flood tide (*Jay and Musiak*, 1994;
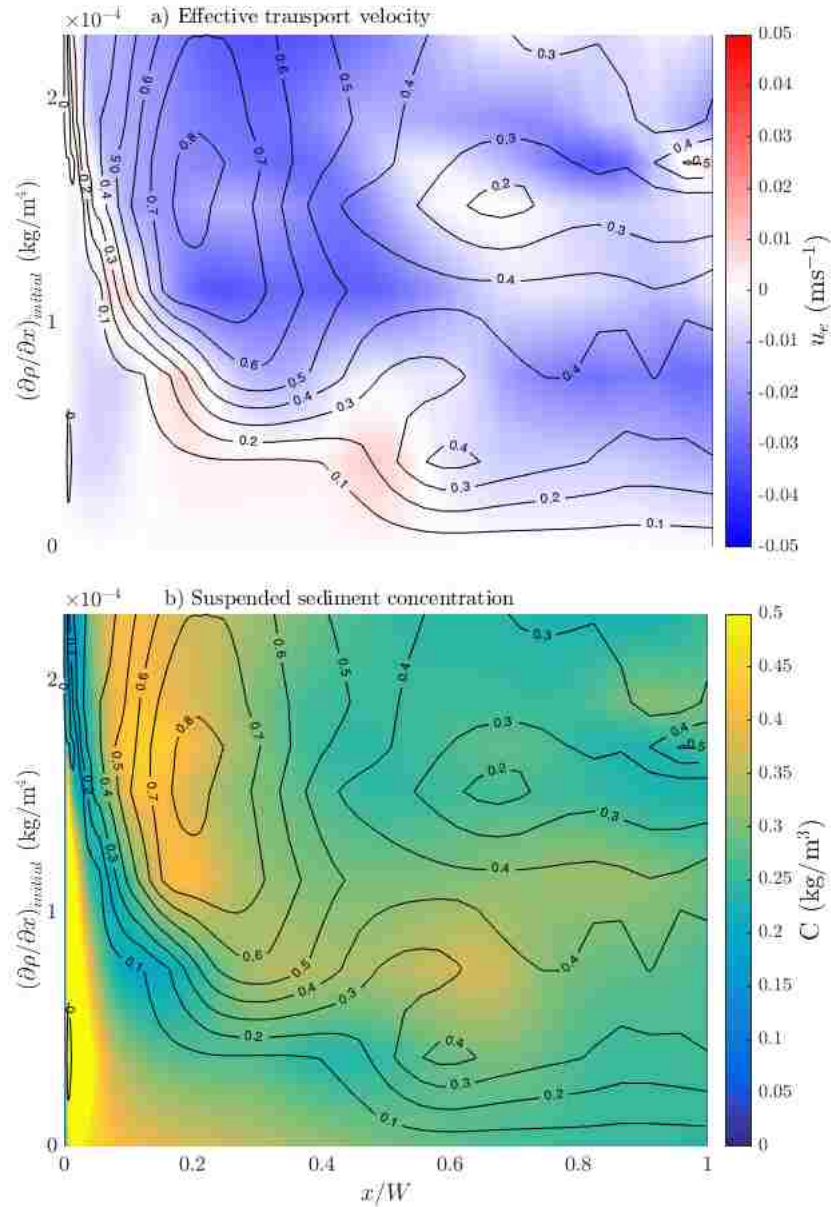
Figure 4.9: (a) Effective transport velocity. Contour lines represent top-bottom ellipticity difference, $\Delta\varepsilon$. (b) Vertically averaged suspended sediment concentrations over the bottom 1 m. Contour lines represent top-bottom ellipticity difference, $\Delta\varepsilon$.

Burchard et al., 2013). Here, ETS leads to enhanced mixing and a well-mixed region near the bed during the stratifying phase of the semi-diurnal cycle, which corresponds to the transition between low water and high water. These results are consistent with previous studies that investigated the effects of ETS on the cycle of turbulence and TKE dissipation in the Rhine system (*Fisher et al.*, 2002; *Souza et al.*, 2008; *Fischer et al.*, 2009). *Souza et al.* (2008) found that the effect of ETS is to create instability in the water column as the cross-shore shear forces denser higher salinity water over fresher water. They hypothesized that the potential energy released by the straining mechanism leads to convective motions and enhanced turbulence near the bed. In agreement with this, we find higher values for the eddy viscosity during the stratifying phase of the semi-diurnal cycle, in which near-bed velocities are directed onshore and thus force denser water over lighter water.

The influence of Earth's rotation is necessary for the occurrence of tidal straining in shallow coastal systems with progressive tides, as it sets the thickness of the cyclonic and anticyclonic boundary layers. In such systems, like the Rhine, Earth's rotation leads to the development of tidal straining in a direction that is perpendicular to the direction of the tidal flow and that of the buoyant coastal current, which flow parallel to the coast. As shown in Section 4.4.2, the fact that cross-shore straining occurs in these systems can lead to the formation of turbidity maximum zones over long stretches of coast (e.g. Figure 4.2). Coastal regions with progressive tidal waves can be frequently found at mid latitudes, for which $\delta_- >> \delta_+$, suggesting that ETS and coastal TMZs, such as the one observed in the Rhine (*van der Hout et al.*, 2015), may occur in other river plume systems. For example, progressive tidal waves are observed in the East China Sea (*Wu et al.*, 2014), along the Scottish and English coast in the North Sea (*Huthnance*, 1991).

4.5.2   Influence of particle size and Rouse number

The occurrence of turbidity maximum zones is conditioned to the particle size distribution of bed sediments, as large particles cannot be maintained in suspension high above the bed by the tidal stresses and turbulence. Here, we have restricted model simulations to very fine particles by providing a 20% bed concentration of medium to fine silts with small settling velocities ($\sim 0.1 - 1$ mms^{-1}) to guarantee that sediment particles are able to stay in suspension for long periods of time

and be transported as suspended load.

The cross-shore distributions of suspended sediment concentrations for different Rouse numbers (Runs 18-22, settling velocities specified in Table 4.1) are shown in Figure 4.10. The Rouse number has been computed using the settling velocity of the fine sediment fraction, which is assumed to predominantly form the TMZ. In order to better appreciate the variations of the suspended sediment concentrations, the suspended sediment concentrations have been normalized by the maximum observed concentrations, which typically occur in very shallow regions ($x/W < 0.05$). The distributions of suspended sediment concentrations show that a coastal TMZ, identified as the second peak in the cross-shore distribution of suspended sediment concentrations (around $x/W \sim 0.1$), exists for all Rouse numbers, albeit the maximum concentrations are certainly different. As discussed earlier, the first peak in the distribution of suspended sediment concentration occurs in very shallow waters and does not result from ETS dynamics. We observe that the suspended sediment concentrations decrease as the Rouse number (or settling velocity) increases, which is to be expected as the amount of energy that sets the magnitude of the bottom stresses was kept fixed in these simulations, via the tidal forcing. Peak suspended sediment concentrations in the TMZ range from $C_{max} = 0.03$ (kgm^{-3}) to $C_{max} = 0.63$ (kgm^{-3}), which correspond to the maximum and minimum Rouse numbers, respectively. Figure 4.10 shows that as the Rouse number increases, the cross-shore extension of the TMZ becomes narrower, and the TMZ exhibits peak concentrations that are not much greater than the background concentrations.

Since the hydrodynamics of the simulations shown in Figure 4.10 were kept the same, we conclude that the characteristics of the TMZ rely heavily on the particle size distribution of bed sediments. Here we have considerably simplified the sediment dynamics by including only one class of fine sediments in the numerical simulations. We recognize that including particle size distributions may result in different cross-shore distributions of suspended sediment concentrations, as the magnitude of the residual and covariance sediment fluxes are affected by particle size (*Schulz and Umlauf*, 2016; *Burchard et al.*, 2013). For the simulations carried out in this study, we observe that the subtidal sediment flux is always dominated by the tidal residual component, independent of the settling velocity of bed sediments (not shown). However, the covariance fluxes do become more
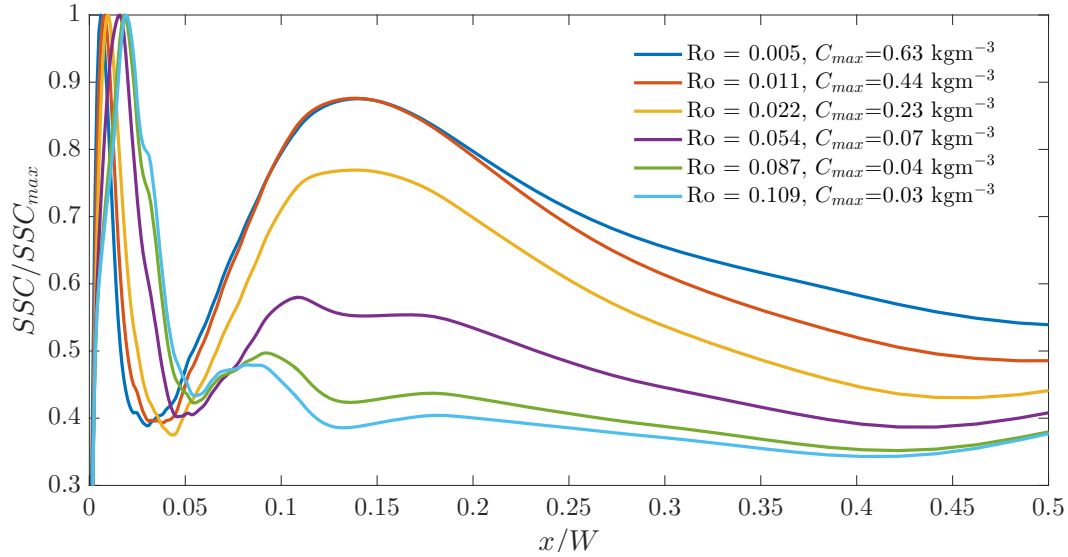
Figure 4.10: Normalized suspended sediment concentrations as a function of the Rouse number. Values of the Rouse numbers and maximum concentrations observed in the TMZ are given in the legend.

important as settling velocity increases, particularly in the near-bed region. Despite this, we do not expect that including more complex particle size distributions would affect the conclusions obtained with respect to the mechanisms of formation of the TMZ.

4.5.3   The parameter space of ETS and the TMZ

The occurrence of a coastal TMZ and ETS is analyzed in terms of the non-dimensional parameters described in Section 4.2, the Simpson number (or horizontal Richardson number), Si, the anticyclonic Stokes number, Stk_-, and the top-bottom ellipticity difference, $\Delta\varepsilon$. Based on the definitions of Si and Stk_- (Equations 4.1 and 4.4), we can write

$$SiStk_-^2 = -\frac{g}{\rho}\frac{\partial\rho}{\partial x}\frac{C_0^2}{(\omega - f)^2} \tag{4.10}$$

Assuming that the constant C_0 is known, or that it can be determined from previous studies (*Soulsby*, 1983; *Souza*, 2013), Equation 4.10 is only a function of the horizontal density gradient

and the Coriolis parameter. We will find that this expression provides suitable combinations of horizontal density gradient and Coriolis parameter for which ETS and a TMZ could be expected to occur.

Figure 4.11 shows where our model simulations fall in the (Stk_-, Si) parameter space. Both Si and Stk_- have been computed using a mean depth value given by $\overline{H}$ (Equation 4.7). Velocity scales have been provided in terms of the tidal Kelvin wave, at a cross-shore location corresponding to $\overline{H}$. As the Kelvin wave velocity decays slowly in the cross-shore direction, results are not sensitive to the exact location of $\overline{H}$. As discussed earlier, ETS in ROFI systems with progressive tides, such as the Rhine, is generated by the counter-rotating surface and bottom currents which result in the semi-diurnal straining of the density field. Therefore, the occurrence of ETS is determined in terms of $\Delta\varepsilon$, by requiring that $\Delta\varepsilon \geq 0.5$. In general, $\Delta\varepsilon \geq 0.5$ would indicate a significant degree of decoupling between the upper and lower layers (*Visser et al.*, 1994) and guarantees the development of tidal currents with strong cross-shore current component (about 20% of the dominant alongshore currents).

The contour lines in Figure 4.11 correspond to constant values of $SiStk_-^2$. With the exception of one run, model runs for which $\Delta\varepsilon \geq 0.5$ (shown as circles) are located above the $SiStk_-^2 = 6$ contour line, suggesting that a limiting condition for the occurrence elliptical of tidal straining in progressive tide ROFI systems can be taken as $SiStk_-^2 = 6$. We observe that, in general, ETS occurred at Simpson numbers greater than $Si > 0.5$ and anticyclonic Stokes numbers greater than $Stk_- > 2$.

The occurrence of a turbidity maximum region is linked to the occurrence of ETS ($\Delta\varepsilon \geq 0.5$), as indicated by the colorbar in Figure 4.11. This is also in line with the results shown in Figure 4.9, where the TMZ was only observed in regions of high $\Delta\varepsilon$. The peak suspended sediment concentrations in the TMZs are variable and typically range from 0.2-0.4 (kgm^{-3}), and while there is no apparent correlation between the observed peak concentrations and Si or Stk_-, it is clear that a TMZ generally occurs for runs with $SiStk_-^2 \geq 3$. Model runs with no TMZ were assigned zero suspended sediment concentration (blue), even though concentrations can also be high (as shown
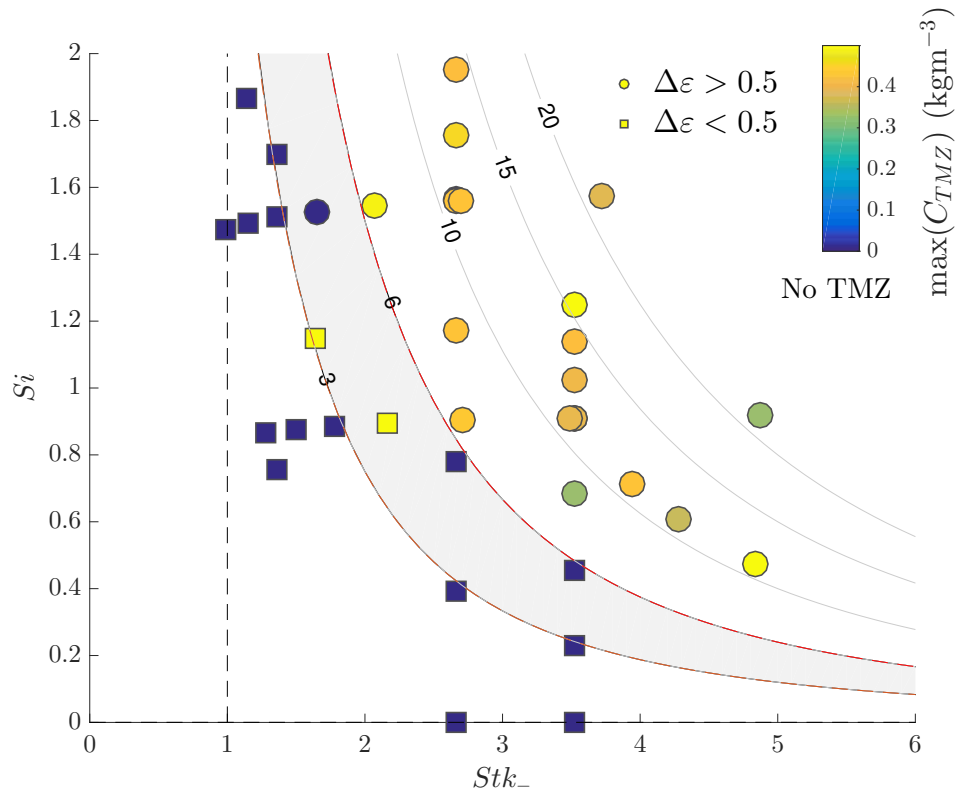
Figure 4.11: Parameter space for ETS and turbidity maximum zones in coastal seas. Circles indicate model runs where $\Delta\varepsilon > 0.5$, whereas squares indicate model runs where $\Delta\varepsilon < 0.5$. The colorbar indicates the peak concentration observed in the TMZ. Zero concentration (dark blue) was assigned to runs where a TMZ was not observed. Contours indicate constant values of $SiStk_-^2$. The area between contours $SiStk_-^2 = 3$ and $SiStk_-^2 = 6$ (red dashed lines) has been filled to indicate a transitional band. Vertical dashed line indicates $Stk_- = 1$, which is required for the decoupling of the top and bottom layers due to stratification

.

in Figure 4.9b).

Combining what is observed in Figure 4.11 for the occurrence of ETS and the TMZ, the region $3 \leq SiStk^2 \leq 6$ can be interpreted as a transitional band; for $SiStk^2 < 3$ neither ETS or a TMZ occur whereas for $SiStk^2 > 6$ they always occur in our simulations. Taking $SiStk_-^2 = \alpha$, with α in the range of 3 to 6, we can rewrite Equation 4.10 as,

$$N_x^2 \geq \alpha \frac{(\omega - f)^2}{C_0^2} \tag{4.11}$$

where $N_x^2 = -(g/\rho_0)\partial\rho/\partial x$. Equation 4.11 predicts the minimum value of the horizontal density gradient that would be required at a specific latitude for the occurrence of ETS. Figure 4.12 shows the limiting curve given by Equation 4.11. For example, for a typical cross-shore density gradient of 1.5×10^{-4} (kgm^{-4}), the minimum latitude at which ETS could be expected to occur is approximately $37°$. Alternatively, at a latitude of $25°$, Equation 4.11 indicates that a cross-shore density gradient of approximately 5×10^{-4} (kgm^{-4}) would be required for ETS to occur. This value is far too large for conditions typically observed in buoyant coastal currents, and suggests that ETS will not occur at low latitudes given realistic values for the horizontal density gradient. We note that the use of Equation 4.11 is limited to shallow regions ($h \sim 20 - 30$ m) where the tide behaves as a progressive wave.

Overall, we find that the parameter space given by Si and Stk_- provides a simple approach to evaluate whether ETS could occur in shallow coastal regions for a given combination of density gradient, tidal velocity, depth and latitude.

4.6 Conclusions

This chapter was motivated by field observations of a persistent offshore turbidity maximum zone that extends for tens of kilometers along the coast in the Rhine ROFI system (*Van Alphen*, 1990; *Joordens et al.*, 2001; *van der Hout et al.*, 2015). The aim of this study was to answer the following questions: Can ETS lead to the formation of an offshore TMZ? And what are the mechanisms that lead to cross-shore sediment convergence?
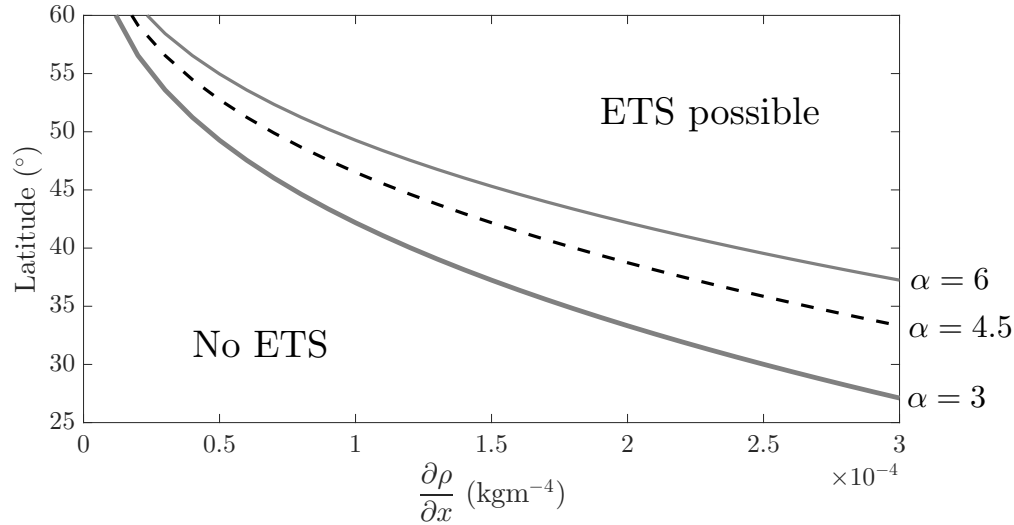
Figure 4.12: relationship between the horizontal density gradient and latitude, given by Equation 4.11.

The major result of this idealized numerical modeling study is that ETS can indeed lead to the formation of offshore turbidity maximum zones in ROFI systems with progressive tides. Our model simulations reproduced the main dynamical features that are observed in the far field of the Rhine ROFI, which include the semi-diurnal variations in stratification and the modification of the tidal ellipses (*Visser et al.*, 1994; *Simpson and Souza*, 1995; *De Boer et al.*, 2006; *Souza et al.*, 2008). The location and extension of the TMZ we observe in the numerical simulations were shown to match well with field observations (*van der Hout et al.*, 2015, 2017).

The mechanism that leads to cross-shore convergence in the subtidal near-bed sediment fluxes is driven by asymmetries in eddy viscosity that result from ETS dynamics. On a subtidal time scale, the asymmetries in vertical mixing lead to landward cross-shore velocities in the near-bed region and landward subtidal sediment fluxes in water depths greater than approximately 12-15 m. The mechanism leading to landward residual sediment fluxes was found to be similar to the tidal strain-ing mechanism that is observed to contribute to the formation of turbidity maximum zones in

estuaries (*Jay and Musiak*, 1994; *Geyer et al.*, 2001). The cross-shore structure of the asymmetries in vertical mixing was found to explain the magnitude and direction of subtidal sediment fluxes, and, by extension, the position of the TMZ and the magnitude of the observed suspended sediment concentrations.

The location and extension of the TMZ, and magnitude of the suspended sediment concentrations strongly depend on the Rouse number, in terms of the settling velocity. As the settling velocity depends primarily on particle size, the dynamics of the TMZ and its generation are expected to vary according to the particle size distribution of fine bed sediments. The formation a TMZ was observed for settling velocities as high as 0.8-1 mms^{-1} (silts), although its magnitude and relative importance with respect to concentrations in shallow water decreased with increasing settling velocity.

The Simpson and the Stokes numbers, in combination with the top-bottom tidal current ellipticity difference, were shown to provide a parameter space that successfully mapped the occurrence of ETS and a coastal TMZ in our simulations. In general, we observed that ETS only occurred at values of $Si > 0.5$ and $Stk_- > 2$. The information needed to estimate the Simpson and the anticyclonic Stokes numbers is frequently available from field observations (Equations 4.1 and 4.4), such that the parameter space provided by Figures 4.11 and Figures 4.12 can be readily used to evaluate whether ETS can occur over a specific coastal region. Evaluation of limiting cases in terms of the required horizontal density gradients and latitudes suggests that ETS will not occur at low latitudes (less than 25°). It should be noted, however, that this study is limited to coastal seas with shallow bathymetries in which the variations in the cross-shore density gradients are the dominant dynamical feature. Nonetheless, these results can be relevant for several regions with progressive tides in mid-latitudes, and may encourage future research regarding the occurrence of coastal TMZs in regions of freshwater influence.

Finally, the ETS mechanism reproduced here is just one of the potential mechanisms that can contribute to the formation of a coastal TMZ. Cross-shore transport near the bed regions may also result from a wide variety of physical processes, such as wave-driven diffusion, wind-induced

downwelling or upwelling (*Lentz and Fewings*, 2012), Stokes drift (*Lentz and Fewings*, 2012) or gravity-driven sediment flows during extreme weather conditions (*Flores et al.*, 2018; *Traykovski et al.*, 2007). It is very likely that all these mechanisms (and others) contribute to the maintenance of the TMZ over long timescales.

Chapter 5

THE INFLUENCE OF NON-EQUILIBRIUM BEDFORMS ON BED STRESSES AND SEDIMENT RESUSPENSION IN THE PRESENCE OF STRONG WAVE AND CURRENT FORCING

5.1 Introduction

Suspended particulate matter dynamics are of interest for a variety of ecological problems in coastal ocean environments. For example, the transport of fine sediments is related to the fate of contaminants and water quality issues, as well as the inhibition of primary production and hypoxia (*Yoshiyama and Sharp*, 2006). Engineering practices are also often conditioned to the natural pathways of suspended sediments, as they can impair the optimal functioning of coastal projects. Human intervention, such as dredging or beach nourishment, may lead to enhanced suspended sediment concentrations and undesirable effects on the functioning of harbors and navigation channels (*Winterwerp et al.*, 2013). Thus, a better understanding of the physical processes that determine sediment pathways and accumulation zones is essential to improve our capability of sustainably manage coastal areas.

The transport of fine sediment involves resuspension, advection, dispersion and deposition processes. Sediment resuspension transfers sediment particles from the seabed into the water column, where they are advected by the dominant currents and diffused into the upper water column by the flow turbulence. When turbulence is weak, sediment particles slowly settle and are eventually deposited back onto the bed surface. The amount of sediment that gets entrained into the water column depends on the shear stress acting on the bed, which results from the interaction between the seabed itself and the overlying flow field, and on the bed sediment properties, such as grain size and cohesiveness (*Sanford and Maa*, 2001; *Van Prooijen and Winterwerp*, 2010). More specifically, sediment will be entrained into the water column when the bed stress exceeds a critical (threshold) stress for erosion. The erosion of cohesive sediments (silts and clays, with $d < 64\ \mu$m) is commonly parametrized as (*Partheniades*, 1965; *Sanford and Maa*, 2001; *Van Prooijen and Winterwerp*, 2010)

$$E = M \left(\tau_b - \tau_{cr}\right)^k \tag{5.1}$$

where M and k are empirical constants, τ_b is the bottom shear stress and τ_{cr} is the critical stress. M, k and τ_{cr} can vary widely between sites as they depend on sediment material properties such as grain size and porosity (*Sanford and Maa*, 2001; *Grabowski et al.*, 2011; *Brand et al.*, 2015). Typically, researchers have opted for the use of linear relationship by setting $k = 1$ (*Sanford and Maa*, 2001).

Estimation of the bed stresses that lead to sediment resuspension under current-dominated conditions is a relatively simple task; if near-bed turbulence measurements are available, the inertial dissipation or the eddy correlation methods can be readily used (*Kim et al.*, 2000). The well-known law of the wall can also be applied (e.g *Kim et al.*, 2000; *Lacy et al.*, 2005)under current-dominated conditions if the near-bed velocity profile was measured, or a quadratic drag law can be used if only a point velocity measurement is available (e.g. *Rippeth et al.*, 2002). Under the simultaneous presence of waves and currents, bottom stress results from the non-linear combination of wave and current effects. The enhanced turbulence within the wave boundary layer increases the effective roughness that the current feels, increasing the drag and retarding the overlying currents (*Grant and Madsen*, 1979). Measuring bed shear stress under wave-and-current forcing is a much more difficult task since measurements need to be taken within the wave-boundary layer, which is only a few centimeters thick. As a result, several models for predicting bed shear stress in the wave-current boundary layer have been developed throughout the years. In these models, bottom stress is usually estimated in terms of bulk wave parameters (height, period, direction), near-bottom current measurements and estimates of bed roughness (*Grant and Madsen*, 1979; *Wiberg et al.*, 1994; *Soulsby et al.*, 1993; *Styles and Glenn*, 2000).

An accurate estimation of bottom stresses is extremely relevant both in field and modeling studies, since they exert a first order influence on sediment transport processes (e.g., Equation 5.1). Among all parameters involved in the computation of the bed stresses, bed roughness is often the most challenging to estimate (*Lacy et al.*, 2005; *Scully et al.*, 2018). Sandy seabeds in shelf seas are

often covered with small scale bedforms (ripples) that result form the action of waves, currents or a combination of both (*Li and Amos*, 1998; *Soulsby et al.*, 2012). These bedforms increase the drag that the seafloor exerts on the overlying flow (*Scully et al.*, 2018; *Drake and Cacchione*, 1992; *Drake et al.*, 1992), and thus have to be accounted for when estimating the bed stresses. Bedforms have also been shown to increase wave dissipation (*Ardhuin et al.*, 2003) and influence the vertical distribution of suspended sediments (*Gutierrez et al.*, 2005; *Li et al.*, 1996). Bed stresses, near-bed turbulence and mean flows in turn affect the characteristics and evolution of the bedforms, such that sediment transport processes are determined by a feedback loop between the hydrodynamics, bedforms and sediment properties (*Soulsby*, 1997).

Bedform roughness is usually incorporated into models as a function of the geometric properties of the bedforms, i.e., bedform height (η) and wavelength (λ), in the form of $k_b = \alpha \eta^2/\lambda$, where α is a constant (*Grant and Madsen*, 1982; *Nielsen*, 1992; *Soulsby*, 1997). Bedform dimensions can be measured in the field with the use of acoustic instrumentation, such as rotary sonars or acoustic ripple profilers (*Thorne and Hanes*, 2002; *Traykovski*, 2007; *Bolaños et al.*, 2012; *Scully et al.*, 2018). Data from these instruments can be processed to extract bedform height, wavelengths and orientation with good spatial and temporal resolution (*Traykovski et al.*, 1999; *Bolaños et al.*, 2012; *Scully et al.*, 2018). However, these type of instruments may not be available for field studies and in this case bedform geometry is estimated indirectly. Numerous formulations have been proposed to predict η and λ, most of which are based on bulk wave parameters (*Nielsen*, 1981; *Wiberg and Harris*, 1994; *Styles and Glenn*, 2002; *Pedocchi and Garcia*, 2009) and developed both in laboratory setting and in the field. These formulations are often site specific, and there is large dispersion in terms of model skill such that there is no widely accepted universal formulation (*Nelson et al.*, 2013).

Most small-scale bedform predictors assume that the bedforms are in equilibrium with the forcing conditions, which is only true if enough time has lapsed for bedforms to adjust to the hydrodynamic forcing (*Nelson et al.*, 2013). If that is not the case, bedforms will actively change their dimensions and if the forcing conditions change continuously, the transient character of the bedforms will persist in time (*Davis et al.*, 2004; *Nelson and Voulgaris*, 2014). Both laboratory and field experiments have found that the adjustment time of bedforms can be longer than the time over

which the forcing changes (*O'Donoghue and Clubb*, 2001; *Traykovski*, 2007). Bedforms can also be washed out if the forcing is too strong, or, under weak forcing, they can remain unchanged as no sediment transport can be sustained (*Soulsby et al.*, 2012). None of these features is accounted for in equilibrium bedform parameterizations.

In order to accurately reproduce the drag exerted by the seabed on the overlying flow, bed roughness needs to be properly quantified in bottom boundary layer models (*Scully et al.*, 2018). While equilibrium bedform dimension predictors have been incorporated into wave-current boundary layer models to account for bottom roughness (*Scully et al.*, 2018; *Lacy et al.*, 2005; *Bolaños et al.*, 2012), results largely depend on the degree to which these predictors can reproduce bedform dimensions. Non-equilibrium ripple dynamics can result in large spatio-temporal variation in the drag coefficient (*Scully et al.*, 2018) and therefore need to be incorporated into the modeling of bed shear stresses. Time-dependent ripple models that account for the non-equilibrium evolution of ripples have been proposed (*Traykovski*, 2007; *Soulsby et al.*, 2012; *Nelson and Voulgaris*, 2015). *Soulsby et al.* (2012) proposed a fully time-evolving model that predicts the height, wavelength and orientation of bedforms on sandy seabeds generated by currents, waves or both, that includes processes dealing with the threshold of motion, bedform wash-out and biological degradation. It is of interest, and one of the main objectives of this study, to evaluate the results of incorporating time-dependent ripple dynamics in the estimation of bed shear stresses.

For the particular case of the Dutch coast, *Meirelles et al.* (2016) analyzed bedform data from an Acoustic Ripple profiler deployed in 12m depth during the STRAINS field campaign in the fall of 2014. They found that current ripples dominated the small scale bedform dynamics throughout most of the deployment, whereas wave ripples were found to dominate during storm periods, which occurred sporadically. *Meirelles et al.* (2016) classified the ripples in terms of visual inspection (*Amos et al.*, 1988) and in terms of a dimensionless mobility number (*Amos and Collins*, 1978), suggesting that the latter performs poorly when the bedforms are not in equilibrium with the hydrodynamic forcing. This further emphasizes the need to account for non-equilibrium ripple dynamics in environments where both waves and currents are equally important, such as the Dutch coast.

The challenges in the estimation of near-bed sediment transport processes go much further than the accurate estimation of bedform dimensions and bed stresses. Measuring sediment resuspension or erosion rates in the field is a difficult task, due to the high-frequency of the dynamics involved and because it requires measurements at the water-sediment interface. However, inferences can be made from near-bottom turbulence measurements (*Davidson et al.*, 1993; *Brand et al.*, 2010, 2015). The one-dimensional equation for vertical sediment diffusion in the water column can be written in terms of the divergence of the turbulent sediment flux and the gravitational settling flux,

$$\frac{\partial C}{\partial t} = -\frac{\partial}{\partial z}\left(\overline{w'c'}\right) - w_s \frac{\partial C}{\partial z} \qquad (5.2)$$

where C is suspended sediment concentration, w' and c' are the turbulent fluctuations in vertical velocity and sediment concentration, respectively, and w_s is the sediment settling velocity. Advection terms have not been considered in Equation 5.2, as is frequently the case in field studies (*Fugate and Friedrichs*, 2002; *Brand et al.*, 2010). When measured close to the bottom and provided lateral processes are of second importance, the vertical turbulent sediment flux $\overline{w'c'}$ can be interpreted as the resuspension flux (*Davidson et al.*, 1993; *Brand et al.*, 2010, 2015; *Scheu et al.*, 2015) as it represents the upward flux of suspended matter induced by turbulence, and responds directly to processes like loosening, consolidation and erosion limitation by a depth-dependent critical stress or changes in bed composition. Turbulent sediment fluxes can be measured directly with ADVs by properly calibrating acoustic backscatter to suspended sediment concentrations (*Fugate and Friedrichs*, 2002; *Brand et al.*, 2010). The occurrence of resuspension events as inferred from $\overline{w'c'}$ can be verified by comparing the critical shear stress with the bed stresses, and also by checking sediment concentration profiles and bed level measurements, if available.

In this chapter, we use field data to investigate bottom boundary layer sediment dynamics in a shallow, sandy inner shelf region (12m water depth) that is subjected to strong current and wave forcing. We present simultaneous measurements of near-bed Reynolds stresses, wave and current velocities, bedform geometry, suspended sediment concentrations and turbulent sediment fluxes with the goal of i) incorporating non-equilibrium bedform dynamics in the estimation of bed shear stresses and ii) using measurements of near-bed turbulent vertical fluxes to obtain field estimates

of the M and τ_{cr} parameters.

5.2   Methods

5.2.1   Instrumentation and data

The Stratification Impacts on Nearshore Sediment transport (STRAINS) experiment made hydro-dynamic and sediment transport measurements in the Rhine region of freshwater influence along the Dutch coast in 2013 and 2014. Near-bottom dynamics, turbulence and bed characteristics were measured using a benthic frame deployed in 12 m of water. Three-dimensional flow velocities were measured using three synchronized 6 MHz Sontek Acoustic Doppler Velocimeters (ADVs), sampling at 16 Hz and located at 0.25, 0.5 and 0.75 m above the bottom. The ADVs were mounted on an arm away from the frame to avoid turbulent perturbations due to the frame itself. The ADVs recorded 10-min bursts every 15 minutes, for a total of 2990 data bursts. Fast-sampling OBSs and microCT were deployed to measure near-bottom concentrations of suspended sediments and conductivity, respectively. These instruments sampled at 16 Hz and were collocated and synchronized with the ADVs to obtain turbulent fluxes of sediment and buoyancy.

The bedform data used here were processed and first published by *Meirelles et al.* (2016). We thank Saulo Meirelles from the Delft University of Technology for kindly providing these data. These data correspond to hourly three-dimensional seabed images that were acquired by an Acoustic Ripple Profiler (ARP), that provided bed elevation over a circular area of approximately 12 m^2, operating at 1.1 MHz. The echo intensity recorded by the ARP was converted into bed elevation, interpolated to a regular Cartesian grid, detrended and corrected for tilt variations of the benthic frame. The final seafloor image resolution was 1.95 cm per pixel, which provides the lower limit of the horizontal features that can be detected. Ripple parameters are extracted from the seafloor images using discrete 2D Fourier analysis, following the procedure outlined in *Perron et al.* (2008).

Bed material cores were taken on deployment day at different water depths, while in transit from the 18 m isobath to the 12 m deployment site. Samples were taken from the cores and sized using a Malvern size analyzer to obtain particle size distribution. All sites showed a mixture of fine sands

www.manaraa.com

and silts, and very small proportions of clay-sized material. A substantial increase in coarseness was not observed between the 18m and the 12m site, even though medium-to-coarse sands were observed at the 12 m site in small proportions (5-10 %). Median particle size at the 12 m site was $d_{50} = 200$ μm, with a fraction of silts and sands of approximately 20% and 80%, respectively.

5.2.2 Near-bottom currents, Reynolds stresses and turbulent sediment fluxes

The raw ADV data were quality controlled and de-spiked using the three-dimensional phase space algorithm of *Goring and Nikora* (2002). Near-bottom mean tidal velocities were estimated by time averaging over a 10-min period, and turbulent velocity components u', v' and w' were obtained by removing the tidal trend. The mean and the turbulent N-E horizontal velocity components were rotated to alongshore and cross-shore components, using the inclination of the major axis of the tidal ellipses which resulted in a rotation angle of 42.5 degrees from the North. Alongshore velocities are positive towards the northeast and cross-shore velocities are positive in the offshore direction. The harmonic analysis done to obtain tidal ellipses was performed using the T-TIDE code (*Pawlowicz et al.*, 2002).

The shallowness of the field site and the presence of high waves during storms required the use of a wave-turbulence separation method to obtain reliable estimates of the Reynolds stresses and fluxes, since wave motions were likely to penetrate all the way to the seabed. To reduce the wave-induced bias on the Reynolds stresses we used the linear filtration technique proposed by *Shaw and Trowbridge* (2001), which relies on the identification of coherent motions between two independent sensors. The sensors have to be separated by a vertical distance larger than the length scale of the turbulent eddies (which scale with the vertical distance from the bottom) but smaller than the correlation scale of wave motion. Here, we have used a vertical separation between instruments of $\Delta z = 0.5$ m using our lowest and highest ADVs. The measured and wave-filtered Reynolds stresses are used to assess the quality of our combined wave-current bottom stress estimates, by comparing the modeled and measured current friction velocities, u_{*c}.

Vertical turbulent sediment fluxes were estimated using the eddy correlation method (*Kim et al.*,

2000; *Brand et al.*, 2010, 2015). Typically, both c' and w' are determined from high frequency ADV measurements, where ADV backscatter is properly calibrated to yield suspended sediment concentrations (*Voulgaris and Meyers*, 2004; *Fugate and Friedrichs*, 2002). *Fugate and Friedrichs* (2002) showed the validity of this approach for cohesive sediments in an estuarine environment. Alternatively, we compute the turbulent sediment fluxes using a combination of collocated fast-sampling ADVs and OBSs. Since OBSs are more sensitive to the smaller particle sizes (*Lynch et al.*, 1997), our estimates of turbulent fluxes are more representative of the fine sediment dynamics. Estimations of turbulent fluxes are obtained at the three vertical levels 0.25mab, 0.5mab and 0.75mab.

5.2.3   Wave parameters

Representative wave parameters at our 12 m site were computed using the high-frequency ADV velocity measurements. Representative bottom orbital velocity (u_{br}) and the representative wave frequency associated with u_{br} were obtained from the frequency spectra of horizontal velocities, following *Madsen* (1995) and *Wiberg and Sherwood* (2008) as

$$u_{br} = \sqrt{2 \int (S_{uu} + S_{vv})\, df} \tag{5.3}$$

$$f_{br} = \frac{\int f S_{uu} df}{\int S_{uu} df} \tag{5.4}$$

where S_{uu} and S_{vv} are the spectra of horizontal velocities u and v. The spectra was calculated after performing the wave-turbulence separation method, thus avoiding inclusion of turbulence energy into the calculations of wave parameters.

5.2.4   Bedform geometry prediction

Because of their importance to bottom boundary layer dynamics and sediment transport processes, a vast number of studies aiming to predict ripple dimensions have been conducted over the years both in laboratory and field conditions. *Nelson et al.* (2013) presents a detailed review of 13 of such ripple predictors. Ripple predictors are commonly based on non-dimensional numbers, such

as the Mobility number (*Nielsen*, 1981; *Van Rijn et al.*, 1993) or the Shields parameter (*Grant and Madsen*, 1982), but also on wave and sediment parameters (*Wiberg and Harris*, 1994; *Traykovski*, 2007; *Pedocchi and Garcia*, 2009).

Here we test 3 ripple predictors and compare predicted ripple heights and wavelengths against measured data. The predictors were chosen because they use different sets of parameters to estimate ripple dimensions. The *Wiberg and Harris* (1994) predictor (hereafter WH94) is based on the wave orbital excursion normalized by the median sediment particle size, d_0/D_{50}. The original WH94 formulation involves iteration, however, *Malarkey and Davies* (2003) presented a modification that facilitates its implementation,

$$\lambda_{orb} = 0.62 d_0 \tag{5.5}$$

$$\lambda_{ano} = 535 D_{50} \tag{5.6}$$

$$\lambda_{sub} = 535 D_{50} \exp\left[-\frac{\log\left(\lambda_{orb}/\lambda_{ano}\right)\log(0.01 d_0)}{\log(5)}\right] \tag{5.7}$$

$$\eta = \frac{d_0}{\exp\left[B_2 - \sqrt{B_3 - B_1 \log\left(\frac{d_0}{\lambda}\right)}\right]} \tag{5.8}$$

where $B_1 = 10.526$, $B_2 = 7.59$ and $B_3 = 33.6$. Wavelength subscripts indicate orbital, anorbital and suborbital ripples. The limits for orbital, suborbital and anorbital ripples are given by $d_0/D_{50} < 1754$, $1754 < d_0/D_{50} < 5587$ and $d_0/D_{50} > 5587$, respectively.

Grant and Madsen (1982) (hereafter GM82) proposed a parameterization based on the Shields parameter,

$$\theta_w = \frac{\tau_w}{(s-1)g D_{50}} \tag{5.9}$$

where τ_w is the wave-induced shear stress. Their predictor gives increasing wavelengths for increasing Shields parameter up to a limiting value, given by

$$\theta_B = 1.8 \theta_{cr} \left(\frac{D_*^{1.5}}{4}\right)^{0.6} \tag{5.10}$$

where θ_{cr} is the critical Shields parameter for sediment movement and D_* is the non-dimensional particle diameter,

$$D_* = D_{50} \left(\frac{g(s-1)}{\nu^2} \right)^{1/3} \tag{5.11}$$

For $\theta_{cr} < \theta \leq \theta_B$, ripple heights and wavelength are given by,

$$\eta = 0.22 \left(\frac{\theta}{\theta_{cr}} \right)^{-0.16} A_w \tag{5.12}$$

$$\lambda = \frac{\eta}{0.16 \left(\frac{\theta}{\theta_{cr}} \right)^{-0.04}} \tag{5.13}$$

whereas for $\theta > \theta_B$,

$$\eta = 0.48 \left(\frac{D^{1.5}}{4} \right)^{0.8} \left(\frac{\theta}{\theta_{cr}} \right)^{-1.5} A_w \tag{5.14}$$

$$\lambda = \frac{\eta}{0.28 \left(\frac{D^{1.5}}{4} \right)^{0.6} \left(\frac{\theta}{\theta_{cr}} \right)^{-1}} \tag{5.15}$$

where A_w is the wave orbital amplitude. θ_{cr} can be obtained from *Soulsby* (1997) as

$$\theta_{cr} = \frac{0.3}{1 + 1.2D_*} + 0.055 \left(1 - \exp(-0.02D_*) \right) \tag{5.16}$$

Pedocchi and Garcia (2009) (hereafter PG09) suggested that ripple dimensions are related to the ratio of wave orbital velocity to particle settling velocity, U_w/w_s. They proposed expressions for η and λ for three different grain size regimes, based on the particle Reynolds number, $Re_p = \sqrt{(s-1)dD_{50}^3}\nu$. Considering the median particle size of bed sediments at our field site, here we use the expression for the $9 \geq Re_p < 13$ range. This range corresponds to a particle size interval between $177 - 220 \ \mu$m. The equations for ripple height and wavelength are given by,

$$\eta = 0.1d_0 \left[(0.055U_w/w_s)^4 + 1 \right]^{-1} \tag{5.17}$$

$$\lambda = 0.65d_0 \left[(0.040U_w/w_s)^2 + 1 \right]^{-1} \tag{5.18}$$

$$\tag{5.19}$$

The settling velocity w_s can be obtained following *Soulsby* (1997) as

$$w_s = \frac{\nu}{d_{50}} \left[\left(10.36^2 + 1.049 D_*^3\right)^{1/2} - 10.36 \right] \tag{5.20}$$

5.2.5 Bed stresses

Measurements

Turbulence measurements within the wave boundary layer were not made. However, the ADV measurements were able to resolve near-bottom turbulence, and were used to obtain the current-induced friction velocity u_{*c} as

$$u_{*c} = \sqrt{\overline{u'w'}_{filt}^2 + \overline{v'w'}_{filt}^2} \tag{5.21}$$

where the subscript *filt* indicates that the Reynolds stresses were wave-filtered to eliminate any wave bias, as outlined in section 2. The measured current friction velocity u_{*c} is compared with the modeled current friction velocity from *Grant and Madsen* (1979) in order to assess model performance.

Grant and Madsen (1979) wave-current interaction model

The *Grant and Madsen* (1979) model is a wave-current interaction model that allows for the specification of a dynamic bed roughness, which feeds the model hydrodynamics. One of the main assumptions of the model is the existence of a constant stress layer where the bottom stress is approximately equal to the turbulent Reynolds stress. If no waves are present, the velocity profile in the bottom boundary layer is logarithmic and it scales with the friction velocity u_{*c},

$$U(z) = \frac{u_{*c}}{\kappa} \log \left(\frac{z}{z_0} \right) \tag{5.22}$$

where $\kappa \approx 0.4$ is the von Karman constant and z_0 is the hydrodynamic roughness, where velocity goes to zero. The boundary layer for steady currents typically extends for meters above the bed. In contrast, the wave-boundary layer only extends for a few centimeters above the bed, due to the oscillating nature of orbital motions. *Grant and Madsen* (1979) propose that in a combined wave-current flow, the influence of the wave boundary layer is to increase the apparent roughness

felt by currents. Currents are thus reduced near the bed as a result of the increased turbulence in the wave boundary layer. The influence of the waves is modeled by an increase of the eddy viscosity in the wave boundary layer, which scales with wave-current friction velocity u_{*cw} that characterizes the maximum stress associated with the combined effect of waves and currents. *Grant and Madsen* (1979) proposed the following eddy viscosity profile,

$$\nu_t = \begin{cases} \kappa u_{*cw} z & z < \delta_w \\ \kappa u_{*c} z & z > \delta_w \end{cases} \tag{5.23}$$

where δ_w is the height of the wave boundary layer. The wave-current friction velocity u_{*cw} is obtained as (*Madsen*, 1995)

$$u_{*cw} = u_{*w} \left[1 + 2 \left(\frac{u_{*c}}{u_{*w}} \right)^2 \cos\theta + \left(\frac{u_{*c}}{u_{*w}} \right)^4 \right]^{1/4} \tag{5.24}$$

where θ is the angle between waves and currents and u_{*w} is the friction velocity associated with the wave stresses, obtained as

$$u_{*w} = \sqrt{\frac{1}{2} f_w} u_b \tag{5.25}$$

where f_w is a wave friction factor (which depends on bed roughness) and u_b is the bottom wave orbital velocity. The velocity profiles outside and within the wave boundary layer are then given by

$$U(z) = \begin{cases} \frac{u_{*c}^2}{\kappa u_{*cw}} \log\left(\frac{z}{z_0}\right) & z < \delta_w \\ \frac{u_{*c}}{\kappa} \log\left(\frac{z}{z_{0a}}\right) & z > \delta_w \end{cases} \tag{5.26}$$

where z_{0a} is the apparent roughness felt by the currents due to the presence of waves. Bottom roughness is included as a Nikuradse roughness, $z_0 = k_B/30$, where k_B is the physical roughness of bottom irregularities such as ripples.

The modified *Grant and Madsen* (1979) model will be used to obtain bottom stresses resulting from different bottom roughness predictions, and these predictions will be compared against our turbulence measurements.

Prediction of time-evolving ripple dynamics

Soulsby et al. (2012) presented a fully time-evolving model for predicting the dimension of ripples generated by waves, currents or a combination of both. This model will be used in combination with the *Grant and Madsen* (1979) boundary layer model to estimate bed stresses. By comparing with measured data we will show that bed stress calculations using this approach are improved with respect to the the use of equilibrium bedform dimension predictors.

In the *Soulsby et al.* (2012) model, the time evolution of ripple properties under a varying forcing field is modeled as a perturbation from its equilibrium value. The equation governing the time-evolution of bedform dimension is given by,

$$\frac{d\eta}{dt} = \frac{\beta}{T_e} \left(\eta_{eq} - \eta \right) \tag{5.27}$$

where T_e is a characteristic timescale, β is a coefficient that governs the rate of change of η, η_{eq} is the equilibrium value and $\eta = \eta(t)$ is the time dependent bedform height. In general, T_e, β and η_{eq} are functions of time. Equivalent equations are used for the time evolution of bedform wavelength and orientation. *Soulsby et al.* (2012) provide expression for η_{eq} and λ_{eq}, which are based on an extensive review of available formulations. Moreover, the model provides expressions for both current and wave dominated ripples, where the criterion to establish wave or current dominance is based on the skin friction Shields parameter,

$$\theta_w = \frac{(1/2)f_w U_w^2}{g(s-1)D_{50}}, \quad \theta_c = \frac{(C_D U^2}{g(s-1)D_{50}} \tag{5.28}$$

such that if $\theta_w > \theta_c$ ripples are wave dominated, and if $\theta_c > \theta_w$ ripples are current dominated. For wave-dominated ripples, equilibrium heights and wavelengths are given by

$$\frac{\lambda}{A} = \left[1 + 1.87 \cdot 10^{-3}\Delta \left(1 - \exp\{-(2.0 \cdot 10^{-4}\Delta\}^{1.5}) \right) \right]^{-1} \tag{5.29}$$

$$\frac{\eta}{\lambda} = 0.15 \left[1 - \exp\{-(5000/\Delta)^{3.5}\} \right] \tag{5.30}$$

where $\Delta = A/D_{50}$, with A being the orbital amplitude and D_{50} the median particle size diameter. For current-dominated conditions, equilibrium heights and wavelength are based on empirical expressions for the maximum ripple height and wavelengths,

$$\eta_{max} = d_{50} 202 D_*^{-0.554} \quad 1.2 < D_* < 16 \tag{5.31}$$

$$\lambda_{max} = d_{50} \left(500 + 1881 D_*^{-1.5} \right) \quad 1.2 < D_* < 16 \tag{5.32}$$

where $D_* = [g(s-1)/\nu^2]^{1/3} D_{50}$ is the non-dimensional particle size and ν is the kinematic viscosity of water. The effect of wash-out ripples and sheet flow at large current speed is also included by applying a linear reduction in ripple height according to limits based on the Shields parameter,

$$\theta_{wo} = 1.66 D_*^{-1.6} \tag{5.33}$$

$$\theta_{sf} = 2.26 D_*^{-1.3} \tag{5.34}$$

$$\tag{5.35}$$

where the subscripts wo and sf refer to wash-out and sheet flow. Expressions for the ripple height are then given by

$$\eta_{eq} = \text{pre-existing value} \quad \text{for } 0 < \theta_c < \theta_{cr} \tag{5.36}$$

$$\eta_{eq} = \eta_{max} \quad \text{for } \theta_{cr} < \theta_c < \theta_{wo} \tag{5.37}$$

$$\eta_{eq} = \eta_{max} \left(\frac{\theta_{sf} - \theta_c}{\theta_{sf} - \theta_{wo}} \right) \quad \text{for } \theta_{wo} < \theta_c < \theta_{sf} \tag{5.38}$$

$$\eta_{eq} = 0 \quad \text{for } \theta_c > \theta_{sf} \tag{5.39}$$

where θ_{cr} is the critical Shields parameter for motion initiation. Wavelengths are assumed to be unaffected by wash-out. For both wave and current dominated ripples, evolution of height and wavelength occurs only if $\theta > \theta_{cr}$, that is, that the threshold for motion is achieved. Otherwise, the model assumes that ripples are not modified (relict ripples). The parameters controlling the time evolution of ripple dimensions (T_e and β) are also specified for wave-dominated or current-dominated conditions, as the timescales for waves and currents are intrinsically different. For wave-dominated conditions, the timescale T_e is set to be equal to the wave period. The β parameter for wave dominated conditions is given by

$$\beta_w = \frac{2.996\psi^{1.07}}{21700 + \psi^{1.07}} \tag{5.40}$$

where $\psi = U_w^2/g(s-1)d_{50}$ is the wave mobility parameter. The timescale for currents is less obvious than of the waves, and is taken to be related to the time that it takes for the volume per unit with of a ripple to be delivered by the volumetric bedload transport rate. The expression for T_c is given by

$$T_c = \frac{\eta_{max}\lambda_{max}}{[g(s-1)D_{50}^2]^{1/2}} \tag{5.41}$$

Laboratory experiments (*Baas*, 1993) showed that for current generated ripples, bedform height evolved faster than the wavelength, hence, different β parameters are required. These are given by

$$\beta_\eta = \frac{20(\theta_c - \theta_{cr})^{1.5}}{2.5 + (\theta_c - \theta_{cr})^{1.5}} \tag{5.42}$$

$$\beta_\lambda = \frac{12(\theta_c - \theta_{cr})^{1.5}}{2.5 + (\theta_c - \theta_{cr})^{1.5}} \tag{5.43}$$

$$\tag{5.44}$$

For further details on the derivation of these empirical expressions, the reader is referred to *Soulsby et al.* (2012). The time stepping procedure involves solving the differential equation given by Equation 5.27, which can be done using a Runge-Kutta scheme of the 4th order. At each time step, wave or current dominance has to be established, the equilibrium values, T_e and β coefficients have to be computed and the equation for η_{t+1} (or λ_{t+1}) has to be solved. If $\theta < \theta_{cr}$ then $\eta_{t+1} = \eta_t$. The critical Shields parameters can be obtained from the expression proposed by *Soulsby et al.* (1997) as

$$\theta_{cr} = \frac{0.3}{1 + 1.2D_*} + 0.055[1 - \exp(-0.02D_*)] \tag{5.45}$$

Combining a wave-current boundary layer model and a ripple evolution model

The wave-current boundary layer model proposed by *Grant and Madsen* (1979) and the time-dependent ripple evolution model proposed by *Soulsby et al.* (2012) are combined to obtain estimates

of the bed shear stress. This approach presents the advantage that it allows for a two-way feedback between bottom roughness and hydrodynamics, as bedforms evolve in response to the bed stresses but also participate in the determination of such stresses. The time stepping procedure is as follows:

1. Compute bottom roughness based on ripple dimensions ($k_B = \eta^2/\lambda$)

2. Compute wave and current friction velocities according to *Grant and Madsen* (1979)

3. Compute wave and current Shields parameters

4. If $\theta > \theta_{cr}$, decide wave or current dominance

5. Compute equilibrium dimensions and time evolution parameters

6. Solve differential equation for η and λ

7. Recompute bottom roughness and repeat until convergence is achieved.

The procedure converges quickly. Bottom roughness can be initiated with an initial estimation for η and λ or by setting equilibrium values. In what follows, we will refer to this approach as NEB (Non-Equilibrium Bedforms).

5.3 Data analysis and results

5.3.1 Bedform observations

Forcing conditions and bedform parameters derived from the Acoustic Ripple Profiler are shown in Figure 5.1. Bedforms were always present during the deployment, and show a relatively stable background level with bedform height of $\eta \approx 2$ cm and wavelength $\lambda \approx 0.5$ m (Figure 5.1a,b) attained during weak forcing conditions (neap tide and low waves, e.g. days 260-264 and 275-277). We observe a strong correlation between bedform dimensions and bottom orbital velocity (Figures 5.1a,b,d), with bedform heights and wavelengths rapidly increasing during the storm of days 264-266. During this storm, bedform height and wavelength reached $\eta = 4$ cm and $\lambda = 1$ m, respectively. The wave events of days 268, 278 and 281 are also reflected in an increase of

bedform height, however, bedform wavelength seems to be less sensitive to wave orbital velocity than bedform height (e.g. day 278). 2D bedforms are observed when the wave forcing is strong (e.g. Figure 5.1 f, g, i), whereas irregular 3D beforms are present when waves are low and the forcing is current-dominated (Figure 5.1 h, j). Bedform steepness is relatively low (Figure 5.1c), with values in the range of $\eta/\lambda = 0.05 - 0.08$, and with no clear relation to the wave forcing. Tidal currents are also able to induce modify bedform dimensions. When wave forcing is low, spring tide currents result in variations of both bedform height and wavelength (e.g. days 270-273). On the other hand, neap tide currents do not seem to induce clear variations in bedform dimensions (e.g. days 260-264 and 273-278), most likely because the threshold for motion was not exceeded.

5.3.2   Bedform predictions

Bedform dimension predictions for the GM82, WH94 and PG09 models are shown in Figure 5.2. When the threshold for sediment movement was not exceeded ($\theta < \theta_{cr}$), we have chosen to keep the previous value rather than to set bedform dimensions to zero. None of the predictors is able to capture the measured variability in η or λ, and all of them show a clear tendency to overestimate the bedform height. From all three predictors, *Pedocchi and Garcia* (2009) gives the best results with respect to η, however, values are typically overestimated by 2 to 4 cm (Figure 5.2a). Wavelengths are somewhat better predicted by all models, particularly during periods of strong wave forcing (Figure 5.2b). The *Grant and Madsen* (1982) and *Wiberg and Harris* (1994) models accurately predict wavelengths during the first storm of days 264-266, reproducing wavelengths on the order of 1m. The wave event of day 267 is also well reproduced by both predictors in terms of bedform wavelength. During the periods of high wave forcing, both WH94 and GM82 give bedform heights and wavelength that result in $\eta/\lambda \sim 0.15 - 0.17$, which is thought to be the equilibrium steepness value for orbital ripples (*Wiberg and Harris*, 1994). Overall, the *Grant and Madsen* (1982) predictor seems to give the best results regarding bedform wavelength. Note that for a considerable part of the measurement period the threshold for sediment motion was not exceed by the wave stresses, and thus the values remained unchanged. In reality, during these periods the bedforms will be dominated by the current forcing, such that variations in bedform dimensions still occur. These variations are clearly observed in the field data (Figure 5.2), though they are generally smaller than
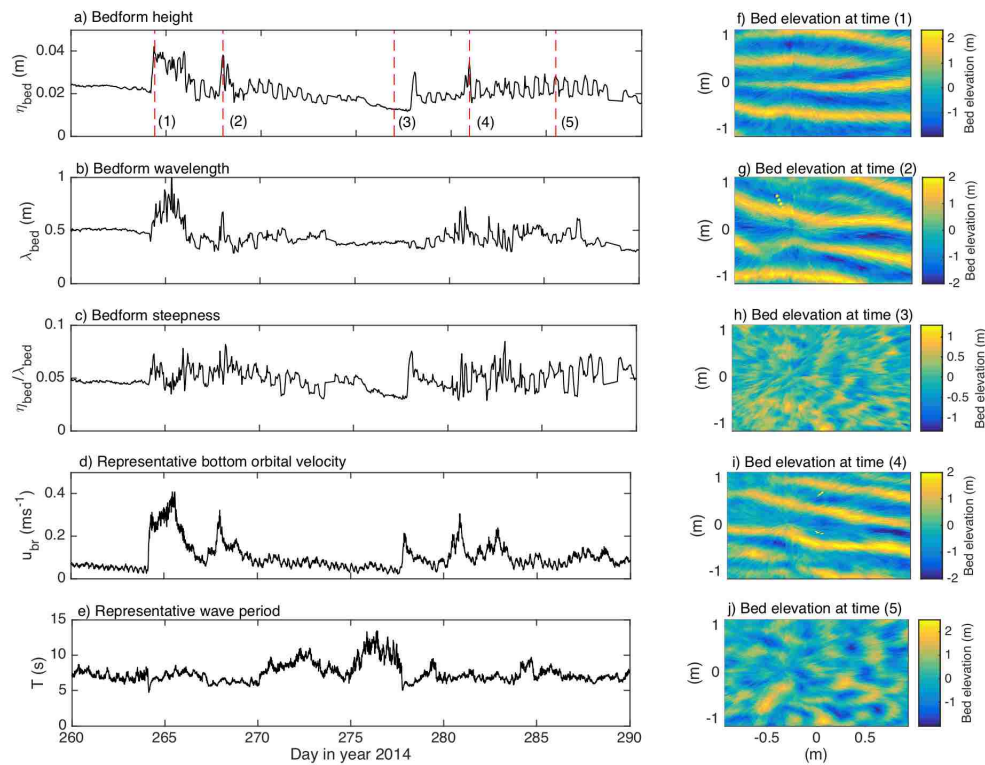
Figure 5.1: Bedforms and wave forcing. (a) Bedform height. (b) Bedform wavelength. (c) Bedform steepness. (d) Representative bottom wave orbital velocity. (e) Representative wave period. (f)-(j) Seafloor images corresponding to times indicated in panel (a).
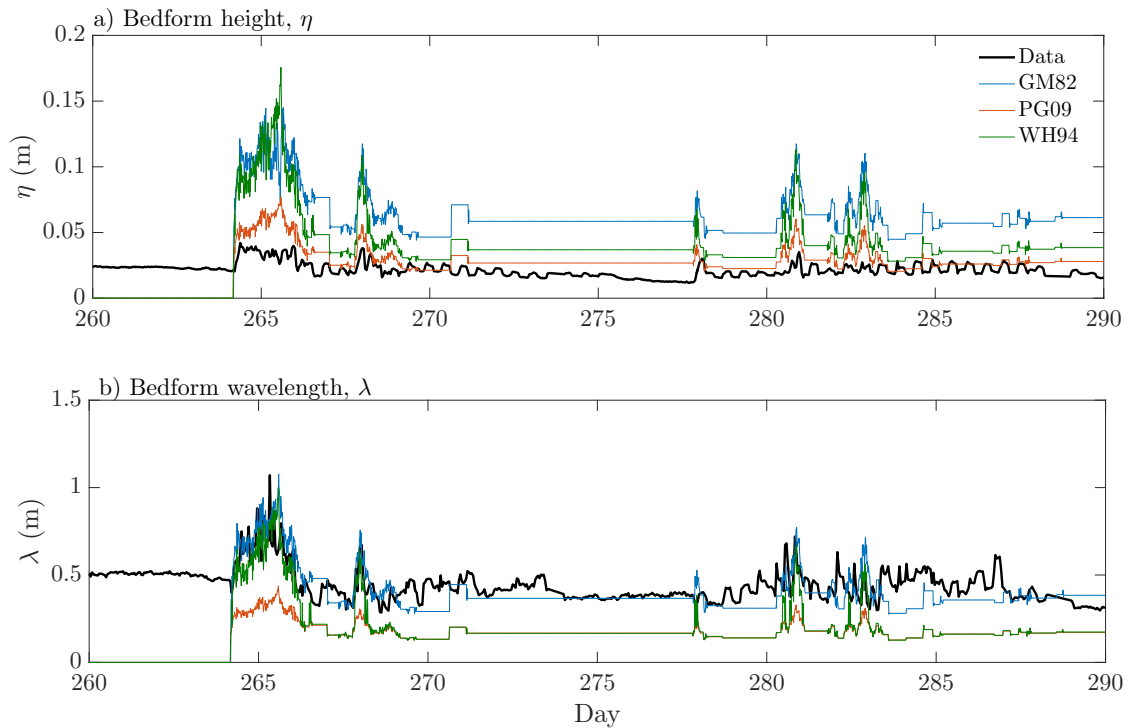
Figure 5.2: Bedform predictors. (a) Bedform height. Measured data (black line), GM82 (blue line), WH94 (green line) and PG09 (red line) predictors. (b) Bedform wavelength. Measured data (black line), GM82 (blue line), WH94 (green line) and PG09 (red line) predictors.

those induced by the waves.

5.3.3   Bed stress estimations

Measured bedforms versus flat bottom

In this section we compare field estimates of u_{*c} against predictions from the *Grant and Madsen* (1979) model. Model calculations have been carried out using bottom roughness values derived from field measurements of bedform dimensions. For comparison, we have also included model estimates where we have used a constant bottom roughness derived from the particle size of bed sediments, $k_B = 2.5D_{50}$ (*Nielsen*, 1992).
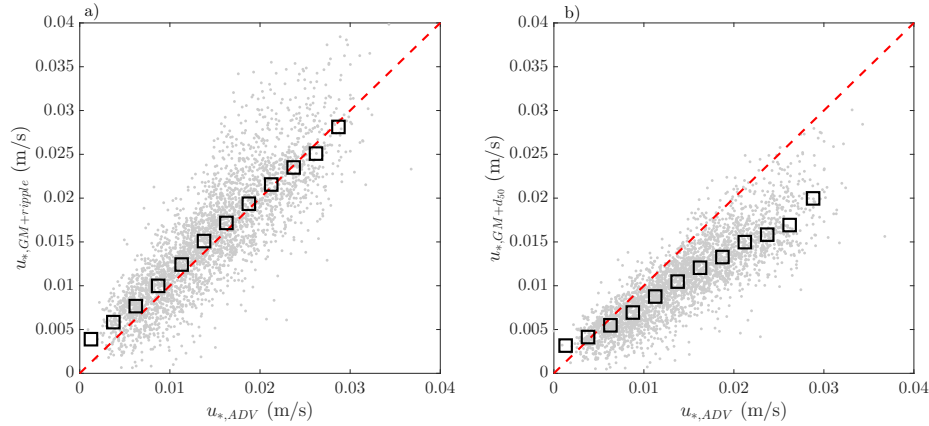
Figure 5.3: Friction velocity predictions versus measured data. (a) Bottom roughness derived from measured ripple dimensions (b) Bottom roughness derived from median grain size, D_{50}

A direct comparison between the wave-filtered ADV measurements and model output is shown in Figure 5.3. Modeled u_{*c} agrees well with the wave-filtered turbulence measurements when measured bedform dimensions are used to estimate bottom roughness (Figure 5.3a). While there is dispersion in the data, the agreement is excellent when considering binned values ($R^2 = 0.95$). This shows the consistency of the boundary layer model when bottom roughness is accounted for properly. Modeled current friction velocities obtained from D_{50} show a clear underestimation with respect to the measured values, particularly in the large u_{*c} range (Figure 5.3b). This suggests that the use of D_{50} only might be justified in low energy cases, when the seabed is expected to remain approximately flat.

Bedform predictors and time-evolving ripple dynamics

The comparison of measured and modeled friction velocities, for cases where bottom roughness was derived using bedform dimensions from the GM82, WH94 and PG09 predictors are shown in Figure 5.4. All three models show a consistent overestimation of bed stresses for the entire range of measured values, with the overestimation increasing at large values of u_{*c}. This is the result of
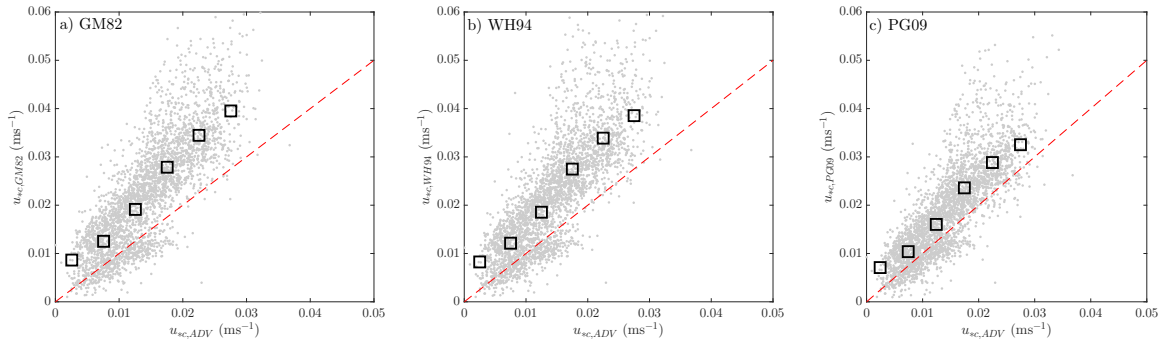
Figure 5.4: Friction velocity predictions versus measured data. ((a) Modeled current friction velocity using the GM82 ripple dimension predictions and the *Grant and Madsen* (1979) bottom boundary layer model versus the measured wave-filtered current friction velocity. (b) Modeled current friction velocity using the WH94 ripple dimension predictions and the *Grant and Madsen* (1979) bottom boundary layer model versus the measured wave-filtered current friction velocity. (c) Modeled current friction velocity using the PG09 ripple dimension predictions and the *Grant and Madsen* (1979) bottom boundary layer model versus the measured wave-filtered current friction velocity.

the observed overprediction of bedform heights at times of strong wave forcing (Figure 5.2). The fact that the PG09 models gives the best results from all three models might be explained by the better estimations of bedform height, since bottom roughness is included in the model as η^2/λ.

Model-data comparison of u_{*c} improves considerably when combining the *Grant and Madsen* (1979) boundary layer model with *Soulsby et al.* (2012) ripple evolution model (Figure 5.5c). Opposite to what was observed for the equilibrium bedform predictors (Figure 5.4), the agreement between modeled and observed u_{*c} improves as u_{*c} increases. This approach computes bed stresses and bedform dimension simultaneously, and results in a much better reproduction of the bedform height, particularly during strong wave forcing periods (Figure 5.5a). However, the agreement in wavelength predictions is very poor (Figure 5.5b such that wavelength dimensions are severely underpredicted during times of high waves and remain more or less stable during low wave forcing. Despite the lat-

ter, the overall agreement in friction velocity is very good, and better than the agreement achieved with any of the standard bedform predictors. Similarly to what was observed in Figure 5.4c for the PG09 predictor, the fact that good u_{*c} predictions can be obtained with a poor reproduction of λ suggests that bedform height controls the bottom roughness due to the quadratic dependence. It is worth noting that even though the *Soulsby et al.* (2012) model accounts for current-dominated bedforms, the bedform dimensions during times of low wave activity are not well reproduced (e.g. days 273-278).

In order to evaluate whether bed stress estimates can be further improved, we use the *Grant and Madsen* (1982) model as the equilibrium predictor in the *Soulsby et al.* (2012) bedform evolution formulation, replacing the predictor proposed in their study (Figure 5.6). Estimates of u_{*c} are greatly improved with respect to the case shown in Figure 5.4a, where we did not include the time-dependent ripple dynamics. We also observe a substantial improvement in bedform height predictions (Figure 5.6a), but at the expense of the bedform wavelength predictions (Figure 5.6b). Similar calculations using the PG09 predictor (not shown) showed that bedform height predictions were also improved, but that changes are not significant during high wave forcing periods. The difference in response between both predictors can be explained by the fact that the GM82 formulation uses the wave-induced stress to obtain the equilibrium bedform dimensions. An advantage of this approach is that the equilibrium predictor in the *Soulsby et al.* (2012) model can be easily interchanged and thus predictors that have been proven to work satisfactorily at a specific site can be readily used.

5.4 Fine sediment resuspension

In this section we present near-bed sediment concentrations and fluxes in order to gain insight about the resuspension of fine sediments under the influence of large waves and strong currents. In particular, we will make use of Equation 5.46 to infer how the resuspension coefficient M varies according to i) how bed stresses are estimated and ii) the wave and current forcing.
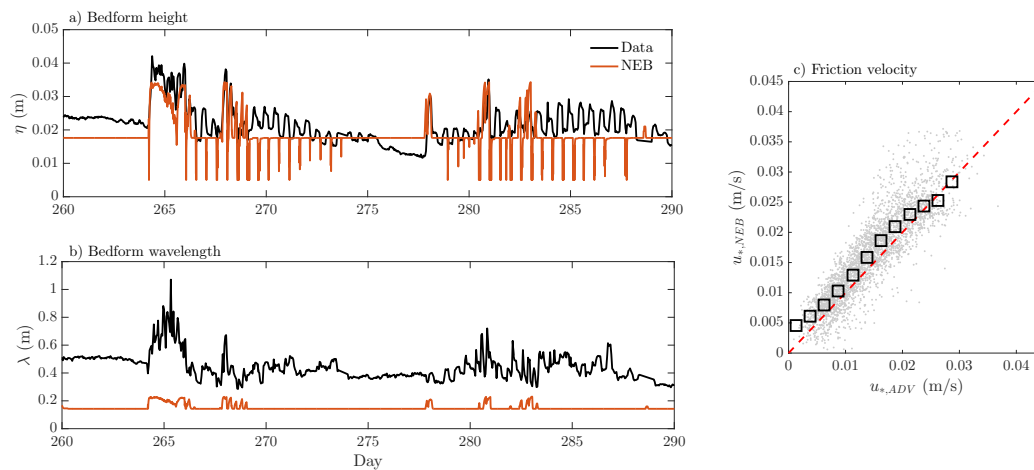
Figure 5.5: (a) Measured (black line) and predicted (red line) bedform height. (b) Measured (black line) and predicted (red line) bedform wavelength. (c) Modeled current fiction velocity using the *Soulsby et al.* (2012) ripple evolution model and *Grant and Madsen* (1979) versus measured current friction velocity.

5.4.1 Turbulent sediment fluxes

The near-bed vertical turbulent sediment fluxes, sediment concentrations and bed stresses are shown in Figure 5.7. In Figure 5.7, bed stresses correspond to those estimated using the *Grant and Madsen* (1979) model and measured bedform data. Both the near-bottom turbulent sediment fluxes (Figure 5.7c) and suspended sediment concentrations (Figure 5.7d) follow the wave forcing closely (Figure 5.7a,b), with the highest concentrations and fluxes occurring during the storms of days 264-266 and days 281-284. Resuspension due to tidal currents is observed primarily during spring tides (e.g. days 267-270 and 285-288), however, the contribution of tidal currents to the total bottom stress frequently exceed that of waves (Figure 5.7a,b).
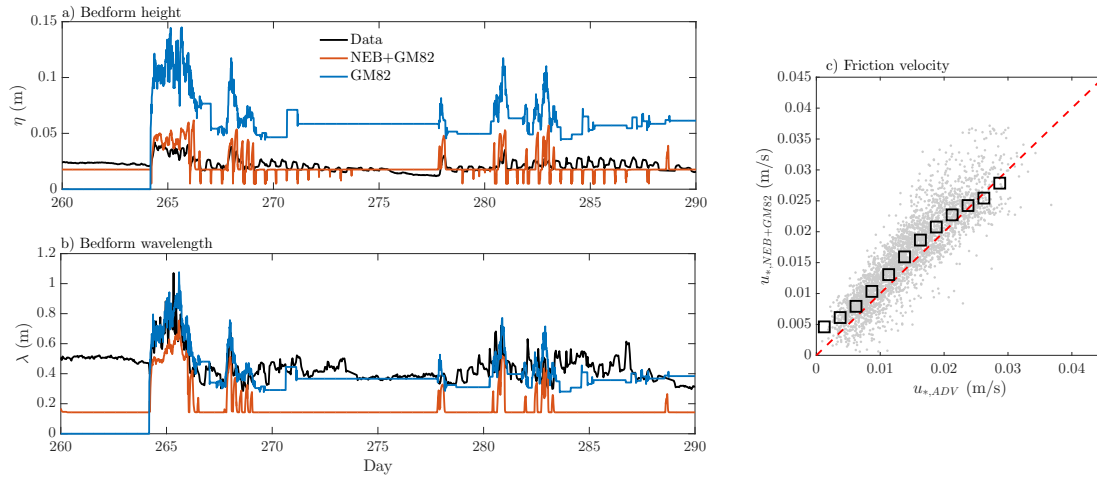
Figure 5.6: (a) Measured bedform height (black line), predicted bedform height using the GM82 predictor (as in Figure 5.2, red line) and modeled bedform height using the *Grant and Madsen* (1979) boundary layer model in combination with the *Soulsby et al.* (2012) model, using GM82 to estimate equilibrium bedform dimensions (blue line).

Fine sediment resuspension

In what follows, we assume that the vertical turbulent fluxes $\overline{w'c'}$ provide a good estimate of fine sediment resuspension. This assumption neglects horizontal processes, and assumes that the very near-bed sediment concentrations are determined by a vertical balance (Equation 5.2). The assumption that $\overline{w'c'}$ provides a good estimate of fine sediment resuspension is supported by Figures 5.7 and 5.8, which show a clear correlation between the turbulent fluxes, sediment concentrations and bed stresses.

The erosion of fine sediment is typically modeled using a linear formulation (*Partheniades*, 1965; *Van Prooijen and Winterwerp*, 2010; *Sanford and Maa*, 2001),

$$E = M \left(\tau_{cw} - \tau_{cr} \right) \tag{5.46}$$

As discussed previously, the accurate estimation of the erosional fluxes rely on the accurate pre-
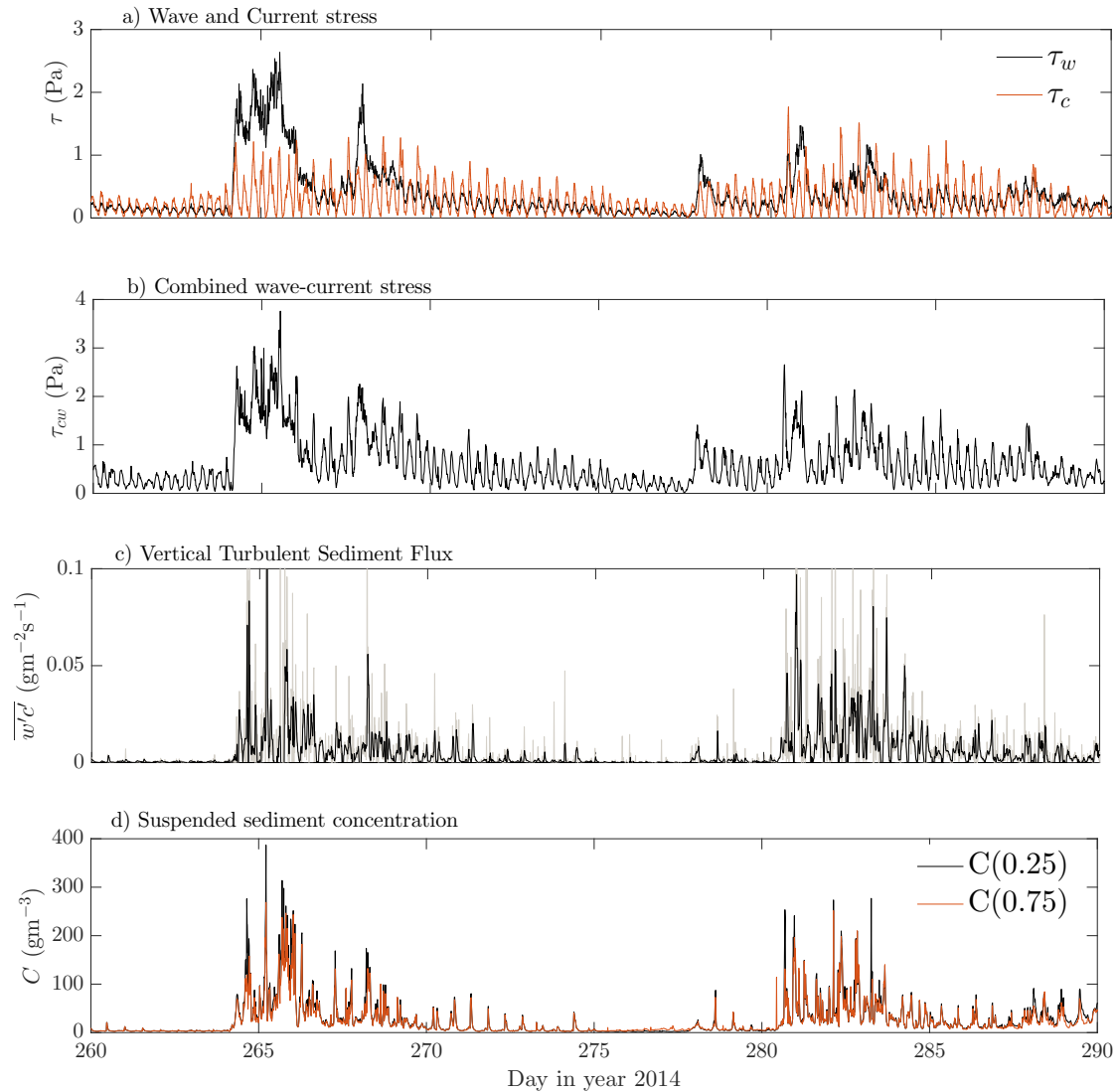
Figure 5.7: Bed stresses, turbulent sediment fluxes and suspended sediment concentration. (a) Wave (black line) and current (red line) stresses. (b) Combined wave-current stresses. (c) Vertical turbulent sediment flux. Gray line corresponds to the raw data and black line corresponds to a 2-hr median filter. (d) Suspended sediment concentrations at 0.25mab (black line) and 0.75mab (red line).

diction of the bed stresses, but also on the resuspension parameter M and the critical stress for erosion, τ_{cr}. These parameters are extremely difficult to estimate directly in the field as they require high resolution measurements at (or very close to) the seabed. Numerical models, such as ROMS or DELFT3D, usually require M and τ_{cr} to be specified by the user for sediment transport calculations. Thus, is of practical importance to have good estimates of the M parameter derived from field measurements.

Field estimates of M and τ_{cr} have been obtained by setting $E = \alpha\overline{w'c'}$, where α is a proportionality constant that is function of distance above the bed (*Brand et al.*, 2015). As we did not have the information to estimate α, we have chosen to set $\alpha = 1$, which may lead to a slight underestimation of the erosional fluxes. A least-squares linear regression between $\overline{w'c'}$ and τ_{cw} then provides estimates of M and τ_{cr}. Evidently, both M and τ_{cr} will vary according to the bed stresses that are used as input in Equation 5.46. We consider that the bed stresses obtained using measured bedform dimensions will provide the best estimates of M and τ_{cr}.

Linear fits to Equation 5.46 are shown in Figure 5.8, for cases where the bottom stresses (τ_{cw}) were computed using measured bedform geometry (black squares), d_{50} (red squares) and for the NEB approach (blue squares). While dispersion is observed regarding the instantaneous τ_{cw} and $w'c'$ values (see dashed lines in Figure 5.8), a linear relation is indeed observed for the binned values, particularly at high values of τ_{cw}. The linear regressions to Equation 5.46 are performed using the binned values, and the values we obtained are shown in Table 5.1. Table 5.1 also shows values obtained for cases where the GM82, WH94 and PG09 were used to estimate bottom roughness. We observe that fitted values of both M and τ_{cr} are very similar for the cases of bed stresses computed using measured bedform dimensions and for the case where we used the *Soulsby et al.* (2012) model, as both of these approaches resulted in very good estimates of the bed stresses (Figure 5.8). This further confirms that the NEB approach provides a robust method for the estimation of the bed stresses. We see that the use of d_{50} results in a severe overestimation of the M parameter, which is twice as high as the value obtained when measured bedform where used to estimate stresses (Figure 5.8). The opposite is true with respect to τ_{cr}, as the value obtained for the d_{50} case is substantially lower. M and τ_{cr} values for cases where the GM82, WH94 and PG09 predictors were used in
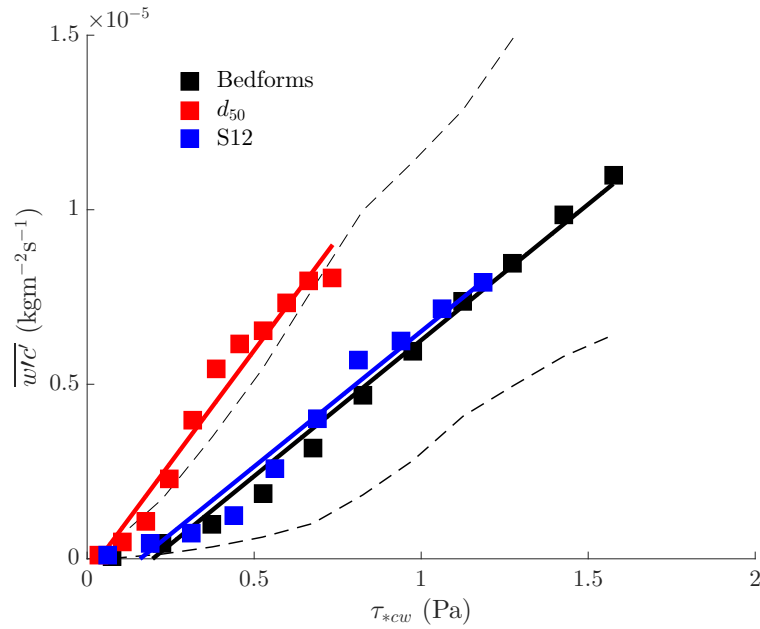
Figure 5.8: Combined wave-current bed stress versus turbulent sediment flux, for the cases where bed stress was estimated using the *Grant and Madsen* (1979) model and estimates of bottom roughness obtained from measured bedform dimensions (black squares), d_{50} (red squares) and the *Soulsby et al.* (2012) model. These values correspond to bin averages of the data. Solid lines correspond to the fits to Equation 5.46. Dashed lines correspond to the 25th and 75th percentiles for the case where measured bedforms were used in the computation of bed stresses (black squares).

the estimation of stresses are shown in Table 5.1, where it can be appreciated that τ_{cr} is clearly overestimated. Overall, we see that these values are in general agreement (order of magnitude) with values presented in the literature (*Sanford and Maa*, 2001) and values used along the Dutch coast (*Van Kessel et al.*, 2011). However, a direct comparison of the values found in this study with values found in other field sites or in the laboratory is not possible due to all the factors that affect the erodibility of fine sediments.

Table 5.1: Fitted M and τ_{cr} parameters

Case	M (kg/m^{-2}s^{-1}Pa^{-1})	τ_{cr} (Pa)
Bedforms	$7.78 \cdot 10^{-6}$	0.19
d50	$1.28 \cdot 10^{-5}$	0.03
NEB	$7.74 \cdot 10^{-6}$	0.15
GM82	$2.94 \cdot 10^{-6}$	0.3
WH94	$3.27 \cdot 10^{-6}$	0.32
PG09	$4.08 \cdot 10^{-6}$	0.13

5.5 Discussion

5.5.1 Non-equilibrium ripple dynamics

Non-equilibrium ripple dynamics affect bottom drag and bed stresses, thus directly influencing coastal circulation patterns in continental shelves (*Scully et al.*, 2018). Accounting for the time-dependent development of ripple dimensions (height, wavelength) was shown to improve the estimates of bed stresses with respect to the traditional approach of using equilibrium ripple predictors in order to obtain bottom roughness (Figures 5.5 and 5.6).

The (*Soulsby et al.*, 2012) model uses the following equation to solve the time-dependent bedform dynamics,

$$\frac{d\eta}{dt} = \frac{\beta}{T}\left(\eta_{eq} - \eta\right) \tag{5.47}$$

where η_{eq} and $\eta = \eta(t)$ are the equilibrium bedform height and the actual bedform height at time t, respectively. Evidently, if $\eta(t) = \eta_{eq}$ then $d\eta/dt = 0$ and the bedforms are in equilibrium with the forcing conditions. The time evolution of $d\eta/dt$ for a subset of the data is shown in Figure 5.9, which allows for the identification of equilibrium and non-equilibrium bedform conditions. This case is the same as the one presented in Figure 5.5. We see that predicted bedform dynamics rapidly reach a state that is close to equilibrium ($d\eta/dt \approx 0$) shortly after start of the big storm of days 264-266.

This is consistent with laboratory observations showing that ripple dimensions rapidly attain equilibrium dimensions under strong wave forcing (*O'Donoghue and Clubb*, 2001; *Marsh et al.*, 1999). Non-equilibrium conditions are typically observed under lower energy conditions, either under decaying wave forcing (e.g. day 266) or current-dominated conditions (Figure 5.9a,c). In particular, ripple dynamics are frequently predicted to be out of equilibrium at times close to peak flood tide, when current stresses (Shields parameter, θ_c) exceeds both the wave stresses and the critical stress for sediment movement. Under these conditions, the model predicts decreasing bedform height as the current Shields number exceeds the washout limit ($\theta_c > \theta_{wo}$). Ripple heights quickly recover after peak flood reaching $\eta = \eta_{max}$ for current dominated conditions. This suggests that the limits given by Equations 5.39 may not apply to this specific field site, or, alternatively, that the grain size may not be appropriately characterized, as it is expected to continuously vary thoughout the deployment.

5.5.2 Fine sediment resuspension

Estimates of the resuspension parameter M and τ_{cr} were shown to be very sensitive to the approach followed to estimate bed roughness (Figures 5.8 and Table 5.1). In Figure 5.8, we used the complete dataset (30 days) to estimate M and τ_{cr} in order to obtain values that are representative of a wide range of forcing conditions. The M and τ_{cr} values are thus expected to be highly influenced by the periods of high wave forcing that occurred during the storms, which led to highest turbulent sediment fluxes (Figure 5.7). A fit to Equation 5.46 for a period with current-dominated conditions (low wave forcing) results in $M = 1.06 \times 10^{-5}$ (kgm^{-2}s^{-1}Pa^{-1}) and $\tau_{cr} = 0.03$ Pa. These values are very different from those obtained with the use of the complete data set. The critical stress for erosion decreases almost by an order of magnitude in response to the lower stresses observed during current-dominated conditions, and its value aligns much better with what can be expected for the critical stress of fine (silt-sized) sediments. A possible interpretation of this is that during current-dominated conditions, fine sediment resuspension results from the erosion of a fluff layer that forms during slack tides when tidal currents cease and fine sediments are allowed to settle. This fluff layer erodes easily and thus the critical stress for erosion is very low.
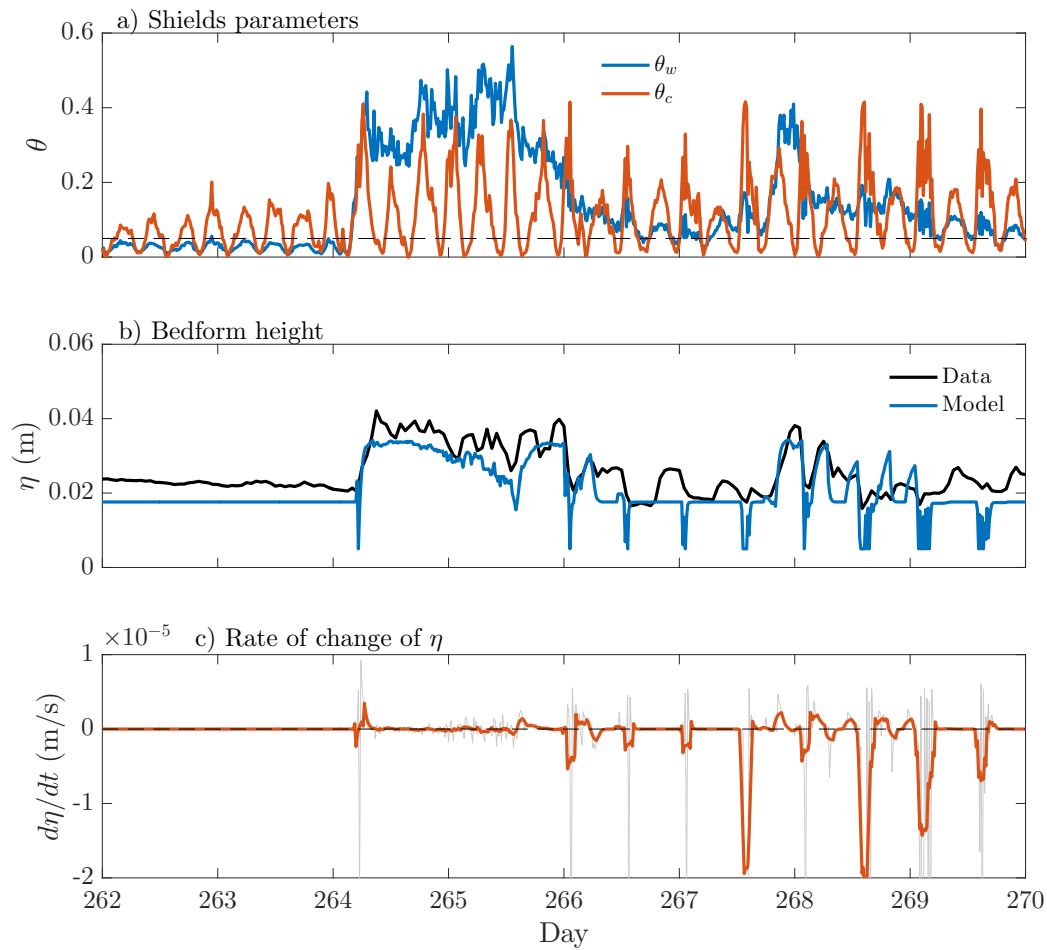
Figure 5.9: Non-equilibrium ripple dynamics. (a) Wave (blue line) and current (red line) Shields parameters. (b) Measured ripple height (black line) and modeled ripple height (blue line). (c) time rate of change of bedform height. Gray line represents the raw data and red line corresponds to a 2-hr median filter.

This contrasts with results shown in Figure 5.8 and Table 5.1 for the cases where bottom roughness was obtained from measured bedform data or the NEB approach, as the inferred critical stress is more representative of fine sands rather than silts. This is found to be consistent with studies suggesting that fine sediment erosion during high energy periods is dominated by the release of fines that are stored within the sandy matrix (*Van Kessel et al.*, 2011). Since the big storm of days 264-266 was the first storm of the fall season in 2014, an alternative explanation for the elevated critical stresses is that the bed sediments may have presented a large degree of consolidation, as they were allowed to consolidate for a long period of time during calm summer months. The critical stress for erosion has been shown to depend on a wide variety of factors, such as the proportion of sands and fines, geochemical properties (mineralogy, PH) and organic content and biological properties (*Grabowski et al.*, 2011; *Dickhudt et al.*, 2011). From our measurements, we cannot really differentiate between all the processes that might lead to differences in τ_{cr}.

5.6 Conclusions

In this chapter, we used near-bed turbulence and bedform geometry measurements to i) investigate the effects of incorporating a time-dependent bedform evolution model into bed stress calculations and ii) obtain field estimates of the M and τ_{cr} parameters based on vertical turbulent sediment fluxes $\overline{w'c'}$.

Using the measured wave-filtered Reynold stresses as the reference values, we found that the best agreement in the prediction of bed stresses was obtained for the case where measured bedforms (height, wavelength) were used to estimate bottom roughness. As bedform geometry measurements are rarely available due to the sophisticated instrumentation that is required, we tested 3 different bedform dimension predictors and found that all three overestimated both the bedform dimensions and the bed stresses at this particular field site.

We proposed a methodology to include time-dependent ripple dynamics into bed stress calculations. This approach combines the *Grant and Madsen* (1979) boundary layer model and the *Soulsby et al.*

(2012) bedform evolution model, and was shown to improve bed stress estimates when compared to those obtained from the use of standard ripple geometry predictors. Bedform dimensions obtained by this approach were also improved, however, discrepancies with field data were still obvious, particularly for current-dominated conditions. The combination of these models presents three main advantages; first, it does not require additional information with respect to that required by standard bedform predictors and the *Grant and Madsen* (1979) model. Second, a two-way feedback is established between the bed stresses, and bottom roughness, as bed stresses participate in determining the evolution of the bedforms and bedforms participate in setting the magnitude of the stresses via the bottom roughness. And third, since the *Soulsby et al.* (2012) model relies on equilibrium ripple predictors to compute the time-dependent ripple dimensions, the predictor can be adapted to use an equilibrium formulation that gives good results at any specific field site.

The dynamics observed regarding the resuspension of fine sediment highlight the importance of waves and storms in the sediment transport dynamics along the Dutch coast. The vertical turbulent sediment flux data were incorporated into a linear erosion formulation and used to obtain field estimates of the resuspension parameter M and the critical stress for erosion tau_{cr}. These parameters were shown to be highly sensitive to the quality of the bed stresses used in the calculations. When using the best stress estimate (using measured bedform data), the critical stress for erosion was found to be $\tau_{cr} \approx 0.2$ (Pa). This value is more representative of fine sands than fine sediments, supporting the hypothesis that the entrainment of fines primarily occurs when sands are being mobilized during storms. Values of M are within an order of magnitude of previously reported values and might serve to inform sediment transport models in the Dutch coast region along the southern North Sea.

Chapter 6

CONCLUSIONS

6.1 Summary

In this thesis, field measurements and a numerical model were used to investigate the processes that lead to cross-shore sediment transport in the Rhine region of freshwater influence. Transport dynamics were investigated in different dynamical regions of the plume; the measurements, which were taken close to the the Rhine river mouth, are representative of the mid-field plume dynamics, whereas the numerical model was designed to be representative of the far-field region. Overall, we presented a comprehensive description of several physical processes that lead to cross-shore transport, including the first report of the occurrence of a WSGF in this region (Chapter 3).

Density stratification plays a crucial role in the cross-shore transport dynamics all along the ROFI. In Chapter 2, collocated measurements of flow velocity, suspended sediment concentration and salinity were used to evaluate the magnitude and direction of sediment transport over a 30-day period, with emphasis on near-bed transport. Results indicate that baroclinic processes contribute to sediment transport on a wide range of time scales. Tidal plume fronts generate offshore fluxes in the lower half of the water column that usually last for a few hours. These results are consistent with the observations of *Horner-Devine et al.* (2017). The net contribution of fronts, however, depends on the state of water column stratification on longer timescales. Persistent water column stratification was found to lead to landward (onshore) subtidal sediment fluxes, such that a net offshore transport due to fronts will only occur when ambient stratification is low.

Storms play a dominant role in the dynamics of this shallow region, as they are able to destroy stratification and mobilize large amounts of bed sediments through wave-induced resuspension. Two storms, spanning a total of 6 days, accounted for more than half of the observed suspended near-bed transport. The transport direction during both storms was offshore, and the transport

was strongly influenced by the occurrence of cross-shelf winds (*Lentz and Fewings*, 2012). The main conclusion from these observations is that, regardless of the proximity of the river mouth, both barotropic and baroclinic processes are equally relevant for the net cross-shore transport in the mid-field region. The switching between these conditions in response to the forcing conditions will determine whether sediments are exported to the shelf or accumulated in the nearshore.

Storms have the potential of contributing to cross-shelf transport not only in terms of suspended load throughout the water column, but also in terms of the generation of wave-supported gravity driven flows. In Chapter 3, we presented the first field measurements of the occurrence of a WSGF event derived from a sandy seabed. This has important implications for the sediment budget along the Dutch coast and many other regions around the world, where WSGF were not thought to occur. Analysis of the observed WSGF dynamics showed that the force balance that is typically used to model these events in muddy environments (*Wright and Friedrichs*, 2006; *Traykovski et al.*, 2007) also governs the dynamics of gravity-driven sediment flows in environments with a much coarser particle size distribution. Richardson number calculations suggest that particle size limits the amount of downslope transport in the WSGF and the characteristics of the turbulent suspension.

One of the main features of sediment transport dynamics along the Rhine ROFI is the existence of a nearshore turbidity maximum zone, that extends for at least 40 km along the coast (*van der Hout et al.*, 2015, 2017). The high rates of transport observed during the WSGF event suggest that these episodic events may contribute to the maintenance of this TMZ along the Dutch coast. In Chapter 4, a numerical model was used to show how the cross-shore tidal straining mechanism contributes to the generation and maintenance of this nearshore TMZ. We found that tidal strain-ing generates landward residual sediment fluxes that result from an asymmetry in vertical mixing between the stratifying and de-stratifyng phases of the tidal cycle. Model results are consistent with the field observations of (*van der Hout et al.*, 2015) in terms the location and extension of the TMZ. The mechanism for sediment convergence is similar to the mechanism that leads to the formation of estuarine turbidity maxima (*Jay and Musiak*, 1994; *Burchard et al.*, 2013), but in the case presented here the effects of Earth's rotation result in sediment convergence in a direction that is perpendicular to the direction of the freshwater flux. A parameter space obtained based

on the model simulations suggests that similar dynamics might be observed in other ROFI systems.

Bottom friction plays an important role in the dynamics of the Rhine ROFI and the observed transport mechanisms. Near-bed turbulence and bedform measurements were used to investigate sediment dynamics in the bottom boundary layer, primarily in terms of the estimation of bed stresses and the resuspension of fine sediments from a mixed sand-silt seabed (Chapter 5). The effect of bottom roughness on the estimation of bed stresses was tested by comparing the near-bed Reynold stresses against the output of a widely accepted wave-current interaction model (*Grant and Madsen*, 1979). The best agreement was found for cases where measured bedform data was incorporated into the model. The use of bottom roughness as inferred from particle size distribution was found to underpredict bed stresses, whereas the use of bedform dimension predictors from the literature (*Wiberg and Harris*, 1994; *Pedocchi and Garcia*, 2009) overpredicted bottom stresses. The combination of a time-dependent bedform predictor (*Soulsby et al.*, 2012) and the wave-current interaction model (*Grant and Madsen*, 1979) was shown to improve bed stress estimates and perform similarly to the case where measured bedform dimensions were used. This methodology provides a simple approach to consider non-equilibrium ripple dynamics in the estimation of bed stresses, and does not require additional information other what is usually required to estimate bed stresses.

Analysis of near bed turbulent sediment fluxes confirmed the importance of wave forcing in the sediment transport dynamics along the Rhine ROFI. The highest vertical turbulent sediment fluxes were observed during storm periods, and the fluxes correlated well with the magnitude of the combined wave-current bottom stresses. Measurements of the near-bed vertical turbulent fluxes $\overline{w'c'}$ were used to estimate the critical stress for erosion and the erodibility constant that are typically used to model the erosion of cohesive sediments.

6.2 Open questions

While much was learned from the measurements and analyses presented here, a number of questions remain unanswered. Many of these questions arose over the course of this Ph.D. work and in response to the findings exposed in previous chapters. Open questions are listed below:

- What is the effect of alongshore processes on the sediment transport dynamics in this region? Are tidal plume fronts able to mobilize fine sediments as they propagate to the shore?

- What is the frequency of occurrence of WSGF events? What is the role of fine sediments in WSGF dynamics on sandy sites? What is the critical fraction of fines that is needed to generate a WSGF?

- How does particle size affect the characteristics of the turbid turbulent suspension in WSGFs? Is the critical Richardson number related to particle size, or Rouse number?

- Is cross-shore tidal straining the dominant mechanism contributing to the formation of nearshore TMZ? Does this TMZ exist all along the Dutch coast, as it is hypothesized? Is there a seasonal variability, and an alonghore variability?

- Can a TMZ such as the one studied here occur in ROFI systems where the tide behaves as a standing wave? How do surfzone processes contribute to the maintenance of TMZ?

- What is the role of tidal currents during periods of wave-dominated bedforms, and viceversa? Are there other dynamical models that may better describe the temporal evolution of bedforms?

6.3 Future directions

Among all the physical processes discussed here, the occurrence of a WSGF on a sandy environment was probably the most important finding. While much has been learned from previous reports of WSGF on muddy shelves (*Traykovski et al.*, 2007; *Hale and Ogston*, 2015), the occurrence of WSGF on environments with much coarser particle size may involve a very different set of dynamics. Future field and laboratory experiments are needed in order to understand how these flows form and evolve in mixed size environments, and how larger particle size affects the turbulent characteristics of the sediment suspension. The inherent difficulty in predicting these events occur suggests that laboratory experiments may be better suited to study these flows in a systematic way. Although some work has been carried out to investigate high-density suspensions with mixed particle sizes

(*Lamb and Parsons*, 2005; *Hooshmand et al.*, 2015), the fraction of coarse sediment in these studies was small in comparison with the field observations we have presented here. High resolution measurements of suspended sediment concentrations, turbulence, and perhaps most importantly, of the particle size distribution within the sediment-water mixture, are required in order to better understand the dynamics of these flows. Research on these topics would likely be impactful as WSGF are not phenomena that are restricted to ROFI systems, and thus have implications for cross-shelf exchange processes in many regions worldwide.

Characterizing near-bed turbulence and bed stresses in the presence of waves, currents, bedforms and overlying stratification remains a challenge. Recent work has shown how large spatial and temporal variations in drag result from non-equilibrium ripple dynamics, ripple anisotropy and sediment type (*Scully et al.*, 2018). All these processes affect coastal circulation and sediment transport processes on the continental shelf. While several bedform dimension predictors are available in the literature, the vast majority of these assumes that the bedforms are in equilibrium with the forcing conditions. These type of models are widely used, primarily because of their simplicity since they require bulk wave or current parameters that are commonly available in field studies. However, the dispersion in the predictions obtained from these models suggests that accurate information about the state of the seabed may not be obtained from such formulations, which has important implications for coastal circulation and transport models. Further research is needed in terms of developing time-dependent bedform models, such as the ones proposed by *Soulsby et al.* (2012) or *Traykovski* (2007), capable of evolving bedform dimensions on short time scales in response to changing wave and current forcing. Similarly, further research is needed regarding the parameterization of current-dominated bedforms. The study of these type of bedforms has been somewhat neglected when compared to the study of wave-generated bedforms, despite the fact that tidal currents can often be comparable to wave orbital velocities and may dominate dynamics for longer periods of time.

Perhaps one of the largest remaining questions is how the dynamics observed in the Rhine ROFI may translate to other ROFI systems. The results presented in Chapter 4 suggest that a coastal TMZ may occur in other regions that are influenced by horizontal density gradients, however, observations

in other systems have not been reported. Field observations of tidal straining in coastal seas have been mostly restricted to the Liverpool Bay ROFI (*Simpson et al.*, 1990; *Verspecht et al.*, 2009b) and the Rhine (*Simpson et al.*, 1993; *Simpson and Souza*, 1995). Thus, future investigations hoping to better understand where and when tidal straining dynamics might be expected in coastal seas, and what is their effect on transport dynamics are required. For the particular case of the Dutch coast, further research (hopefully field-based) oriented to investigate the asymmetries in near-bottom the turbulence processes that control the transport of fine sediments is highly recommended.

BIBLIOGRAPHY

Amos, C., and M. Collins (1978), The combined effects of wave motion and tidal currents on the morphology of intertidal ripple marks; the wash, uk, *Journal of Sedimentary Research*, *48*(3), 849–856.

Amos, C., A. Bowen, D. Huntley, and C. Lewis (1988), Ripple generation under the combined influences of waves and currents on the canadian continental shelf, *Continental Shelf Research*, *8*(10), 1129–1153.

Amoudry, L. O., and A. J. Souza (2011), Deterministic coastal morphological and sediment transport modeling: A review and discussion, *Reviews of Geophysics*, *49*(2).

Amoudry, L. O., R. Ramirez-Mendoza, A. J. Souza, and J. M. Brown (2014), Modelling-based assessment of suspended sediment dynamics in a hypertidal estuarine channel, *Ocean Dynamics*, *64*(5), 707–722.

Ardhuin, F., W. O'reilly, T. Herbers, and P. Jessen (2003), Swell transformation across the continental shelf. part i: Attenuation and directional broadening, *Journal of Physical Oceanography*, *33*(9), 1921–1939.

Baas, J. H. (1993), *Dimensional analysis of current ripples in recent and ancient dePositional environments*, Faculteit Aardwetenschappen.

Baumert, H., and G. Radach (1992), Hysteresis of turbulent kinetic energy in nonrotational tidal flows: A model study, *Journal of Geophysical Research: Oceans*, *97*(C3), 3669–3677.

Betteridge, K. F., P. D. Thorne, and R. D. Cooke (2008), Calibrating multi-frequency acoustic backscatter systems for studying near-bed suspended sediment transport processes, *Continental Shelf Research*, *28*(2), 227–235.

Bolaños, R., P. D. Thorne, and J. Wolf (2012), Comparison of measurements and models of bed stress, bedforms and suspended sediments under combined currents and waves, *Coastal Engineering*, *62*, 19–30.

Brand, A., J. R. Lacy, K. Hsu, D. Hoover, S. Gladding, and M. T. Stacey (2010), Wind-enhanced resuspension in the shallow waters of south san francisco bay: Mechanisms and potential implications for cohesive sediment transport, *Journal of Geophysical Research: Oceans*, *115*(C11).

Brand, A., J. R. Lacy, S. Gladding, R. Holleman, and M. Stacey (2015), Model-based interpretation of sediment concentration and vertical flux measurements in a shallow estuarine environment, *Limnology and Oceanography*, *60*(2), 463–481.

Brown, J. M., L. O. Amoudry, A. J. Souza, and J. Rees (2015), Fate and pathways of dredged estuarine sediment spoil in response to variable sediment size and baroclinic coastal circulation, *Journal of environmental management*, *149*, 209–221.

Burchard, H., and R. D. Hetland (2010), Quantifying the contributions of tidal straining and gravitational circulation to residual circulation in periodically stratified tidal estuaries, *Journal of Physical Oceanography*, *40*(6), 1243–1262.

Burchard, H., and H. M. Schuttelaars (2012), Analysis of tidal straining as driver for estuarine circulation in well-mixed estuaries, *Journal of Physical Oceanography*, *42*(2), 261–271.

Burchard, H., G. Flöser, J. V. Staneva, T. H. Badewien, and R. Riethmüller (2008), Impact of density gradients on net sediment transport into the wadden sea, *Journal of Physical Oceanography*, *38*(3), 566–587.

Burchard, H., R. D. Hetland, E. Schulz, and H. M. Schuttelaars (2011), Drivers of residual estuarine circulation in tidally energetic estuaries: Straight and irrotational channels with parabolic cross section, *Journal of Physical Oceanography*, *41*(3), 548–570.

Burchard, H., H. M. Schuttelaars, and W. R. Geyer (2013), Residual sediment fluxes in weakly-to-periodically stratified estuaries and tidal inlets, *Journal of Physical Oceanography*, *43*(9), 1841–1861.

Chapman, D. C., and S. J. Lentz (1994), Trapping of a coastal density front by the bottom boundary layer, *Journal of Physical Oceanography*, *24*(7), 1464–1479.

Chapman, D. C., and S. J. Lentz (1997), Adjustment of stratified flow over a sloping bottom, *Journal of Physical Oceanography*, *27*(2), 340–356.

Chen, S.-N., W. R. Geyer, and T.-J. Hsu (2013), A numerical investigation of the dynamics and structure of hyperpycnal river plumes on sloping continental shelves, *Journal of Geophysical Research: OCEANS*, *118*(5), 2702–2718.

Dagg, M., R. Benner, S. Lohrenz, and D. Lawrence (2004), Transformation of dissolved and particulate materials on continental shelves influenced by large rivers: plume processes, *Continental shelf research*, *24*(7), 833–858.

Davidson, M. A., P. E. Russell, D. A. Huntley, and J. Hardisty (1993), Tidal asymmetry in suspended sand transport on a macrotidal intermediate beach, *Marine geology*, *110*(3-4), 333–353.

Davis, J. P., D. J. Walker, M. Townsend, and I. R. Young (2004), Wave-formed sediment ripples: Transient analysis of ripple spectral development, *Journal of Geophysical Research: Oceans*, *109*(C7).

De Boer, G. J. (2009), On the interaction between tides and stratification in the rhine region of freshwater influence.

De Boer, G. J., J. D. Pietrzak, and J. C. Winterwerp (2006), On the vertical structure of the rhine region of freshwater influence, *Ocean dynamics*, *56*(3-4), 198–216.

De Boer, G. J., J. D. Pietrzak, and J. C. Winterwerp (2008), Using the potential energy anomaly equation to investigate tidal straining and advection of stratification in a region of freshwater influence, *Ocean Modelling*, *22*(1), 1–11.

De Kok, J. (1996), A two-layer model of the rhine plume, *Journal of marine systems*, *8*(3), 269–284.

de Nijs, M. A., J. C. Winterwerp, and J. D. Pietrzak (2010), The effects of the internal flow structure on spm entrapment in the rotterdam waterway, *Journal of Physical Oceanography*, *40*(11), 2357–2380.

de Nijs, M. A., J. D. Pietrzak, and J. C. Winterwerp (2011), Advection of the salt wedge and evolution of the internal flow structure in the rotterdam waterway, *Journal of Physical Oceanography*, *41*(1), 3–27.

de Ruijter, W. P., A. W. Visser, and W. Bos (1997), The rhine outflow: a prototypical pulsed discharge plume in a high energy shallow sea, *Journal of marine Systems*, *12*(1), 263–276.

de Schipper, M. A., S. de Vries, G. Ruessink, R. C. de Zeeuw, J. Rutten, C. van Gelder-Maas, and M. J. Stive (2016), Initial spreading of a mega feeder nourishment: Observations of the sand engine pilot project, *Coastal Engineering*, *111*, 23–38.

Dickhudt, P. J., C. T. Friedrichs, and L. P. Sanford (2011), Mud matrix solids fraction and bed erodibility in the york river estuary, usa, and other muddy environments, *Continental Shelf Research*, *31*(10), S3–S13.

Drake, D. E., and D. A. Cacchione (1992), Wavecurrent interaction in the bottom boundary layer during storm and non-storm conditions: observations and model predictions, *Continental Shelf Research*, *12*(12), 1331–1352.

Drake, D. E., D. A. Cacchione, and W. D. Grant (1992), Shear stress and bed roughness estimates for combined wave and current flows over a rippled bed, *Journal of Geophysical Research: Oceans*, *97*(C2), 2319–2326.

Eisma, D. (1990), Transport and deposition of suspended matter in the north-sea and the relation to coastal siltation, pollution, and bottom fauna distribution, *Reviews in Aquatic Sciences*, *3*(2-3), 181–216.

Fettweis, M., and D. Van den Eynde (2003), The mud deposits and the high turbidity in the belgian–dutch coastal zone, southern bight of the north sea, *Continental Shelf Research*, *23*(7), 669–691.

Fewings, M., S. J. Lentz, and J. Fredericks (2008), Observations of cross-shelf flow driven by cross-shelf winds on the inner continental shelf, *Journal of Physical Oceanography*, *38*(11), 2358–2378.

Fewings, M. R., and S. J. Lentz (2010), Momentum balances on the inner continental shelf at martha's vineyard coastal observatory, *Journal of Geophysical Research: Oceans*, *115*(C12).

Fischer, E., H. Burchard, and R. D. Hetland (2009), Numerical investigations of the turbulent kinetic energy dissipation rate in the rhine region of freshwater influence, *Ocean Dynamics*, *59*(5), 629–641.

Fisher, N., J. Simpson, and M. Howarth (2002), Turbulent dissipation in the rhine rofi forced by tidal flow and wind stress, *Journal of sea research*, *48*(4), 249–258.

Flores, R. P., S. Rijnsburger, A. R. Horner-Devine, A. J. Souza, and J. D. Pietrzak (2017), The impact of storms and stratification on sediment transport in the rhine region of freshwater influence, *Journal of Geophysical Research: Oceans*, *122*(5), 4456–4477, doi:10.1002/2016JC012362.

Flores, R. P., S. Rijnsburger, S. Meirelles, A. R. Horner-Devine, A. J. Souza, J. D. Pietrzak, M. Henriquez, and A. Reniers (2018), Wave generation of gravity-driven sediment flows on a predominantly sandy seabed, *Geophysical Research Letters*.

Fong, D. A., and W. R. Geyer (2001), Response of a river plume during an upwelling favorable wind event, *Journal of Geophysical Research: Oceans*, *106*(C1), 1067–1084.

Fong, D. A., and W. R. Geyer (2002), The alongshore transport of freshwater in a surface-trapped river plume*, *Journal of Physical Oceanography*, *32*(3), 957–972.

Friedrichs, C., and L. Wright (2004), Gravity-driven sediment transport on the continental shelf: implications for equilibrium profiles near river mouths, *Coastal Engineering*, *51*(8), 795–811.

Friedrichs, C. T., and M. E. Scully (2007), Modeling deposition by wave-supported gravity flows on the po river prodelta: from seasonal floods to prograding clinoforms, *Continental Shelf Research*, *27*(3), 322–337.

Fugate, D. C., and C. T. Friedrichs (2002), Determining concentration and fall velocity of estuarine particle populations using adv, obs and lisst, *Continental Shelf Research*, *22*(11-13), 1867–1886.

Garvine, R. W. (1974), Physical features of the connecticut river outflow during high discharge, *Journal of Geophysical Research*, *79*(6), 831–846.

Garvine, R. W. (1977), Observations of the motion field of the connecticut river plume, *Journal of Geophysical Research*, *82*(3), 441–454.

Garvine, R. W. (1984), Radial spreading of buoyant, surface plumes in coastal waters, *Journal of Geophysical Research: Oceans*, *89*(C2), 1989–1996.

Geyer, W., P. Hill, and G. Kineke (2004), The transport, transformation and dispersal of sediment by buoyant coastal flows, *Continental Shelf Research*, *24*(7), 927–949.

Geyer, W. R. (1993), The importance of suppression of turbulence by stratification on the estuarine turbidity maximum, *Estuaries and Coasts*, *16*(1), 113–125.

Geyer, W. R., and P. MacCready (2014), The estuarine circulation, *Annual Review of Fluid Mechanics*, *46*.

Geyer, W. R., and R. Signell (1990), Measurements of tidal flow around a headland with a shipboard acoustic doppler current profiler, *Journal of Geophysical Research: Oceans*, *95*(C3), 3189–3197.

Geyer, W. R., J. H. Trowbridge, and M. M. Bowen (2000), The dynamics of a partially mixed estuary, *Journal of Physical Oceanography*, *30*(8), 2035–2048.

Geyer, W. R., J. D. Woodruff, and P. Traykovski (2001), Sediment transport and trapping in the hudson river estuary, *Estuaries*, *24*(5), 670–679.

Godin, G. (1972), The analysis of tides, 264 pp, *University of Toronto*.

Goring, D. G., and V. I. Nikora (2002), Despiking acoustic doppler velocimeter data, *Journal of Hydraulic Engineering*, *128*(1), 117–126.

Grabowski, R. C., I. G. DropPo, and G. Wharton (2011), Erodibility of cohesive sediment: the importance of sediment properties, *Earth-Science Reviews*, *105*(3-4), 101–120.

Grant, W. D., and O. S. Madsen (1979), Combined wave and current interaction with a rough bottom, *Journal of Geophysical Research: Oceans*, *84*(C4), 1797–1808.

Grant, W. D., and O. S. Madsen (1982), Movable bed roughness in unsteady oscillatory flow, *Journal of Geophysical Research: Oceans*, *87*(C1), 469–481.

Grant, W. D., and O. S. Madsen (1986), The continental-shelf bottom boundary layer, *Annual Review of Fluid Mechanics*, *18*(1), 265–305.

Gutierrez, B. T., G. Voulgaris, and E. R. Thieler (2005), Exploring the persistence of sorted bed-forms on the inner-shelf of wrightsville beach, north carolina, *Continental Shelf Research*, *25*(1), 65–90.

Gutierrez, B. T., G. Voulgaris, and P. A. Work (2006), Cross-shore variation of wind-driven flows on the inner shelf in long bay, south carolina, united states, *Journal of Geophysical Research: Oceans*, *111*(C3).

Hale, R. P., and A. S. Ogston (2015), In situ observations of wave-supported fluid-mud generation and deposition on an active continental margin, *Journal of Geophysical Research: Earth Surface*, *120*(11), 2357–2373.

Hansen, D. V., and M. Rattray (1965), Gravitational circulation in straits and estuaries, *J. mar. Res.*, *23*, 104–122.

Harris, C. K., P. Traykovski, and W. R. Geyer (2004), Including a near-bed turbid layer in a three dimensional sediment transport model with application to the eel river shelf, northern california, in *Estuarine and Coastal Modeling (2003)*, pp. 784–803.

Harris, C. K., P. A. Traykovski, and W. R. Geyer (2005), Flood dispersal and deposition by near-bed gravitational sediment flows and oceanographic transport: A numerical modeling study of the eel river shelf, northern california, *Journal of Geophysical Research: Oceans*, *110*(C9).

Harris, C. K., C. R. Sherwood, R. P. Signell, A. J. Bever, and J. C. Warner (2008), Sediment dispersal in the northwestern adriatic sea, *Journal of Geophysical Research: Oceans*, *113*(C11).

Hetland, R. D. (2005), Relating river plume structure to vertical mixing, *Journal of Physical Oceanography*, *35*(9), 1667–1688.

Hickey, B. M., R. M. Kudela, J. Nash, K. W. Bruland, W. T. Peterson, P. MacCready, E. J. Lessard, D. A. Jay, N. S. Banas, A. M. Baptista, et al. (2010), River influences on shelf ecosystems: introduction and synthesis, *Journal of Geophysical Research: Oceans*, *115*(C2).

Hooshmand, A., A. R. Horner-Devine, and M. P. Lamb (2015), Structure of turbulence and sediment stratification in wave-supported mud layers, *Journal of Geophysical Research: Oceans*, *120*(4), 2430–2448.

Horner-Devine, A. R., D. A. Jay, P. M. Orton, and E. Y. Spahn (2009), A conceptual model of the strongly tidal columbia river plume, *Journal of Marine Systems*, *78*(3), 460–475.

Horner-Devine, A. R., R. D. Hetland, and D. G. MacDonald (2015), Mixing and transport in coastal river plumes, *Annual Review of Fluid Mechanics*, *47*, 569–594.

Horner-Devine, A. R., J. D. Pietrzak, A. J. Souza, M. A. McKeon, S. Meirelles, M. Henriquez, R. P. Flores, and S. Rijnsburger (2017), Cross-shore transport of nearshore sediment by river plume frontal pumping, *Geophysical Research Letters*.

Horwitz, R., and S. J. Lentz (2014), Inner-shelf response to cross-shelf wind stress: The importance of the cross-shelf density gradient in an idealized numerical model and field observations, *Journal of Physical Oceanography*, *44*(1), 86–103.

Hsu, T.-J., C. E. Ozdemir, and P. A. Traykovski (2009), High-resolution numerical modeling of wave-supported gravity-driven mudflows, *Journal of Geophysical Research: Oceans*, *114*(C5).

Huisman, B., M. De Schipper, and B. Ruessink (2016), Sediment sorting at the sand motor at storm and annual time scales, *Marine Geology*, *381*, 209–226.

Hunt, J. (1954), The turbulent transport of suspended sediment in open channels, *Proc. R. Soc. Lond. A*, *224*(1158), 322–335.

Huthnance, J. (1991), Physical oceanography of the north sea, *Ocean and shoreline management*, *16*(3-4), 199–231.

Jacobs, W. (2004), Modelling the rhine river plume.

Janssen, G., and S. Mulder (2005), Zonation of macrofauna across sandy beaches and surf zones along the dutch coast, *Oceanologia*, *47*(2).

Jaramillo, S., A. Sheremet, M. Allison, A. Reed, and K. Holland (2009), Wave-mud interactions over the muddy atchafalaya subaqueous clinoform, louisiana, united states: Wave-supported sediment transport, *Journal of Geophysical Research: Oceans*, *114* (C4).

Jay, D. A., and J. D. Musiak (1994), Particle trapping in estuarine tidal flows, *Journal of Geophysical Research: Oceans*, *99* (C10), 20,445–20,461.

Jay, D. A., and J. D. Smith (1990), Circulation, density distribution and neap-spring transitions in the columbia river estuary, *Progress in Oceanography*, *25* (1-4), 81–112.

Jones, S., C. Jago, and J. Simpson (1996), Modelling suspended sediment dynamics in tidally stirred and periodically stratified waters: progress and pitfalls, *Coastal and Estuarine Studies*, pp. 302–324.

Joordens, J., A. Souza, and A. Visser (2001), The influence of tidal straining and wind on suspended matter and phytoplankton distribution in the rhine outflow region, *Continental Shelf Research*, *21* (3), 301–325.

Kim, S.-C., C. Friedrichs, J.-Y. Maa, and L. Wright (2000), Estimating bottom stress in tidal boundary layer from acoustic doppler velocimeter data, *Journal of Hydraulic Engineering*, *126* (6), 399–406.

Kumar, N., F. Feddersen, Y. Uchiyama, J. McWilliams, and W. OReilly (2015), Midshelf to surfzone coupled roms–swan model data comparison of waves, currents, and temperature: Diagnosis of subtidal forcings and response, *Journal of Physical Oceanography*, *45* (6), 1464–1490.

Lacy, J. R., C. R. Sherwood, D. J. Wilson, T. A. Chisholm, and G. R. Gelfenbaum (2005), Estimating hydrodynamic roughness in a wave-dominated environment with a high-resolution acoustic doppler profiler, *Journal of Geophysical Research: Oceans*, *110* (C6).

Lamb, M. P., and J. D. Parsons (2005), High-density suspensions formed under waves, *Journal of Sedimentary Research*, *75* (3), 386–397.

Lentz, S. J. (1995), Sensitivity of the inner-shelf circulation to the form of the eddy viscosity profile, *Journal of Physical Oceanography*, *25* (1), 19–28.

Lentz, S. J., and M. R. Fewings (2012), The wind-and wave-driven inner-shelf circulation, *Annual review of marine science*, *4*, 317–343.

Lentz, S. J., M. Fewings, P. Howd, J. Fredericks, and K. Hathaway (2008), Observations and a model of undertow over the inner continental shelf, *Journal of Physical Oceanography*, *38*(11), 2341–2357.

Lerczak, J. A., and R. Geyer (2004), Modeling the lateral circulation in straight, stratified estuaries, *Journal of Physical Oceanography*, *34*(6), 1410–1428.

Li, M. Z., and C. L. Amos (1998), Predicting ripple geometry and bed roughness under combined waves and currents in a continental shelf environment, *Continental Shelf Research*, *18*(9), 941–970.

Li, M. Z., L. Wright, and C. L. Amos (1996), Predicting ripple roughness and sand resuspension under combined flows in a shoreface environment, *Marine Geology*, *130*(1-2), 139–161.

Lynch, J., T. Gross, C. Sherwood, J. Irish, and B. Brumley (1997), Acoustical and optical backscatter measurements of sediment transport in the 1988–1989 stress experiment, *Continental Shelf Research*, *17*(4), 337–366.

Ma, Y., L. D. Wright, and C. T. Friedrichs (2008), Observations of sediment transport on the continental shelf off the mouth of the waiapu river, new zealand: evidence for current-supported gravity flows, *Continental Shelf Research*, *28*(4), 516–532.

Ma, Y., C. T. Friedrichs, C. K. Harris, and L. D. Wright (2010), Deposition by seasonal wave-and current-supported sediment gravity flows interacting with spatially varying bathymetry: Waiapu shelf, new zealand, *Marine Geology*, *275*(1), 199–211.

Macquaker, J. H., S. J. Bentley, and K. M. Bohacs (2010), Wave-enhanced sediment-gravity flows and mud dispersal across continental shelves: Reappraising sediment transport processes operating in ancient mudstone successions, *Geology*, *38*(10), 947–950.

Madsen, O. S. (1991), Mechanics of cohesionless sediment transport in coastal waters, in *Coastal sediments*, pp. 15–27, ASCE.

Madsen, O. S. (1995), Spectral wave-current bottom boundary layer flows, in *Coastal Engineering 1994*, pp. 384–398.

Malarkey, J., and A. G. Davies (2003), A non-iterative procedure for the wiberg and harris (1994) oscillatory sand ripple predictor, *Journal of Coastal Research*, *19*(3), 738–739.

Marchesiello, P., J. C. McWilliams, and A. Shchepetkin (2001), Open boundary conditions for long-term integration of regional oceanic models, *Ocean modelling*, *3*(1-2), 1–20.

Marsh, S., C. Vincent, and P. Osborne (1999), Bedforms in a laboratory wave flume: an evaluation of predictive models for bedform wavelengths, *Journal of Coastal Research*, pp. 624–634.

McCandliss, R., S. Jones, M. Hearn, R. Latter, and C. Jago (2002), Dynamics of suspended particles in coastal waters (southern north sea) during a spring bloom, *Journal of Sea Research*, *47*(3), 285–302.

Meirelles, S., M. Henriquez, A. J. Souza, A. R. Horner-Devine, J. D. Pietrzak, S. Rijnsburg, and M. J. Stive (2016), Small scale bedform types off the south-holland coast, *Journal of Coastal Research*, *75*(sp1), 423–426.

Milliman, J. D., and R. H. Meade (1983), World-wide delivery of river sediment to the oceans, *The Journal of Geology*, *91*(1), 1–21.

Milliman, J. D., and J. P. Syvitski (1992), Geomorphic/tectonic control of sediment discharge to the ocean: the importance of small mountainous rivers, *The Journal of Geology*, *100*(5), 525–544.

Monismith, S., J. Burau, and M. Stacey (1996), Stratification dynamics and gravitational circulation in northern san francisco bay, *San Francisco Bay: The Ecosystem*, pp. 123–153.

Münchow, A., and R. W. Garvine (1993), Dynamical properties of a buoyancy-driven coastal current, *Journal of Geophysical Research: Oceans*, *98*(C11), 20,063–20,077.

Nelson, T. R., and G. Voulgaris (2014), Temporal and spatial evolution of wave-induced ripple geometry: Regular versus irregular ripples, *Journal of Geophysical Research: Oceans*, *119*(2), 664–688.

Nelson, T. R., and G. Voulgaris (2015), A spectral model for estimating temporal and spatial evolution of rippled seabeds, *Ocean Dynamics*, *65*(2), 155–171.

Nelson, T. R., G. Voulgaris, and P. Traykovski (2013), Predicting wave-induced ripple equilibrium geometry, *Journal of Geophysical Research: Oceans*, *118*(6), 3202–3220.

Nielsen, P. (1981), Dynamics and geometry of wave-generated ripples, *Journal of Geophysical Research: Oceans*, *86*(C7), 6467–6472.

Nielsen, P. (1992), *Coastal bottom boundary layers and sediment transPort*, vol. 4, World Scientific Publishing Company.

Nittrouer, C. A., and L. D. Wright (1994), Transport of particles across continental shelves, *Reviews of Geophysics*, *32*(1), 85–113.

O'Donoghue, T., and G. S. Clubb (2001), Sand ripples generated by regular oscillatory flow, *Coastal Engineering*, *44*(2), 101–115.

Ogston, A., D. Cacchione, R. Sternberg, and G. Kineke (2000), Observations of storm and river flood-driven sediment transport on the northern california continental shelf, *Continental Shelf Research*, *20*(16), 2141–2162.

Palmer, M. R. (2010), The modification of current ellipses by stratification in the liverpool bay rofi, *Ocean Dynamics*, *60*(2), 219–226.

Parsons, J. D., C. T. Friedrichs, P. A. Traykovski, D. Mohrig, J. Imran, J. P. Syvitski, G. Parker, P. Puig, J. L. Buttles, and M. H. Garcia (2007), The mechanics of marine sediment gravity flows, *Continental Margin Sedimentation: From Sediment TransPort to Sequence Stratigraphy, C. Nittrouer, J. Austin, M. Field, J. Syvitski, and P. Wiberg, eds., Blackwell, Oxford, UK*, pp. 275–333.

Partheniades, E. (1965), Erosion and deposition of cohesive soils, *Journal of the Hydraulics Division*, *91*(1), 105–139.

Pawlowicz, R., B. Beardsley, and S. Lentz (2002), Classical tidal harmonic analysis including error estimates in matlab using t_tide, *Computers & Geosciences*, *28*(8), 929–937.

Pedocchi, F., and M. Garcia (2009), Ripple morphology under oscillatory flow: 1. prediction, *Journal of Geophysical Research: Oceans*, *114*(C12).

Peperzak, L., F. Colijn, R. Koeman, W. Gieskes, and J. Joordens (2003), Phytoplankton sinking rates in the rhine region of freshwater influence, *Journal of Plankton Research*, *25*(4), 365–383.

Perron, J. T., J. W. Kirchner, and W. E. Dietrich (2008), Spectral signatures of characteristic spatial scales and nonfractal structure in landscapes, *Journal of Geophysical Research: Earth Surface*, *113*(F4).

Pietrzak, J., J. B. Jakobson, H. Burchard, H. J. Vested, and O. Petersen (2002), A three-dimensional hydrostatic model for coastal and ocean modelling using a generalised topography following co-ordinate system, *Ocean Modelling*, *4*(2), 173–205.

Pietrzak, J. D., G. J. de Boer, and M. A. Eleveld (2011), Mechanisms controlling the intra-annual mesoscale variability of sst and spm in the southern north sea, *Continental Shelf Research*, *31*(6), 594–610.

Prandle, D. (1982), The vertical structure of tidal currents and other oscillatory flows, *Continental Shelf Research*, *1*(2), 191–207.

Puig, P., A. Ogston, B. Mullenbach, C. Nittrouer, and R. Sternberg (2003), Shelf-to-canyon sediment-transport processes on the eel continental margin (northern california), *Marine Geology*, *193*(1), 129–149.

Puig, P., A. Ogston, B. Mullenbach, C. Nittrouer, J. Parsons, and R. Sternberg (2004), Storm-induced sediment gravity flows at the head of the eel submarine canyon, northern california margin, *Journal of Geophysical Research: Oceans*, *109*(C3).

Radermacher, M., M. A. de Schipper, C. Swinkels, J. H. MacMahan, and A. J. Reniers (2016), Tidal flow separation at protruding beach nourishments, *Journal of Geophysical Research: Oceans*.

Rijnsburger, S., C. M. van der Hout, O. van Tongeren, G. J. de Boer, B. C. van Prooijen, W. G. Borst, and J. D. Pietrzak (2016), Simultaneous measurements of tidal straining and advection at two parallel transects far downstream in the rhine rofi, *Ocean Dynamics*, *66*(5), 719–736.

Rijnsburger, S., R. P. Flores, J. D. Pietrzak, A. R. Horner-Devine, and A. J. Souza (2018), The influence of tide and wind on the propagation of fronts in a shallow river plume, *Journal of Geophysical Research: Oceans.*

Rippeth, T. P., N. R. Fisher, and J. H. Simpson (2001), The cycle of turbulent dissipation in the presence of tidal straining, *Journal of Physical Oceanography*, *31*(8), 2458–2471.

Rippeth, T. P., E. Williams, and J. H. Simpson (2002), Reynolds stress and turbulent energy production in a tidal channel, *Journal of Physical Oceanography*, *32*(4), 1242–1251.

Roos, P. C., J. J. Velema, S. J. Hulscher, and A. Stolk (2011), An idealized model of tidal dynamics in the north sea: resonance properties and response to large-scale changes, *Ocean dynamics*, *61*(12), 2019–2035.

Rouse, H. (1937), Modern conceptions of the mechanics of fluid turbulence, *Trans ASCE*, *102*, 463–505.

Ruddick, K., E. Deleersnijder, P. Luyten, and J. Ozer (1995), Haline stratification in the rhine-meuse freshwater plume: a three-dimensional model sensitivity analysis, *Continental Shelf Research*, (13).

Sanford, L. P., and J. P.-Y. Maa (2001), A unified erosion formulation for fine sediments, *Marine Geology*, *179*(1-2), 9–23.

Scheu, K., D. Fong, S. Monismith, and O. Fringer (2015), Sediment transport dynamics near a river inflow in a large alpine lake, *Limnology and Oceanography*, *60*(4), 1195–1211.

Schulz, K., and L. Umlauf (2016), Residual transport of suspended material by tidal straining near sloping topography, *Journal of Physical Oceanography*, *46*(7), 2083–2102.

Scully, M., C. Friedrichs, and L. Wright (2002), Application of an analytical model of critically stratified gravity-driven sediment transport and deposition to observations from the eel river continental shelf, northern california, *Continental Shelf Research*, *22*(14), 1951–1974.

Scully, M., C. Friedrichs, and L. Wright (2003), Numerical modeling of gravity-driven sediment transport and deposition on an energetic continental shelf: Eel river, northern california, *Journal of Geophysical Research: Oceans*, *108*(C4).

Scully, M. E., and C. T. Friedrichs (2007), Sediment pumping by tidal asymmetry in a partially mixed estuary, *Journal of Geophysical Research: Oceans*, *112*(C7).

Scully, M. E., J. H. Trowbridge, C. R. Sherwood, K. R. Jones, and P. Traykovski (2018), Direct measurements of mean reynolds stress and ripple roughness in the presence of energetic forcing by surface waves, *Journal of Geophysical Research: Oceans*, *123*(4), 2494–2512.

Shaw, W. J., and J. H. Trowbridge (2001), The direct estimation of near-bottom turbulent fluxes in the presence of energetic wave motions, *Journal of Atmospheric and Oceanic Technology*, *18*(9), 1540–1557.

Shchepetkin, A. F., and J. C. McWilliams (2005), The regional oceanic modeling system (roms): a split-explicit, free-surface, topography-following-coordinate oceanic model, *Ocean modelling*, *9*(4), 347–404.

Simpson, J. (1997), Physical processes in the rofi regime, *Journal of marine systems*, *12*(1), 3–15.

Simpson, J., and A. Souza (1995), Semidiurnal switching of stratification in the region of freshwater influence of the rhine, *Journal of Geophysical Research: Oceans*, *100*(C4), 7037–7044.

Simpson, J., E. Williams, L. Brasseur, and J. Brubaker (2005), The impact of tidal straining on the cycle of turbulence in a partially stratified estuary, *Continental Shelf Research*, *25*(1), 51–64.

Simpson, J. H., J. Brown, J. Matthews, and G. Allen (1990), Tidal straining, density currents, and stirring in the control of estuarine stratification, *Estuaries*, *13*(2), 125–132.

Simpson, J. H., W. G. Bos, F. Schirmer, A. J. Souza, T. P. Rippeth, S. E. Jones, and D. Hydes (1993), Periodic stratification in the rhine rofi in the north sea, *Oceanologica Acta*, *16*(1), 23–32.

Soulsby, R. (1997), *Dynamics of marine sands: a manual for practical applications*, Thomas Telford.

Soulsby, R., L. Hamm, G. Klopman, D. Myrhaug, R. Simons, and G. Thomas (1993), Wave-current interaction within and outside the bottom boundary layer, *Coastal engineering*, *21*(1-3), 41–69.

Soulsby, R., R. Whitehouse, et al. (1997), Threshold of sediment motion in coastal environments, in *Pacific Coasts and Ports' 97: Proceedings of the 13th Australasian Coastal and Ocean Engineering Conference and the 6th Australasian Port and Harbour Conference; Volume 1*, p. 145, Centre for Advanced Engineering, University of Canterbury.

Soulsby, R., R. Whitehouse, and K. Marten (2012), Prediction of time-evolving sand ripples in shelf seas, *Continental Shelf Research*, *38*, 47–62.

Soulsby, R. L. (1983), The bottom boundary layer of shelf seas, in *Elsevier oceanography series*, vol. 35, pp. 189–266, Elsevier.

Souza, A. (2013), On the use of the stokes number to explain frictional tidal dynamics and water column structure in shelf seas, *Ocean Science*, *9*, 391–398.

Souza, A., and I. James (1996), A two-dimensional (xz) model of tidal straining in the rhine rofi, *Continental Shelf Research*, *16*(7), 946–966.

Souza, A., and J. Simpson (1996), The modification of tidal ellipses by stratification in the rhine rofi, *Continental Shelf Research*, *16*(8), 997–1007.

Souza, A., J. Simpson, and F. Schirmer (1997), Current structure in the rhine region of freshwater influence, *Journal of marine research*, *55*(2), 277–292.

Souza, A. J., and A. Lane (2013), Effects of freshwater inflow on sediment transport, *Journal of Operational Oceanography*, *6*(1), 27–31.

Souza, A. J., and J. H. Simpson (1997), Controls on stratification in the rhine rofi system, *Journal of Marine Systems*, *12*(1), 311–323.

Souza, A. J., L. G. Alvarez, and T. D. Dickey (2004), Tidally induced turbulence and suspended sediment, *Geophysical Research Letters*, *31*(20).

Souza, A. J., J. T. Holt, and R. Proctor (2007), Modelling spm on the nw european shelf seas, *Geological Society, London, Special Publications*, *274*(1), 147–158.

Souza, A. J., N. R. Fisher, J. H. Simpson, and M. J. Howarth (2008), Effects of tidal straining on the semidiurnal cycle of dissipation in the rhine region of freshwater influence: Comparison of model and measurements, *Journal of Geophysical Research: Oceans*, *113*(C1).

Stacey, M. T., S. G. Monismith, and J. R. Burau (1999), Observations of turbulence in a partially stratified estuary, *Journal of Physical Oceanography*, *29*(8), 1950–1970.

Stacey, M. T., J. R. Burau, and S. G. Monismith (2001), Creation of residual flows in a partially stratified estuary, *J. Geophys. Res*, *106*(17), 013–17.

Stacey, M. T., M. L. Brennan, J. R. Burau, and S. G. Monismith (2010), The tidally averaged momentum balance in a partially and periodically stratified estuary, *Journal of Physical Oceanography*, *40*(11), 2418–2434.

Stive, M. J., M. A. de Schipper, A. P. Luijendijk, S. G. Aarninkhof, C. van Gelder-Maas, J. S. van Thiel de Vries, S. de Vries, M. Henriquez, S. Marx, and R. Ranasinghe (2013), A new alternative to saving our beaches from sea-level rise: The sand engine, *Journal of Coastal Research*, *29*(5), 1001–1008.

Styles, R., and S. M. Glenn (2000), Modeling stratified wave and current bottom boundary layers on the continental shelf, *Journal of Geophysical Research: Oceans*, *105*(C10), 24,119–24,139.

Styles, R., and S. M. Glenn (2002), Modeling bottom roughness in the presence of wave-generated ripples, *Journal of Geophysical Research: Oceans*, *107*(C8).

Swart, D. H. (1974), Offshore sediment transport and equilibrium beach profiles, Ph.D. thesis, TU Delft, Delft University of Technology.

Thorne, P. D., and D. M. Hanes (2002), A review of acoustic measurement of small-scale sediment processes, *Continental shelf research*, *22*(4), 603–632.

Thorne, P. D., D. Hurther, and B. D. Moate (2011), Acoustic inversions for measuring boundary layer suspended sediment processes, *The Journal of the Acoustical Society of America*, *130*(3), 1188–1200.

Traykovski, P. (2007), Observations of wave orbital scale ripples and a nonequilibrium time-dependent model, *Journal of Geophysical Research: Oceans*, *112*(C6).

Traykovski, P., A. E. Hay, J. D. Irish, and J. F. Lynch (1999), Geometry, migration, and evolution of wave orbital ripples at leo-15, *Journal of Geophysical Research: Oceans*, *104*(C1), 1505–1524.

Traykovski, P., W. R. Geyer, J. Irish, and J. Lynch (2000), The role of wave-induced density-driven fluid mud flows for cross-shelf transport on the eel river continental shelf, *Continental Shelf Research*, *20*(16), 2113–2140.

Traykovski, P., P. L. Wiberg, and W. R. Geyer (2007), Observations and modeling of wave-supported sediment gravity flows on the po prodelta and comparison to prior observations from the eel shelf, *Continental Shelf Research*, *27*(3), 375–399.

Trowbridge, J., and G. Kineke (1994), Structure and dynamics of fluid muds on the amazon continental shelf, *Journal of Geophysical Research: Oceans*, *99*(C1), 865–874.

Umlauf, L., and H. Burchard (2003), A generic length-scale equation for geophysical turbulence models, *Journal of Marine Research*, *61*(2), 235–265.

Van Alphen, J. (1990), A mud balance for belgian-dutch coastal waters between 1969 and 1986, *Netherlands Journal of Sea Research*, *25*(1-2), 19–30.

Van Alphen, J., W. De Ruijter, and J. Borst (1988), Outflow and three-dimensional spreading of rhine river water in the netherlands coastal zone, in *Physical processes in estuaries*, pp. 70–92, Springer.

van der Hout, C., R. Witbaard, M. Bergman, G. Duineveld, M. Rozemeijer, and T. Gerkema (2017), The dynamics of suspended particulate matter (spm) and chlorophyll-a from intratidal to annual time scales in a coastal turbidity maximum, *Journal of Sea Research*.

van der Hout, C. M., T. Gerkema, J. J. Nauw, and H. Ridderinkhof (2015), Observations of a narrow zone of high suspended particulate matter (spm) concentrations along the dutch coast, *Continental Shelf Research*, *95*, 27–38.

Van Kessel, T., H. Winterwerp, B. Van Prooijen, M. Van Ledden, and W. Borst (2011), Modelling the seasonal dynamics of spm with a simple algorithm for the buffering of fines in a sandy seabed, *Continental Shelf Research*, *31*(10), S124–S134.

Van Prooijen, B., and J. Winterwerp (2010), A stochastic formulation for erosion of cohesive sediments, *Journal of Geophysical Research: Oceans*, *115*(C1).

Van Rijn, L. C., et al. (1993), *Principles of sediment transPort in Rivers, estuaries and coastal seas*, vol. 1006, Aqua publications Amsterdam.

Verspecht, F., T. P. Rippeth, J. H. Simpson, A. J. Souza, H. Burchard, and M. J. Howarth (2009a), Residual circulation and stratification in the liverpool bay region of freshwater influence, *Ocean Dynamics*, *59*(5), 765–779.

Verspecht, F., T. Rippeth, M. Howarth, A. Souza, J. Simpson, and H. Burchard (2009b), Processes impacting on stratification in a region of freshwater influence: Application to liverpool bay, *Journal of Geophysical Research: Oceans*, *114*(C11).

Verspecht, F., J. Simpson, and T. Rippeth (2010), Semi-diurnal tidal ellipse variability in a region of freshwater influence, *Geophysical Research Letters*, *37*(18).

Visser, A., A. Souza, K. Hessner, and J. Simpson (1994), The effect of stratification on tidal current profiles in a region of fresh-water influence, *Oceanologica acta*, *17*(4), 369–381.

Visser, M., W. De Ruijter, and L. Postma (1991), The distribution of suspended matter in the dutch coastal zone, *Netherlands Journal of Sea Research*, *27*(2), 127–143.

Voulgaris, G., and S. T. Meyers (2004), Temporal variability of hydrodynamics, sediment concentration and sediment settling velocity in a tidal creek, *Continental Shelf Research*, *24*(15), 1659–1683.

Walsh, J., C. Nittrouer, C. Palinkas, A. Ogston, R. Sternberg, and G. Brunskill (2004), Clinoform mechanics in the gulf of papua, new guinea, *Continental Shelf Research*, *24*(19), 2487–2510.

Warner, J. C., C. R. Sherwood, H. G. Arango, and R. P. Signell (2005), Performance of four turbulence closure models implemented using a generic length scale method, *Ocean Modelling*, *8*(1-2), 81–113.

Warner, J. C., C. R. Sherwood, R. P. Signell, C. K. Harris, and H. G. Arango (2008a), Development of a three-dimensional, regional, coupled wave, current, and sediment-transport model, *Computers & Geosciences*, *34*(10), 1284–1306.

Warner, J. C., B. Butman, and P. S. Dalyander (2008b), Storm-driven sediment transport in massachusetts bay, *Continental Shelf Research*, *28*(2), 257–282.

Wiberg, P. L., and C. K. Harris (1994), Ripple geometry in wave-dominated environments, *Journal of Geophysical Research: Oceans*, *99*(C1), 775–789.

Wiberg, P. L., and C. R. Sherwood (2008), Calculating wave-generated bottom orbital velocities from surface-wave parameters, *Computers & Geosciences*, *34*(10), 1243–1262.

Wiberg, P. L., D. E. Drake, and D. A. Cacchione (1994), Sediment resuspension and bed armoring during high bottom stress events on the northern california inner continental shelf: measurements and predictions, *Continental Shelf Research*, *14*(10-11), 1191–1219.

Winant, C. D. (2007), Three-dimensional tidal flow in an elongated, rotating basin, *Journal of Physical Oceanography*, *37*(9), 2345–2362.

Winterwerp, J. (2002), On the flocculation and settling velocity of estuarine mud, *Continental shelf research*, *22*(9), 1339–1360.

Winterwerp, J. C., Z. B. Wang, A. van Braeckel, G. van Holland, and F. Kösters (2013), Man-induced regime shifts in small estuariesii: a comparison of rivers, *Ocean Dynamics*, *63*(11-12), 1293–1306.

Wright, L., and C. Friedrichs (2006), Gravity-driven sediment transport on continental shelves: a status report, *Continental Shelf Research*, *26*(17), 2092–2107.

Wright, L., W. Wiseman, B. Bornhold, D. Prior, J. Suhayda, G. Keller, Z.-S. Yang, and Y. Fan (1988), Marine dispersal and deposition of yellow river silts by gravity-driven underflows, *Nature*, *332*(6165), 629–632.

Wright, L., C. Friedrichs, S. Kim, and M. Scully (2001), Effects of ambient currents and waves on gravity-driven sediment transport on continental shelves, *Marine Geology*, *175*(1), 25–45.

Wu, H., J. Shen, J. Zhu, J. Zhang, and L. Li (2014), Characteristics of the changjiang plume and its extension along the jiangsu coast, *Continental Shelf Research*, *76*, 108–123.

Yankovsky, A. E., and D. C. Chapman (1997), A simple theory for the fate of buoyant coastal discharges, *Journal of Physical oceanography*, *27*(7), 1386–1401.

Yoshiyama, K., and J. H. Sharp (2006), Phytoplankton response to nutrient enrichment in an urbanized estuary: Apparent inhibition of primary production by overeutrophication, *Limnology and Oceanography*, *51*(1part2), 424–434.